Fermi National Accelerator Laboratory

FERMILAB-Pub-79/30-EXP
7340.098
7340.398

(Submitted to Phys. Rev. D)

A MEASUREMENT OF THE NUCLEON STRUCTURE FUNCTIONS

H. L. Anderson, R. M. Fine, R. H. Heisterberg, W. W. Kinnison,
H. S. Matis, L. W. Mo, L. C. Myrianthopoulos, and S. C. Wright
Enrico Fermi Institute and Department of Physics, University of Chicago
Chicago, Illinois 60637 USA

and

B. A. Gordon, W. A. Loomis, F. M. Pipkin, S. H. Pordes,
A. L. Sessoms, W. D. Shambroom, C. Tao, L. J. Verhey,
and Richard Wilson
High Energy Physics Laboratory and Department of Physics
Harvard University, Cambridge, Massachusetts 02138 USA

and

W. R. Francis, R. G. Hicks, and T. B. W. Kirk
Department of Physics, University of Illinois, Urbana, Illinois 61801

and

V. K. Bharadwaj, N. W. Booth, G. I. Kirkbride, J. Proudfoot,
T. W. Quirk, A. Skuja, M. A. Staton, and W. S. C. Williams
Nuclear Physics Laboratory, University of Oxford
Keble Road, Oxford, OX1 3RH, England

May 1979

Operated by Universities Research Association Inc. under contract with the Energy Research and Development Administration

A MEASUREMENT OF THE NUCLEON STRUCTURE FUNCTIONS

H.L. Anderson, R.M. Fine,[1] R.H. Heisterberg,[2] W.W. Kinnison, H.S. Matis,[3] L.W. Mo,[2] L.C. Myrianthopoulos, S.C. Wright

Enrico Fermi Institute and Department of Physics
University of Chicago
Chicago, Illinois 60637

B.A. Gordon, W.A. Loomis, F.M. Pipkin, S.H. Pordes,[4] A.L. Sessoms, W.D. Shambroom,[5] C. Tao, L.J. Verhey,[6] Richard Wilson

High Energy Physics Laboratory
and
Department of Physics
Harvard University
Cambridge, Massachusetts 02138

W.R. Francis,[7] R.G. Hicks,[8] T.B.W. Kirk[8]

Department of Physics
University of Illinois
Urbana, Illinois 61801

V.K. Bharadwaj,[9] N.E. Booth, G.I. Kirkbride,[10] J. Proudfoot,[11] T.W. Quirk,[12] A. Skuja,[13] M.A. Staton, W.S.C. Williams

Nuclear Physics Laboratory
University of Oxford
Keble Road, Oxford, OX1 3RH, England

(1) Present address: Nevis Laboratory, Columbia University, New York, NY 10027
(2) Present address: Department of Physics, Virginia Polytechnic Institute and State University, Blacksburg, Virginia 20461
(3) Present address: Los Alamos Scientific Laboratory, Los Alamos, New Mexico 87545
(4) Present address: CERN, CH-1211, Geneva 23, Switzerland
(5) Present address: Dept. of Physics, Northeastern University, Boston, MA 02115
(6) Present address: Massachusetts General Hospital, Boston, MA 02115
(7) Present address: Michigan State University, Lansing, MI 48823
(8) Present address: Fermi National Accelerator Laboratory, Batavia, IL 60510
(9) Present address: Dept. of Physics, University of California, Santa Barbara, CA 93106
(10) Present address: Hansen Laboratory, Stanford University, Stanford, CA 94305
(11) Present address: Rutherford High Energy Laboratory, Chilton, Didcot, Berks. OX11 0QX, England
(12) Present address: Bougainville Copper, Panguna, Bougainville, Papua New Guinea
(13) Present address: Dept. of Physics and Astronomy, University of Maryland, College Park, MD 20742

ABSTRACT

Measurements have been made of the inclusive scattering of 96, 147, and 219 GeV muons from hydrogen, and of 147 GeV muons from deuterium. Results are presented for the nucleon structure function $F_2(x, Q^2)$ ($\equiv \nu W_2(x, Q^2)$) $10 < \nu < 200$ GeV and $0.2 < Q^2 < 80$ GeV^2. The value of F_2 rises with Q^2 at small x, and falls with Q^2 at large x in agreement with the ideas of QCD. An average value of the ratio $\sigma_L/\sigma_T \equiv R = 0.52 \pm 0.35$ has been obtained for the region $0.003 < x < 0.10$ and $0.4 < Q^2 < 30$ GeV^2. The values of F_2 from this experiment have been combined with those from other charged lepton scattering experiments to derive moments of the structure functions. The variation with Q^2 of these moments is used to derive values for Λ taking into account corrections up to 2nd order in α_s. The fit to the data is very good.

I. Introduction

The inelastic scattering of leptons by nucleons is an important probe of the structure of hadronic matter. In particular the scattering of the charged leptons, muons or electrons, probes the electric and magnetic structure of the hadrons. This technique has some important properties. The first is that the electron or muon can be treated as a structureless point charge which interacts in a known way only with the electric charge and current distribution in the target nucleon. No experiment to date has detected any behavior of these leptons which is not adequately described by treating them as point Dirac particles.[1,2] Compared to hadron-hadron interactions, which may have to be described by considering the convolution of two complex structures, charged lepton scattering can be interpreted unambiguously in terms of the electromagnetic structure of the hadronic target. In addition, since the electromagnetic coupling constant is small, only the lowest order processes need to be considered when relating measured cross-sections to the hadronic structure. A second attractive feature of charged lepton scattering is that the momentum of both initial and final lepton can be measured. Consequently, ν, the laboratory energy transfer, and Q^2, where $-Q^2$ is the square of the mass of the virtual photon exchanged, can be varied independently subject only to the condition $Q^2 \leq 2M\nu$. (See Figure 1 and Table I for definitions of kinematic variables.) Unlike the situation in photoproduction processes, which are constrained to have $Q^2 = 0$, muon and electron scattering allow an investigation over a range of values of Q^2 limited only by the incident energy and by the apparatus acceptance and luminosity.

This paper is concerned with muon scattering by nucleons. Muon scattering

has an advantage over electron scattering in that the radiative corrections that must be applied are considerably less, and the associated uncertainties are therefore smaller.

The first series of deep inelastic scattering experiments was performed at the Stanford Linear Accelerator Center using electrons, starting in 1967, and showed that the inelastic cross sections were large and decreased approximately as $1/Q^4$. [3] This is the behavior expected for scattering from a point charge. This is in contrast to the cross-section for elastic scattering ($Q^2 = 2M\nu$) which decreased as $1/Q^{12}$ (made up from $1/Q^4$ for the photon propagator and $1/Q^8$ from the square of the form factor).

This result meant that the nucleon structure functions, which play the same role in inelastic scattering as do the squares of the form factors in elastic scattering, were varying much more slowly with increasing Q^2 than were the elastic form factors. These structure functions W_2 and W_1 are related to the inelastic differential cross section for charged lepton scattering through the formula

$$\frac{d^2\sigma}{dQ^2 d\nu} = \frac{2\pi\alpha^2}{p^2 Q^4} \left[(2\,EE' - Q^2/2)W_2 + (Q^2 - 2m_\mu^2)\,W_1\right] \qquad (1)$$

The early results obtained from electron deep inelastic scattering showed that, to a precision of about 20%, the structure functions F_2 ($\equiv \nu W_2$) and F_1 ($\equiv 2MW_1$) were not functions of Q^2 and ν separately, but only of their ratio $2M\nu/Q^2$ ($\equiv \omega \equiv 1/x$). This so-called scaling behavior set in when $Q^2 > 2$ GeV^2. Thus, at fixed ω, the scattering cross section falls approximately as $1/Q^4$ as Q^2 increases. This property of scaling had been anticipated by Bjorken, [4, 5] who suggested that this should be the asymptotic behavior for large Q^2;

$Q^2 >>$ all masses. It was a surprise that it held for such low values of Q^2 (~ 2 GeV^2). Later results extended the earlier measurements out to $Q^2 = 6$ GeV^2 and $\nu = 15$ GeV and found that in certain regions scaling in the variable ω was violated but that it was restored by changing to a variable $\omega' = \omega + M^2/Q^2$. Readers are referred to review articles and references contained therein.[6]

The $1/Q^4$ dependence of the cross section suggested that the muon was scattering from point-like objects within the proton. Feynman[7] called these point-like objects "partons" and derived a simple parton model of the nucleon; he used the impulse approximation in the infinite momentum frame and thereby justified the appearance of the parton's point-like nature in the proton structure functions. The identification of the charged partons with quarks (the quark-parton model) led to several predictions in agreement with experiment.

The simple quark-parton model, while attractive, cannot be put on a field-theoretic basis. Subsequent theoretical ideas used the operator production expansion[8,9] and the renormalization group to connect the scaling prediction with the leading terms in renormalizable field theories. In the non-Abelian class of gauge field theories, the effective coupling constant vanishes at large momentum transfer and the quarks become asymptotically free[10,11] and thereby justify the use of the impulse approximation.[7] A color quantum number has been added to the quarks and the theory has developed into "Quantum Chromodynamics" or QCD.[12] By analogy with quantum electrodynamics (QED), QCD can be viewed as the quark parton model with the inclusion of gluon exchange and gluon radiation, just as QED is the simple Dirac model with the addition of photon exchange and photon radiation. QCD can predict, from first principles, the pattern of scale breaking observed in deep inelastic electron and muon scattering.[13] The form of scale breaking observed can then be used as input

to more phenomenological quark-gluon models, or in fits to other data, to provide accounts of several processes, including the Drell-Yan process in direct muon pair production in proton-proton collisions,[14,15] high p_T hadron-hadron scattering,[16] and neutrino and anti-neutrino inelastic scattering.[17,18]

The construction of the Fermilab accelerator made available useful muon beams of energies up to 275 GeV; this allowed measurements of the structure functions at values of Q^2 and ν greater than those previously accessible. Preliminary results have been published for scattering from an iron target,[19,20] and from hydrogen and deuterium.[21,22,23] This paper reports in detail the results of the latter experiments done at muon beam energies of 96, 147 and 219 GeV. Table II shows the statistics of incident muons and the number of events at each energy. In discussing the data, the assumption is made that muon-electron universality[1,2] holds, and that the only process involved is single photon exchange (Fig. 1).

II. Kinematic Quantities

There is a standard equivalent expression for the cross-section which emphasizes the connection between real photoproduction ($Q^2 = 0$) and muon (or electron) scattering as virtual photoproduction ($Q^2 > 0$). Defining σ_T and σ_L as the total cross-sections for transverse and longitudinal virtual photons, then (Table I)

$$\frac{d^2\sigma}{dQ^2 d\nu} = \Gamma\,(\sigma_T + \varepsilon\sigma_L) \tag{2}$$

It is convenient to define

$$\sigma = \sigma_T + \varepsilon\sigma_L\ . \tag{3}$$

The ratio $R \equiv \sigma_L/\sigma_T$ is of special interest. In a parton model where all the partons have zero momentum transverse to the proton's direction, R reflects the parton spin (for spin 0, $R = \infty$; for spin 1/2, $R = 0$); in a less constrained model, the value of R reflects the average transverse momentum of the partons.

$$R = 4\,\langle p_T^2\rangle/Q^2$$

In QCD, $\langle p_T^2\rangle$ contains two parts added in quadrature: the first arises from the transverse recoil of the quark arising from gluon bremsstrahlung and may be estimated from pertubative QCD calculations.[24] It is approximately $(1 - x)Q^2/[8\ \ln(Q^2/1\ \text{GeV}^2)]$. The second part arises from confinement of the quark (and the uncertainty principle) for which there is presently no generally accepted calculation. For this second part experiment suggests $\langle p_T^2\rangle \sim 0.3\ \text{GeV}^2$. The value of R is obtained by measuring the differential cross section at the same Q^2 and ν but at different incident beam energies thus changing the virtual photon polarization ε. (The procedure is identical to that used in separating G_E and G_M in elastic scatttering.) This measurement is difficult since the cross sections depend only weakly on the value of R. The cross section can now be rewritten in terms of R:

$$\frac{d^2\sigma}{dQ^2 d\nu} = \frac{2\pi\alpha^2}{Q^4}\,\frac{1}{p^2}\,\frac{F_2(Q^2,\nu)}{\nu}\left[(2EE' - Q^2/2) + \frac{(Q^2 - 2m_\mu^2)(1 + \nu^2/Q^2)}{1 + R(Q^2,\nu)}\right] \quad (4)$$

where the connection between the structure functions and σ_L and σ_T is given by

$$F_2 \equiv \nu W_2 = \frac{\nu K}{4\pi^2\alpha}\,\frac{Q^2}{Q^2 + \nu^2}\,(\sigma_T + \sigma_L) \quad (5)$$

$$F_1 \equiv 2MW_1 = \frac{2MK}{4\pi^2\alpha}\,\sigma_T \quad (6)$$

$$R = \left(1 + \frac{\nu^2}{Q^2}\right)\left(\frac{F_2}{F_1}\right)\left(\frac{2M}{\nu}\right) - 1 \quad (7)$$

III. Apparatus

The apparatus can be divided for the purpose of description into ten separate sections. They are:

1. the muon beam and tagging system
2. the target
3. the upstream multiwire proportional chambers
4. the spectrometer magnet
5. the downstream spark chambers
6. the trigger and timing scintillation counter hodoscopes, G and H
7. the photon and neutral hadron detectors
8. the hadron absorber
9. the muon counter hodoscopes, M, M', N, and K
10. the muon spark chambers

These are described in the above order. A right handed coordinate system is used with the z axis lying along the nominal beam direction, the y axis pointing vertically and the x axis pointing to the left of the beam. The origin is at the center of the spectrometer magnet. The dimensions of items are given in the order x, y, z.

III.1 The muon beam and tagging system

A muon beam was produced by the decay in flight of pions and kaons produced in high energy proton-nucleon collisions. Fig. 2 shows a schematic layout of the Fermilab muon beam. This beam was designed as an adjunct of a neutrino beam in order to allow both neutrino and muon experiments to share the same parent pions and to take data simultaneously. The result was a design which had a limited momentum acceptance of ±2.5%, a limited acceptance

for decay muons, and consequently a limited intensity.

A 300 GeV (or 400 GeV) extracted proton beam from the Fermilab accelerator impinged on a 30 cm aluminum target (Fig. 2a). The secondaries produced in the resulting interactions were strongly focussed by a triplet of quadrupole magnets Q1 into a 400 meter evacuated decay pipe. The beam-line had four bending stations D1-D4, with a total bend at each station of 27 mr. Station D1 consisted of 4 dipole magnets of aperture 10 cm x 10 cm; stations D2 and D3 consisted of 3 dipole magnets each with apertures of 10 cm x 5 cm; station D4 consisted of 3 dipole magnets with aperture of 10 cm x 10 cm. These bends served to momentum select the muons and to separate the muon beam line from the neutrino beam line. The beam coming out of the 400 meter decay pipe was bent at D1, refocussed by quadrupole doublets Q2 and Q3 and bent again at D2. The gap in the dipole magnets at D3 contained approximately 23 meters of high density polyethylene. This absorbed the hadrons that had not decayed so that the beam emerging from D3 was a highly pure muon beam. The estimate of the residual hadron contamination of this beam is described below. The beam was further refocussed at Q4 and bent at D4 into the Muon Laboratory. The bending station at D4 was also used for momentum tagging the muon beam, while the quadrupoles Q4 focussed the beam onto the experimental target in the laboratory.

Since muons have great penetrating power, there was some probabilility that muons bent or multiple scattered out of the beam line would enter the Muon Laboratory. These were the so-called halo muons. The beam line was designed with four bending stations to try to minimize the halo muon rate. Dipoles D1 selected the desired momentum of the muon beam, while those at D2 acted as a momentum slit and bent the momentum selected muons away from

the halo muons of all other momenta. Very few of the unwanted muons from this point reached the Muon Laboratory.

The muon beam was then focussed onto the polyethelene hadron filter placed in bending station D3. Muons leaving the beam line because of multiple scattering in the filter were the prime source of halo muons observed in the Muon Laboratory. The bend at D3 reduced this effect. The halo due to multiple scatters in the filter could have been reduced by shortening the length of the filter, but its length was dictated by the desire to keep the pion contamination to a minimum.

In the laboratory, the number of halo muons was of the same order as those in the beam. The beam was measured in an aperture with a diameter of 12 cm, while the halo was measured in an area 4m x 2m. The final definition of the beam was achieved electronically, to the point where the effects of the halo were quite manageable.

The most forward muons from the decays of high energy pions and kaons take almost all the parent energy so that maximum yield is obtained if all parts of the beam line are set to the same momentum (apart from an allowance for the energy loss in the absorber). This process of selecting forward decays produces muons with helicity ± 1 depending on the electric charge. The beam-line selected positive muons since this gives a more intense beam. The sign of the charge is irrelevant to the scattering process if the one photon-exchange assumption is correct. The helicity does not affect the inclusive measurement, as the target was unpolarized.

A pion in the muon beam could fake a muon scatter if it interacted in the target and one of the interaction secondaries decayed in flight before the hadron absorber (see Section III.8). Calculations predicted a

trigger rate of 10^{-2} per incident pion. To reduce the incidence of such fake events to less than one per thousand muon scatters required a pion contamination of less than 10^{-7} per incident muon. To test that this rate was attained, the fraction of the beam which failed to penetrate the 2.4 m of steel hadron absorber was measured as a function of the thickness of the polyethylene absorber in D3. This fraction contains two elements: a) pions in the beam and b) positrons from muon decay occuring after the D3 absorber. Positrons account for almost all this fraction at thickness 23 m, so that a correction can be made to fractions at less thickness where the pion effect is appreciable. Fig. 3 shows this pion fraction as a function of thickness. The attenuation length is 111 ± 6 cms. Extrapolating to 23 m from the observed pion fraction at 12 and 15 m gives a real beam pion fraction of 10^{-7}. This gives the required 1 pion interaction to 10^{3} muon interactions averaged over all the accepted kinematics. In certain regions of Q^2 and ν the contamination could reach 10^{-2}. This was ignored.

The trajectory of each incident muon was measured at four points: one just after Q4, the second 70 m downstream, just before D4, one just after D4, and the last 31 m further downstream about 3 m before the target (Fig. 4). The x coordinates were measured at all points but the y coordinates were only measured after D4. The measurement was made with multiwire proportional chambers (MWPC, Fig. 4), combined with light-element scintillation counter hodoscopes (BH1-6, Fig. 4), which covered the active area of the MWPC. The angle of bend in D4 was determined to a precision of 0.03 mr giving a 0.1% error in momentum at 150GeV. The system also gave the transverse position of the muon at the target to a precision of 1/2 mm.

For the purpose of triggering, muons in the beam were defined by a telescope of scintillation counters T1, T1A, T2, T3 centered on the beam line

(Fig. 4) and by veto counters V_s and V_j which eliminated from the defined beam any muons scattering from the D4 magnet pole tips. In the 219 GeV running the beam telescope of T counters was discarded and the signals from the beam counter hodoscopes were used in an appropriate coincidence.

Typical plots of the phase space of the incident beam are shown in Figs. 5 (a-d).

III.2 The target

The target flask was 18 cm diameter and 120 cm long. It could be filled with liquid hydrogen or deuterium (see Fig. 6); this represented 8.5 g/cm^2 of H_2 or 20.3 g/cm^2 of D_2 to be compared with 0.63 g/cm^2 of flask material. The upstream vacuum jacket window was sufficiently far from the flask to allow separation of events in which the muon scattered from the window material from events where the muon scattered in the flask or its contents.

III.3 The upstream multiwire proportional chambers

Immediately downstream of the target and before the spectrometer magnet (hence 'upstream' relative to the magnet center) was a set of eight 1 x 1 m^2 multiwire proportional chambers. These chambers were arranged with alternate vertical and horizontal wire planes, giving four x and four y coordinates on the trajectory. The wire spacing in the proportional chambers was 1.5 mm giving a resolution (r.m.s.) of 0.5 mm. The latch gate width was set at 100 nsec. These chambers were used to measure the tracks of charged particles emerging from the muon interaction, and to determine the position of the event vertex.

III.4 The spectrometer magnet

The spectrometer magnet was the rebuilt magnet of the University of Chicago 460 MeV synchrocyclotron (CCM in Fig. 6). The main change was an increase in the gap to 129 cm. The pole tip radius was 216 cm. The field reached 1.5 Tesla at an excitation current of 5000 A. At this current, the $\int$Bdl was

7.5 Tm corresponding to a transverse momentum kick of 2.25 GeV. The magnet polarity was set to bend positive particles in the negative x direction.

The field was measured in detail using three orthogonal Hall probes. The magnet volume was very large and extensive measurements were only made in the useful regions of the magnet and at a central field of 1.5 T. Less extensive measurements were made at lower excitations. The measurements had a precision of better than 10 gauss; the central value of the field is thus known to 0.1%. The field was found to have a high degree of symmetry (better than 1% both cylindrical and for reflections in the median plane). This circumstance allowed a simple model of the magnet to be used in track reconstruction and momentum determination.

III.5 The downstream spark chambers

Downstream of the magnet were four groups of spark chambers (Fig. 6). The first three were 4 x 2 m^2 shift-register[25] read-out chambers, the last group was a set of 6 x 2 m^2 magnetostrictive read-out chambers. All chambers were placed perpendicular to the z axis and had wire spacing of 1.25 mm leading to a resolution of 0.3 to 0.5 mm in the read-out direction. The wires were arranged either vertically (x) or at an angle of $\pm\tan^{-1}(1/8)$ to the vertical (u,v). Each of the first three groups were arranged as (uxxv). The last group was arranged (uxuxvuxv) making a total of twenty planes.

The shift-register readout chambers were sensitive in the region around the beam, where there were many "stale" tracks, but the magnetostrictive chambers had a region of 20 cms diameter which was deadened by a plastic sheet in the gap.

This system provided the information required to determine the direction of charged particles which had passed through the magnet and had momentum greater than 7 GeV. The directional resolution attained was 0.3 mr.

The arrangement of the last group of chambers provided a convenient set of track coordinates on which to start track reconstruction, for two reasons. Firstly, the tracks were well separated and most easily distinguished at these planes, and secondly, their compactness in the z-direction allowed fast computer algorithms for track finding in projected roads within the chambers.

III.6 The trigger and timing scintillation hodoscopes, G and H

Immediately downstream of the 6 x 2 m^2 magnetostrictive spark chambers were two large scintillation counter hodoscopes, G and H. The sizes and disposition of their elements is shown in Fig. 7. The H hodoscope had twenty-four vertical elements, overlapping by 1 cm, and covering an area of 4 x 2 m^2. The hodoscope was deadened in the beam region by replacing the scintillator by perspex in the central 30 cm of the central two elements. The G hodoscope covered an area 6 x 2 m^2 with eighteen horizontal, slightly overlapping elements. One of the central G counters was moved outwards to leave a gap for the deflected beam. Two extra counters not shown in Fig. 7 covered this beam region. This arrangement was used at 96 and 147 GeV. At 219 GeV the arrangement was changed slightly: the H hodoscope was made wider by the addition of extra counters at either end and near the center. The hole in G had to be moved to accomodate the higher energy beam.

These hodoscopes played two roles. First they were part of the trigger system described in Section IV. Second, their time resolution was 30 ns, which allowed time as well as space masking of the tracks found in the downstream chambers. This masking was an essential part of the definition of event-associated tracks.

III.7 The photon and neutral hadron detectors

Behind the G and H hodoscopes there were two systems of detectors.

The first consisted of 3 radiation lengths of steel followed by a set (uvuxuxuv) of magnetostrictive spark chambers, 4 x 2 m^2 (Fig. 6). Electrons or photons striking the steel wall had a good chance of starting an electromagnetic shower which showed in the spark chambers as a very large number of sparks. In fact the system was not used to detect photons but was used to help identify electrons in an investigation of the effects of the background of μ-e scattering at very low Q^2.

The second consisted of a 40 cm thick lead wall followed by a set of 4 x 2 m^2 magnetostrictive chambers (xvuxxv)(Fig. 6). This thickness of lead provided almost complete absorption of electromagnetic showers but was of the required thickness to start nucleon cascades. This combination was designed to make possible the detection of neutral long-lived hadrons and check on the hadron versus muon separation in the rest of the equipment. However, the high density of stray sparks made it impossible to use it as a detector. It was, however, used in combination with the "photon" detector described above to help identify electrons and was also used to identify triggers caused by beam positrons in random coincidence with halo muons.

III.8 The hadron absorber

Muons were identified by their ability to penetrate a steel wall 250 cm thick (Fig. 6). This represents 15 hadronic interaction lengths: this did not completely eliminate the effects of the most energetic hadrons. However, effects due to mis-identification of hadrons as muons are insignificant (<1%).

III.9 The muon counter hodoscopes, M and M', and the beam veto system

The M and M' hodoscopes had respectively horizontal and vertical elements; their layout is shown in Fig. 8. The central elements on the negative side were smaller vertically than the other counters because they covered the region where the majority of scattered muons appeared. All the central elements were mounted on a trolley which permitted movement in the x direction so that the beam hole position could be adjusted. The width of this hole was also adjustable, as were the heights between the elements of M'. These hodoscopes were used as a part of the trigger system; in the analysis they provided time and space masking of the muon spark chambers.

The N hodoscope was an arrangement of 13 counters (each 66 x 7.5 x 2 cm^3) arranged as shown in Fig. 8. This hodoscope was designed to fill the gap in the M hodoscope and was used as a beam veto counter for part of the 147 GeV running. To improve the acceptance at low ν and moderate Q^2, it was replaced in its veto action by 3 totally overlapping counters, each 30 x 23 x 0.6cm^3 called collectively the K counters. In this mode the middle N counters were only latched while the outer ones not overlapping K could be added conceptually and operationally to the M. This allowed the muon acceptance to be pushed vertically nearer to the beam. A reference to M includes these particular counters of N. This arrangement was used for the 96 and 147 GeV runs of 1975.

At 219 GeV, the three counters of the K were replaced by a hodoscope, consisting of eleven scintillation counters 30 x 5 x 2.5cm^3 arranged with 50% overlaps, and an additional counter which covered the area between the hodoscope and the active area of the M. We shall refer to both veto arrangements as K.

III.10 The muon spark chambers

Behind the muon hodoscopes was placed a set of eight, 4 x 2 m^2 magneto-strictive spark chambers (uxxvuvux). The chambers and hodoscopes were displaced to the negative x direction (the direction in which the spectrometer magnet bent the scattered muons) in order to maximize the acceptance.

IV. The Trigger and Data Logging

The experimental trigger required that three conditions be simultaneously fulfilled. These were:

1. The observation of an incident beam particle within the beam acceptance. This condition was satisfied by signals from the beam telescope in coincidence (B).

2. The observation of a scattered muon in the acceptance of the apparatus. This condition was satisfied by a coincidence of signals from the downstream hodoscopes, G, H, M, M'.

3. The observation that the incident muon had left the beam before it arrived at the back of the apparatus. This condition was satisfied by the absence of a signal from the beam veto K.

All three conditions were necessary to achieve an acceptable trigger rate. The beam contained positrons which satisfied (1) and (2) at the rate of about 2×10^{-4} per incident muon. The beam halo could satisfy (3) by accidental coincidence with a beam particle at a rate of about 3 to 5×10^{-2} per incident muon. The inclusion of G and H in (2) prevented beam muons which scattered in the hadron absorber and struck M or M' rather than K from appearing in the trigger as real muon scatters. The three requirements taken together provided a trigger which occurred at the rate of 6 to 10×10^{-6} per incident muon. The target associated trigger rate was visible at about 1×10^{-6} if a full-empty subtraction was done with adequate statistics.

Events which contributed to the remaining trigger rate included:

1. Positrons in the beam (from μ decay) firing B and G in random coincidence with M or M'.

2. Muons interacting in the iron hadron absorber and firing B and M in random coincidence with G.

(These random coincidences were usually coincidences with an unvetoed halo muon which fired one of the G, M or M' hodoscopes.)

3. Muons of low energy which scattered in or near the final bending magnet, satisfied the beam trigger requirements, and were bent by the spectrometer magnet into the trigger acceptance.

The exact definition of the trigger satisfying all conditions was

B $\bar{K}$ G (M or M') used at 96 and 147 GeV

B $\bar{K}$ (G or H)(M or M') used at 219 GeV

where

1. B was a coincidence between the beam telescope counters T1-3, T1A and an anticoincidence from any of the veto counters V_s, V_j or the $2 \times 4\,m^2$ halo veto hodoscope V_w (Fig. 4). There was also an additional constraint applied. The beam had the structure of the RF accelerating frequency of the main ring. This meant that muons appeared at the apparatus in RF "buckets," 18.8 ns apart and 2 ns wide. No muon was accepted unless it was alone in its bucket; "alone" means that each of the beam hodoscopes BH2-6 had only one counter firing. This was done so that there would be no loss of events due to extra muons vetoing such events by hitting K. In addition no muon was counted or used which had a muon in the preceding RF bucket. This was done to avoid the effects of inefficiencies due to dead time in the K veto system. These could occur in the following manner: muons emerging from the hadron wall were frequently accompanied by extensive electromagnetic showers which might disable the K system for a period greater than 18 ns; the second muon could then satisfy the first trigger condition and a random coincidence due to a halo muon would complete an unwanted trigger.

2. $\bar{K}$ was the absence of a signal in any element of the K counter system.

3. (G or H) was the presence of a signal in any counter of the G or H hodoscope.

4. (M or M') was the presence of a signal in any counter of the M or M' hodoscope. As mentioned M sometimes included some elements from the N hodoscope.

The beam telescope resolving time was 10 ns, the V_s, V_j and K veto resolving time was 15 ns and the halo veto hodoscope V_w resolving time was 25 ns. The resolving time of the remainder of the trigger system was set by the need to accomodate the transit time of light (20 ns) in the longest counter elements (3 m) which were those of the G hodoscope. Thus the overall resolving time on $B\bar{K}$ (G or H) (M or M') was about 30 ns.

In addition to the basic trigger as described, the apparatus was also triggered on a small fraction of the beam muons; 1 in 2^{20} (10^6) changed to 1 in 2^{22} for part of the 219 GeV running. These embedded beam triggers provided an unbiased sample of beam well interspersed within the data, which was used to calculate the incident muon tagging efficiency and to determine the phase space of beam potentially able to scatter.

Other triggers were used for special purposes. Particularly useful was the "halo" trigger which was a coincidence between the halo veto hodoscope, the G hodoscope, and the H hodoscope. This provided many tracks passing straight through the apparatus which were useful for alignment purposes.

A trigger set in motion a sequence of events. The first was to close the gate to a set of scalers counting various coincidences, in particular one counting the incident beam (B). At the same time the spark chamber firing sequence was initiated and the gate to counter latches opened for a suitable time to record which counters were fired in the trigger. When the spark chamber data was digitized, the on-line computer, a Xerox Sigma-3, initiated

the reading of all spark chambers, MWPC, scaler and other relevant information. These data were organized, sorted into records and stored. At the end of the beam spill all the events accumulated during that spill were transferred to magnetic tape.

The computer was also employed on many monitoring services which allowed continuous checks to be made on the operation of the equipment.

Data taking normally involved both target full and empty runs in the ratio of about 8 to 1 in exposure. However, changeovers were not frequent because the target emptying time was several hours.

V. Event Reconstruction

The process of data reduction took place in several stages, the objective being to produce a library of events which contained for each the track-finding, track-linking and preliminary vertex data in addition to scaler and counter latching information. This tape was used as a source for all physics data analyses.

The stages of this reduction are conveniently labelled by the name given to the magnetic tapes produced, viz. Primary, Secondary and Tertiary.

V.1 The production of primary tapes

The records from the raw data tapes were checked for simple errors that might have occurred during data logging. Bad records were removed and corrected records written on to the primary tapes.

V.2 The production of secondary tapes

The purpose of the secondary tapes was to provide a record of all events in which the scaler and counter latching data were unpacked and arranged into a convenient format and in which all spark and MWPC coordinates were

in real x, y, u, v, etc., coordinate space. The latter required a thorough alignment procedure to maintain the apparatus resolution over long periods of time.

Some runs were available in which events were recorded with a simple beam trigger (B, section IV) and with the spectrometer magnet switched off. The beam tagging system after D4 was used to define the coordinate system of the apparatus so that these straight-through muon events could be used to fix the central alignment of the detectors to 0.5 mm.

This procedure was adequate to align completely the upstream MWPC but the downstream spark chamber system required more attention.

To align the system, halo muon tracks and real event tracks were used in addition to beam events. Members of groups of chambers were aligned relative to each other. Then all groups were aligned within the apparatus as a whole. In addition the chambers using magnetostrictive readout were examined for non-linearities. These were the exception, not the rule, and were easily removed by a simple parametrization of the deviation. These procedures depended on track finding and fitting followed by minimization methods designed to eliminate deviations due to misalignments.

These alignments and the changes in magnetostrictive corrections were conducted on a run to run basis by means of a four-pass procedure using the first three or four hundred events on each primary tape. In this way the chambers demonstrated and maintained their theoretical resolution of about 0.5 mm in spite of effects due to temperature variations, floor sinkage near

the hadron absorber, and ageing.

Once the chambers were aligned, the program calculated event by event the real space positions and widths of all sparks and MWPC hits, combined these withcounter latch and scaler data and wrote the events on the secondary data tape.

The apparatus efficiencies were monitored on a run by run basis. Any run which had a part of the apparatus running at a grossly impaired efficiency was rejected at this stage.

V.3 The production of tertiary tapes

This stage of the data reduction was concerned with track and vertex finding. It used the secondary tapes as source and wrote the results on a tertiary tape. It was designed to find all tracks, all secondary muons, and their vertices and to make track and vertex linkings. No cuts were applied except to probabilities in track fitting so that no bias was built into the program. The tertiary tapes became the source for later programs which made the final muon selection.

The analysis programs were divided into nine separate tasks:

i. beam tagging

ii. upstream MWPC trackfinding

iii. muon chamber trackfinding

iv. downstream chamber trackfinding

v. linking upstream MWPC tracks to downstream spark chamber tracks

vi. track recovery

vii. linking to muon chambers

viii. vertex finding

ix. calculation of kinematic quantities

i) The beam tagging system. Information from the beam hodoscopes and multi-wire proportional chambers was combined to provide the most efficient beam track reconstruction consistent with precision on the momentum, position and direction of the incident muon. This meant that at stations at D4 or Q4 the absence of either a chamber hit of a counter hit did not eliminate the event. Only at the station just upstream of the target was it necessary to demand a chamber hit in both coordinates in order to preserve positional accuracy. The trajectory reconstructed upstream and downstream of D4 was required to link within 1 cm at the center of D4 (r.m.s. deviation was 0.15 cm) and to lie inside the aperture of these dipoles at their entrance, center and exit.

ii) The upstream MWPC trackfinding. The data were analyzed using the 8 planes before the magnet. Trackfinding was done independently in the xz and yz planes. In each view tracks were required to have three or four wire hits and to point back to the target region. A 2% probability cut eliminated inappropriate fits. In the case of two tracks sharing two or more wire hits, that with the highest x^2 was rejected.

iii) Muon chamber trackfinding. These chambers were some distance from the magnet and target so that, except for the beam region, tracks were well separated and generally pointing back towards the magnet center or parallel to the beam. In addition, the chambers were close together. Correlated (x, y) points were found from the two planes in each of the four chambers. A search starting from one such point required that only a small range of x coordinate in the neighboring chambers be examined. Groups of three or more x sparks were fit to a straight

line; the tracks were accepted on a simple χ^2 cut. For every track found in the xz projection, a search was initiated among the associated y values in order to find its yz projection.

iv) Downstream spark chamber trackfinding. These chambers were spread over a large range of z and trackfinding was complicated by the large numbers of sparks not related to the events. Trackfinding started in the 6 x 2 m^2 magnetostrictive chambers using a technique identical to that used in the muon chambers. This allowed the definition of track roads upstream into the 4 x 2 m^2 chambers, which were searched, plane by plane, for contributing sparks. Once all sparks were found, the entire track was fitted using the data from each plane (x, u, or v) separately, and a χ^2 cut was applied to remove bad tracks. A minimum of three sparks in the 4 x 2 m^2 chambers and a minimum of eleven total sparks was set for downstream tracks. If the track failed these requirements, the line of search in x was allowed to swing, fixing the position of the track at the center of the 6 m chambers, and changing its position at the most upstream of the shift-register readout chambers. A first pass swung the track by 1.5 cm, a second pass by 2.5 cm. These swings were only necessary for about 10% of the successful tracks.

v) Upstream-downstream linking through the magnet. The cylindrical symmetry of the spectrometer magnet meant that the impact parameter in the xz plane of an upstream particle trajectory was equal to that of its downstream trajectory. Apart from the effects of edge focussing and the helix geometry of the track in the magnet, both of which are small, the projected slope of the trajectory in the yz plane is the same before and after the magnet. The distributions of the observed difference for unique links have r.m.s. deviations of 2.3 mm in x, 7 mm

in y and 1.3 mr in dy/dz. Links in the xz plane were accepted if the difference in x impact parameters was less than 8.8 mm. Links in the yz plane were accepted if

$$\left[\frac{\delta\left(\frac{dy}{dz}\right)}{6 \times 10^{-3}}\right]^2 + \left[\frac{\delta(y)}{2\ \text{cm}}\right]^2 < 1$$

This assumed, as was almost the case, that the differences were uncorrelated. (δ stands for the upstream-downstream difference.)

vi) Track recovery. Once initial upstream-downstream linking had been completed two extra track searching routines were activated. The first was designed to remove inefficiencies in the upstream track reconstruction due to the lack of redundancy in the MWPC system. It took any missing link in the x and/or y view and projected it back through the magnet to the beam muon position at the center of the target length. The upstream chambers were searched for any two point tracks near this line. Approximately 15% of xz and yz tracks in the upstream chambers were such two point tracks.

The second recovery routine was designed to remove inefficiencies in the downstream track reconstruction. The impact parameter of MWPC x tracks which did not link to any downstream track and (x, y) sparks in one of the downstream chambers were used to form a road. If sufficient sparks were found in the road, they were fitted, and the resulting track was added to the track buffer if it was not a duplicate of a previously found track. If insufficient sparks were found, then the road was allowed to swing by 5 mm in a manner similar to that of the primary trackfinder.

In the 96 and 147 GeV running, the sparks were taken from the 6 m chambers, and the algorithm went to the next MWPC track on finding a new

downstream track. In the 219 GeV running, all combinations of tracks and sparks from the four downstream-most shift-register chambers were used as seeds. In both cases, the initial road was required to point in the direction of a lit G or H counter.

vii) Downstream-muon chamber linking through the hadron absorber. All tracks in the muon chambers were tested for linking to all tracks in the downstream chambers. A good link satisfied criteria designed to find in the downstream chambers those trajectories which were due to muons. The muons were the only particles which could penetrate the hadron absorber but in doing so they suffered multiple scattering. This effect increased with decreasing muon energy so that the linking criteria had to take into account larger deflections and displacements at lower energies. A link was accepted if the following criteria were satisfied:

a) The difference in slopes dx/dz was less than S x 12.5 mr

b) The difference in x coordinates at a z which is the effective multiple scattering center was less than S x 38 mm

c) The difference in y coordinates at the muon chambers was less than 188 mm.

The number S is the multiple scattering factor: it was 1 near the beam and increased approximately linearly with x to a figure of about 9 at the x point where 15 GeV muons were detected. The cuts in (a) and (b) are at 7 standard deviations. The cut in (c) is large to accomodate the poorer direction finding ability in the vertical plane.

viii) Vertex finding. Each muon candidate was used to find a vertex with the beam by fitting its MWPC links and the beam track to a vertex. If there was no y link in the MWPC, the downstream y track was used. Any other MWPC tracks which pointed at the muon-beam vertex were included in a subsequent fit to improve the vertex location and resolution.

ix) Calculation of kinematic quantities. Momenta were calculated for intime tracks linking through the magnet in the following way. The vertex was located and a line drawn to the impact parameter of the track in the center of the magnet. This line and the incident muon direction gave the scattering angle; the position of the track in the 6 m chambers and $\int Bdl$ for the magnet then gave the momentum. The values of Q^2 and ν were then calculated for all muon candidates. These values were written on the tertiary tape but normally better values were calculated later.

The data from track finding, track linking, vertex finding and the kinematic calculations were written on the tertiary tape along with scaler and counter latching information which was transferred intact from the secondary tapes. These tertiary tapes were used as sources for various efficiency and physics programs.

VI. Event Selection and Corrections

This section deals with the production of the sample of good events, the calibration of the spectrometer and the calculation of the muon kinematics.

The linking requirements established at the tertiary tape production stage left a sample of muons contaminated by out-of-time halo muons. To purify this sample every muon candidate track was projected onto all hodoscopes. At each hodoscope a successful hit was flagged if at least one element was latched and this element was one that could have been struck by the particle. To allow for multiple scattering and errors in the counter positions and track coordinates, each element was expanded 3.75 cm at each x boundary and 7.5 cm at each y boundary. At the muon chambers a track could hit any number up to three hodoscopes (M, M' and N) and was declared to be an in-time muon track if the success rate was 3/3, 2/3, 2/2, 1/2, 1/1.

In the downstream section for the 219 GeV data the hodoscopes were G and H, and the in-time downstream track declaration required 2/2. For the 97 and 147 GeV data, G was standing alone and the requirement was 1/1. Downstream tracks were also projected through the hadron shield, and with an additional allowance for multiple scattering, were flagged if an appropriate M, M' or N element had been latched.

There are two classes of track which were acceptable muons. The common criteria were:

a) Track must have an upstream to downstream link.

b) Track must be declared in-time downstream.

Then the two classes are defined by:

1) Track-linked: the downstream track links to an in-time muon track.

2) Counter-labelled: the downstream track is in-time at the muon hodoscopes, as defined above, and points to a cluster of sparks in the muon chambers. Downstream tracks which link to out-of-time muon chamber tracks are considered to be counter-labelled if they are in-time at the muon hodoscopes.

85 to 92% of all events containing a muon were track-linked. The remainder were counter-labelled or contained two muon tracks linked to the same downstream track; in the latter case the downstream track defined the muon. About 1.5% of the events contained two muon candidates, in which case track-linked was chosen in preference to counter-labelled. Failing this the best upstream-downstream track linking signaled the preferred muon. In the 219 GeV data, there were more extra tracks due to the change in the track-finding routines and an additional level of choice was added. If the linking

signature was the same, then the choice was based on the number of sparks in the track. The number of multi-muon events is consistent with the hypothesis that they come from the decay of secondaries produced by the scattered muon. The procedures used to choose the muon made no use of this information, being designed to eliminate halo muons which were accidentally in-time and linked upstream. This implies that the hadron decay muon will be chosen over the real scattered muon in some half the multi-muon events. The resulting Q^2 depends on both the muon and hadron kinematics, and can be either larger or smaller than the Q^2 of the real scattered muon. The net correction to the cross section is thus less than 1% and was ignored.

The vertex was redetermined using the scattered and incident muon tracks alone. This vertex was used in making vertex cuts in the final stages of the analysis, in order to eliminate a possible systematic effect. Events which produced hadrons would have smaller vertex errors due to the inclusion of the hadron tracks in the vertex fit, thus resulting in a bias unrelated to the muon kinematics. To remove any effects of this bias, the scattered-incident muon vertex was used. Figure 9 shows the z-distribution of these vertices. The target stands out clearly.

VI.1 Calibration of the Spectrometer

The accuracy of the momentum calculation was dependent on two pieces of information. The first was knowledge of $\int Bdl$, which was known for both magnets, D4 and the CCM, to better than 1%. The current drawn by each magnet was monitored during the running, and any run-to-run drifts were taken into account. The second was knowledge of the bend angle, which was measured by using the position and the track reconstructed in the downstream chambers. However, the angles measured depended on the accuracy of the alignment, which could introduce, via a rotation of

one part of the apparatus with respect to another, misassignment of momenta. A calibration was therefore done which took two stages and corrected for three systematic effects. These were:

1) A relative rotational misalignment between the upstream and downstream apparatus. This affected the momenta of positive and negative particles oppositely.

2) A relative miscalibration of the D4 magnet and the spectrometer magnet, which had a very large effect on ν, the muon energy loss, for small values of ν.

3) The absolute calibration of the spectrometer magnet.

The effects 1 and 2 were corrected by using the large number of elastic μ-e scattering events and the embedded beam events (which can be classed as μ-e scatters in which no energy is lost). The opposite effects in 1 and 2 allowed them to be separated and a small correction factor found which corrected all momenta to that which would be measured by the spectrometer magnet. The absolute calibration was done by again using μ-e events. Those scatters which were "elastic" within the apparatus resolution were in principle over determined. The angle of scatter can be predicted from the muon energy loss and measured from track coordinates. Since the value calculated for the muon energy loss, after effects 1 and 2 have been corrected, depends directly on the spectrometer calibration assumed, an absolute calibration was obtained by minimizing the square of the difference between the predicted and observed angles over a large number of events.

The procedure also provided the figures for the apparatus resolution. For the momentum, the r.m.s. deviation σ_p is given by $\sigma_p/p = 1.4 \times 10^{-4}\ p$ where p is in GeV. For the scattering angle the r.m.s. deviation is 0.32 mr. The resolution in ν varies and its effects are considered in Section VI-8.

VI.2 Data cuts

Several cuts were made to this data sample which are enumerated below.

(a) Some parts of the apparatus had little redundancy so that any malfunction had an immediate effect on efficiency. Preliminary filtering for gross inefficiency was done at the secondary tape stage but less obvious changes were also present. Of particular importance were the downstream and muon spark chambers. Runs were rejected if the mean number of sparks in the downstream chambers per track was less than two standard deviations above the least number of 11 sparks, the requirement employed during track finding. Similar checks were applied to the muon chambers. The upstream and MWPC chambers were monitored for efficiency so that it was possible to retain all runs unless there was a gross malfunction.

(b) All muon scattering events were required to satisfy the following geometric criteria:

i. The incident muon trajectory had to be inside the target along the latter's entire length.

ii. The vertex calculated using the scattered and incident muon was used for a target cut. Events were accepted if the vertex was inside the target with an error of 3 standard deviations.

iii. The scattered muon was required to be inside the geometric acceptance of the trigger and to point outside the deadener in the 6 x 2 m^2 spark chambers.

(c) μ-e scatters must be eliminated from the data. Events in which only the scattered muon and one negative particle were reconstructed downstream and where there was no excess activity in the MWPC were examined further. If the event

appeared elastic within 15%, or had a very low p_T for the negative particle, it was declared to be a μ-e scatter and was removed from the data sample. This program was about 80% efficient and had a negligible effect on hadronic events. It left a contamination in the hadronic events estimated to be about 6% in the range $0.2 < Q^2 < 0.3$ $(GeV)^2$ and about 3% in the range $0.3 < Q^2 < 0.6$ $(GeV)^2$ in the 147 GeV data. The estimates are 10% for $0.3 < Q^2 < 0.6$ $(GeV)^2$ in the 219 GeV data. For all other kinematic regions and for the 96 GeV data the contamination is less than 0.5%.

(d) After all the above cuts have been made the trigger rate was calculated for all the muon scattering events, including the effect of beam reconstruction efficiency (see Section VI.4). Any run having a rate more than three standard deviations from the mean had its contribution removed from the sample.

VI.3 Basic formulae

The results are presented in bins of the kinematic variables: e.g. (Q^2, x). We specify a pair of general kinematic variables (α, β) with a bin $(\Delta\alpha, \Delta\beta)$, and a quantity $Q(\alpha, \beta)$ related to the differential cross section by $d^2\sigma/d\alpha d\beta = K(\alpha, \beta)\, Q(\alpha, \beta)$. Then the bin-centered value $Q(\alpha_o, \beta_o)$ is

$$Q(\alpha_o, \beta_o) = \frac{W}{L\epsilon \int_{\Delta\alpha}\int_{\Delta\beta} \frac{Q(\alpha, \beta)}{Q(\alpha_o, \beta_o)} \left[\frac{K(\alpha, \beta)}{RC(\alpha, \beta)\ SC(\alpha, \beta)}\right]} \qquad (8)$$

Here, L is the luminosity, ε is an efficiency factor independent of α and β, RC is the radiative correction, and SC is the correction for finite resolution. The quantity W is a weighted event sum:

$$W = \sum_i \frac{1 - P^{MT}(\alpha_i, \beta_i)}{A(\alpha_i, \beta_i)\, E(\alpha_i, \beta_i)} - N_{ert}(\Delta\alpha, \Delta\beta) \qquad (9)$$

$$\equiv W_{sum}(\Delta\alpha, \Delta\beta) - N_{ert}(\Delta\alpha, \Delta\beta)$$

where the sum runs over the events in the bin; F^{MT} is the empty target fraction, A is the geometric acceptance, E is an efficiency dependent on the kinematics, and N_{ert} is the number of elastic radiative tail events (see Section VI.10) calculated for the bin. Equation 8 is used iteratively; an analytic form for $Q(\alpha, \beta)$ based on previous data is assumed, the values of $Q(\alpha_o, \beta_o)$ are found and a new fit to $Q(\alpha, \beta)$ is obtained. The procedure is repeated until the fit does not change significantly. This procedure is necessary only at low ω where the structure functions are rapidly changing.

This method is used to determine the values of $F_2(Q^2, x)$, as reported below. The determination of the other terms is discussed in the following sections.

VI.4 The luminosity

The luminosity L is the number of incident muons times the number of nucleons in the target per unit area perpendicular to the beam axis. The first number is found from the gated scaler which counted the incident muon beam and the second from the target dimensions and liquid density.

VI.5 The kinematic independent efficiency

The efficiency ϵ contains six factors. Each is described below and the values given in Table III.

1. ϵ_1 is beam reconstruction efficiency. The embedded beam triggers are unbiased by the muon trigger. The fraction of these triggers in which the incident muon is successfully reconstructed gives ϵ_1.
2. ϵ_2 corrects for the effect of two muons appearing in one RF beam bucket. If one scattered, the event was lost since the second would strike the K veto. This effect was suppressed by the trigger arrangement (see Section IV) but remained so that $(1 - \epsilon_2) = 1\%$ in some

of the 147 GeV data but is negligible in the rest.

3. ϵ_3 corrects for the downstream spark chamber inefficiencies. Asking for 11 sparks or more is estimated to lose 0.5% of the events.

4. ϵ_4 corrects for the efficiency of the upstream MWPC. This was measured by using a class of "perfect" downstream muons and asking how often they linked with tracks upstream. In the case of both ϵ_3 and ϵ_4 the overall gross inefficiencies have been removed earlier (Section V.2). The methods of calculation take account of possible event to event correlated inefficiences.

5. ϵ_5 is the correction for counter efficiency as it affects the trigger and reconstruction.

6. ϵ_6 corrects for over-subtraction of background because of the existence of hydrogen vapor in the nominally empty target.

VI.6 The geometric acceptance

The geometric acceptance $A(Q^2, \nu)$ was calculated on a net of Q^2 and ν values at each energy using a Monte Carlo program. The boundaries of the acceptance are given by the inner and outer boundaries of the hodoscopes in the trigger and by dead space inside this region owing to deadeners and the spark chamber boundaries, all smeared by multiple scattering. Counter positions were determined from survey and from a program which used tracks to determine boundaries between hodoscope elements. The Monte Carlo events were generated using as incident particles the trajectories given by the embedded beam triggers.

Figure 10 shows the acceptance at each of the three energies. The contours shown are determined essentially by the size and shape of the muon hodoscopes. Since the CCM preserves impact parameters, the locus of the events having a fixed (Q^2, ν) is approximately a circle on the plane of the muon hodoscopes, smeared by the finite size of the beam and target. Figure 11 shows some representative unsmeared circles, for the 219 GeV data.

VI. The kinematic dependent efficiency

The efficiency $E(\alpha, \beta)$ takes account of two effects. The first is due to trackfinding inefficiences in the region of the beam in the downstream chambers. This effect was measured by taking data from a real event and planting an extra track by a Monte Carlo method which simulated known inefficiencies and spark spreads. This modified event data was subjected to the track finder and the success rate in finding the planted track measured the efficiency. Fig. 12 shows this efficiency as a function of position across the $6 \times 2\ m^2$ chambers. The effects can be parametrized with a maximum error of 30% of the inefficiency. The low ν bins are worst affected with a maximum error about 6% due to the error on this correction.

The second effect is called the K-veto showering or "suicide" correction. A fraction of events with the muon inside the geometric acceptance were self vetoed when a delta ray or a part of the electromagnetic shower, which often emerged with the muon from the hadron shield, struck one or more of the K-hodoscope elements. This was an important effect for the part of the acceptance which was close to the K-veto. The effect was quantified by examining the distribution of multiple hits in the N-hodoscope for embedded beam triggers. The systematic error due to this correction is about 1%.

VI.8 Background subtraction

The background subtraction was done by using $F^{MT}(\alpha, \beta)$ which is the ratio of target empty to target full yield at a normalized incident beam. For the 96 and 147 GeV running, the background was fit to the form

$$F^{MT}(\nu, Q^2) = (C_1 + C_2\nu + C_3\nu^2)(1 - 3x/8),$$

$$x = Q^2/2M\nu.$$

The factor $(1 - 3x/8)$ allows for the fact that the target flask material is

deuteron-like. Fig. 13a shows the data and fit for the 96 GeV data. The 219 GeV data had better statistics and allowed the value of $F^{MT}(\nu, Q^2)$ to be calculated for numerous bins. It was found to behave in a simple way with Q^2, but no ν dependence was observed. The value of F^{MT} was determined for bands of Q^2 and is shown in Fig. 13b. The background fraction was not constant since the vertex resolution at lower Q^2 was poorer, and muons scattered from a greater amount of material near the target could pass the vertex cut. The systematic error in the final cross section introduced by this methods of background subtraction is estimated to be less than 3%.

VI.5 Resolution correction

Due to finite resolution the observed value of ν or Q^2 will not be the true value. This effect can be serious where there are kinematic boundaries or where the differential cross-section is varying rapidly. The observed cross-section is given by

$$\left.\frac{d^2\sigma}{d\alpha d\beta}\right|_{obs} = \int\int \left.\frac{d^2\sigma}{d\alpha' d\beta'}\right|_{true} P(\alpha,\beta;\ \alpha',\ \beta')\ d\alpha' d\beta'. \qquad (10)$$

The correction factor is then

$$SC(\alpha,\ \beta) = \frac{\left.\frac{d^2\sigma}{d\alpha d\beta}\right|_{true}}{\left.\frac{d^2\sigma}{d\alpha d\beta}\right|_{obs}} . \qquad (11)$$

$P(\alpha, \beta; \alpha', \beta')$ is the probability that an event truly having kinematic variables α', β' is seen as having α, β owing to resolution. The resolutions determined (Section VI.1) indicate that the only resolution that is serious is that on E'. Tables of values of $SC(\alpha, \beta)$ were constructed and found to be insensitive to the values of the structure function F_2 used in a true cross-section.

The resolution becomes extremely poor at very low ν so a cut on the data is made at ν = 5 GeV (ν = 10 GeV for the 219 GeV data); at the same time, the correction has a significant effect only on data with ν < 20 GeV (ν < 50 GeV for the 219 GeV data). Its maximum effect in the accepted region is 20-30%, depending on the data set, and the systematic error arising from this correction is estimated to be less than 1%.

VI.10 The radiative correction

The radiative correction factor $RC(\alpha, \beta)$ has to be calculated. The inelastic scattering of muons by nucleons is the process of interest but it is possible for the muon to radiate real photons in the target material before and after the interaction of interest (external bremsstrahlung) and during the interaction of interest (internal bremsstrahlung). In both cases the measurement of secondary energy does not yield the actual values of Q^2 and ν in the basic interaction. Thus the events in an (α, β) bin are a sample which has been depleted because, although the kinematics in the interaction had value α, β the observed muon radiated after scattering. In contrast the sample has been increased by events which had different (α, β) but radiation makes them appear to have the required (α, β). The increase also includes events from elastic scattering of muons on nucleons in which a photon has been radiated (elastic tail). Thus the observed cross-section is given by

$$\left(\frac{d^2\sigma}{d\alpha d\beta}\right)_{obs} = \frac{1}{RC(\alpha,\beta)} \left(\frac{d^2\sigma}{d\alpha d\beta}\right)_{true} + \left(\frac{d^2\sigma}{d\alpha d\beta}\right)_{tail} . \qquad (12)$$

The number of events due to the elastic radiative tail is calculated for each bin, and is subtracted from the weighted events in that bin (eq. 9). Values for the cross-section due to the elastic tail are calculated using

formulae given by Tsai.[26] The ratio of the calculated number of radiative tail events to the weighted number of observed events at 219 Gev is shown in Table IV. The method of calculating the remaining term is described by Mo and Tsai.[27] To use this method it is necessary to iterate from a starting form for $d^2\sigma/d\alpha d\beta_{true}$. The form used was a fit to the values of νW_2 from the MIT-SLAC data.[28] For the 219 GeV data the form used was a fit to the 96 and 147 GeV data. $RC(\alpha, \beta)$ was calculated and the muon scattering measurement corrected, F_2 was derived and fitted, and RC recalculated. This iteration was continued until the corrected values did not change. The value of $RC(Q^2, \nu)$ is shown in Table V.

VI.11 Alternative analysis

The 147 GeV deuterium data was analysed independently of the analysis described above. This second analysis had several distinct features; these differences are summarized in Table VI. The lack of a vertex cut in the second analysis led to a larger empty target subtraction, and hence a larger error on the final result than in the first analysis. The two analyses of the deuterium data were in good agreement, and gave confidence in the methods of the first analysis, the results of which are presented below for each of the data sets.

VII. Results

We have derived values for the structure function $F_2(Q^2, x) = \nu W_2(Q^2, x)$ over the complete kinematic range covered by the experiment. The value of $R(Q^2, x)$ has been measured over a more restricted region. These data can be used with Eq. 4 to evaluate the cross section at any desired point in the Q^2, x plane.

VII.1 Measurement of R for the proton

The relationship between the structure functions and R is shown in Eq 4 - 7. A large part of the data lie in regions inaccessible to lower-energy experiments, so that it is important to measure R over the range accessible to this experiment and use these values to extract the structure function. This experiment has data at three energies, which allows the determination of R in the region where two or three data sets overlap. This is equivalent to the separation of the structure functions F_1 and F_2.

Equation 4 shows that the cross section is not strongly dependent on R over much of the kinematic region covered by the experiments. This means, however, that small changes in the cross section induce large changes in R, and some care must be taken to ensure that the process of extracting R measures something other than the systematic differences between the experiments at the three energies. Insofar as the data at each energy were taken in the same apparatus and analysed using similar programs, these relative systematic effects should be small. They were measured by comparing the extracted values of F_2 at each energy in regions where its value is insensitive to R. The structure function should have the same value in a given Q^2, x) bin regardless of the energy of the incident muon. The values of the normalization factors applied to the data sets were allowed to vary, and the best normalization factors were found by

minimizing the χ^2 for the data set comparison. When this was done for some of the data with intermediate values of x ($0.02 < x < 0.09$), the normalization factors required of the 96 GeV and 147 GeV data were 1.01 ± 0.055 and 1.01 ± 0.045 relative to the 219 GeV data. That is, the best χ^2 is obtained by multiplying the three data sets by 1.01, 1.01, and 1.00. Calculations based on estimated systematic differences between the experiments (e.g. muons at the same physical position at the muon hodoscopes have different Q^2 and ν for the different energies) indicate that the normalizations should be less than a few percent.

In this experiment, the cross section in region $x > 0.1$ is quite insensitive to the value of R. In addition, muons having $x > 0.1$ were often close to the beam and the beam veto, and were therefore more subject to systematic effects than the lower x data; these data were not used to evaluate R.

An example of the stability of the results in the face of changing systematics is shown in Fig. 14, where the differing acceptances and radiative corrections at the three energies are shown in conjunction with the extracted structure function.

The standard approach to the evaluation of R involves plotting $\sigma = \sigma_T + \epsilon\sigma_L$ (Eq. 2) as a function of ϵ for a given kinematic bin. The different energies give different values of ϵ, and the straight-line fit yields σ_L and σ_T (Fig. 15). This approach is satisfyingly direct, but in this experiment it suffered from having to set up well-defined bins, in which there was often little data, or where the ϵ difference afforded by the muon energy range was small. Accordingly a procedure utilizing the full overlap region was devised to make maximum use of the statistical power available to the experiment. This took the form of a program identical to that used in measuring the

relative normalizations, except that in this case the value of R was varied. The kinematic variation of R is also of interest and fits including such variations were performed by varying the parameters of simple functional forms for R. Unfortunately, the precision of the data allows only consistency checks to be made.

The values of R obtained assuming R = constant for bands of x are shown in Table VII and in Fig. 16. The data are consistent with a constant value of R: $R = 0.52^{+0.17}_{-0.15}$. The fit has a χ^2 of 168.4 for 157 degrees of freedom. The errors quoted are statistical only. If the normalizations applied to the data are allowed to change by their measured errors, the resulting change in R is $^{+0.24}_{-0.20}$. Changes in R of a similar size can be induced by uncertainties in the positions of the hodoscope element edges affecting the acceptance, or in the trackfinding correction. These are shown in Table VIII. If all the errors noted are added in quadrature, along with a possible additional change of 0.15 estimated for the effects of the suicide correction, the estimated total error on R is $\Delta R = 0.35$.

One possible form for the variation of R is[29]: $R = R_o(1 - x)/Q^2$. Fitting this form to the data gives $R_o = 1.20^{+0.43}_{-0.36}$ GeV^2 for Q^2 in GeV^2. The χ^2 is 164.4 for 157 degrees of freedom. The error in the measured normalizations give rise to changes in R_o of $^{+0.57}_{-0.38}$. This suggests, using the relation between R and the quark transverse momentum noted earlier, $R = 4\langle p_T^2\rangle/Q^2$, that $\langle p_T^2\rangle(x) = 0.3(1 - x)$ GeV^2.

Another form, suggested by QCD[30, 13] is $R = R_o'(1 - x)/\ln(Q^2/\Lambda^2)$. The approximations used in deriving this form are valid only for $x \geq 0.1$, whereas the data used in the measurement had $x \leq 0.1$. Nonetheless, the form does fit the data as well as the two previously mentioned parametrizations; the

fit had a χ^2 of 172.8 for 157 degrees of freedom. Using Λ = 0.5 GeV, $R_o' = 1.18^{+0.39}_{-0.33}$. If the data are split into three Q^2 ranges, and the data available in each range are averaged over x, a different approach to the Q^2 variation is obtained. (Fig. 17) Note that the x range, while different for each point, is confined to $x < 0.1$. The average x increases with Q^2.

A simple parton model incorporating exact scaling of both structure functions predicts $R = Q^2/\nu^2$. The data are one and one-half standard deviations away from this picture because the large values of ν involved mean that the prediction is essentially zero, while the trend of the data is larger than zero.

The rise in the value of R at low x and low Q^2 measured in this experiment is not so significant as to invalidate a possible assumption that R = constant. However, such a rise is expected both by QCD[13] and by general arguments of a "hadronic photon" nature.[31] The rise appears very striking when the x range is separated into "very small x" ($x < 0.01$) for which $R = 1.22^{+0.37}_{-0.47}$ and "small x" ($0.01 < x < 0.1$) for which $R = 0.38^{+0.17}_{-0.15}$. The ranges of Q^2 and x over which there is enough data to measure R are correlated. We cannot therefore separate a Q^2 dependence and an x dependence.

Early analyses of electron scattering data from SLAC and MIT[6] also showed a statistically insignificant rise in the average value of R as x and Q^2 are decreased. The data here continue that trend. However, a further analysis of that data[32] shows that the data are also well fitted by a constant value for $x \geq 0.2$ of $R = 0.21 \pm 0.10$.

While these experiments cannot distinguish between various forms for R, they do indicate that R, at low x, is higher than either the earlier SLAC value of 0.14 ± 0.1[6] or the latest combined SLAC/MIT-SLAC value of 0.21 ± 0.10, measured at lower energies and higher values of x. Since our data at $x > 0.1$ are quite insensitive to the value of R, we have used the value $R = 0.52$ in extracting $F_2(Q^2, x)$ from the cross sections.

VII.2 $F_2(Q^2, \omega)$

The value of the structure function $F_2(Q^2, \omega)$ is presented in Table IX for each of the three muon energies incident on the hydrogen target, for the combined hydrogen data, and for the deuterium data. This data was evaluated in bins of ω and Q^2. The data table was prepared assuming $R = 0.52$ for both hydrogen and deuterium. Figure 18 shows the combined hydrogen data as a function of Q^2 for various bands of ω. The horizontal bars indicate the effects of changing R by its standard deviation, to 0.69 and 0.37. Some lower energy data[32, 33] are also shown in the figures.

It is intended that these values of $F_2(Q^2, \omega)$ be considered to be the correct experimental value for a point at the center of the bin. For ω large enough F_2 varies sufficiently smoothly that the value of F_2 averaged over the bin, which is what we measure, is almost the same as that at the center of the bin. However, for $\omega < 5$, F_2 varies considerably over a bin; moreover for the bins with ω near 1, there are apparatus cuts which do not correspond to the bin boundaries so that a correction is necessary and was made to make these bin centered values. For the largest ω bin for each Q^2, some parts of the bin are inaccessible kinematically. The values are values averaged only over the portion of the bin where data exists. Care should be exercised in using those values in Table IX in brackets where the bin center is not kinematically accessible. The number of events is small and corrections to other values of R are great. We have omitted these from our moment analysis. Fig. 19 shows the same data as a function of x in bands of Q^2. The value of x is $1/\omega$ where ω is the value at the center of the bin.

Several features of the data emerge on inspection of the figures.

1) The previously observed pattern of scaling violations is seen: the value of F_2 falls with increasing Q^2 at low ω and rises with increasing Q^2 at high ω. The turnover point is approximately at $\omega = 4$.

2) The value of R affects primarily the region $\omega > 10$, where it was measured. The changes can be quite noticeable at large ω or large Q^2. Referring to eq. 4 the square bracket can be approximated:

$$[\quad] = 2EE' + (Q^2 + \nu^2)/(1 + R)$$

When ω is large, ν is large and E' is small; the second term dominates the bracket, and changes in R can affect F_2 substantially. When ω is small, the reverse is true and R has little effect on the structure function.

3) The effect of increasing the assumed value of R is to increase the derived value of the structure function. The overall effect of the parametrization $R = R_0(1 - x)/Q^2$ is to flatten the structure function at high ω: since R is then falling rapidly with Q^2, there is less rise than when R is set to a constant. Also, the points at lower Q^2 have a larger R and are raised relative to R = constant.

4) There is substantial agreement between the values of F_2 found in this experiment and those from the SLAC and MIT-SLAC data as shown in the figures. A bin-by-bin comparison in the overlap region gives a χ^2 of 46.2 for 34 degrees of freedom. It is difficult, given the small size of the overlap region, to estimate any systematic differences, especially in the shape of F_2.

5) As Q^2 becomes small, so must F_2, since all real photons are transversely polarized. This behavior is seen in the high ω bins for $Q^2 \leq 1$ GeV^2.

6) The deuteron data in our range of x and Q^2 is indistinguishable from the hydrogen data (multiplied by 2) to within the errors.

VII.3 Scaling violations

While the existence of scaling violations is established, their interpretation is not so straightforward. When scaling violations were observed, attempts were made to recover complete scaling by expressing the data in terms of a new variable $\omega' = \omega + Q^2/M^2$ instead of ω. These attempts had initial success although violations of scaling in ω' have been observed at SLAC.[6] A new scaling variable should attempt to correct for the effect of quark binding of quark masses, and QCD specifies a variable $\xi = 2x/(1 + \sqrt{1+ 4M^2x^2/Q^2})$ when the masses of both the struck and the final quark are light; at large x, $\xi = 1/\omega'$, and $\xi \to x$ at large Q^2. For that part of our data and those of references 19 and 20, at small x (high ω) none of the standard scaling variables will restore scaling.

However, at small x (high ω) the limitation on beam energy and hence ν is reflected in a limitation to low values of Q^2. The fact that $F_2(x, Q^2)$ must fall to zero as Q^2 decreases necessarily implies that scaling is not a valid concept at low Q^2. The rise of $F_2(x, Q^2)$ with Q^2 is termed the "approach to scaling." There is no a priori way of defining this region, however, and some of the variation of F_2 with Q^2 at high ω, even for $Q^2 > 1$ GeV^2, may arise from this kinematic constraint. In Fig. 20, the data from several ω bins are plotted against Q^2. The line in the figure is the constraint on the very low Q^2 variation of F_2 provided by the real photon cross section. The data at finite Q^2 approach "scaling" more slowly than that, and no clear "edge" can be seen in the distributions. In order to be quantitative, some value for the low-Q^2 limit of the "scaling region" must be defined. Phenomologically, scaling in ω' was initially observed at SLAC, at least in certain regions of ω', for $Q^2 > 1$ GeV^2. The limit chosen here, then, is $Q^2 = 1$ GeV^2. Figure 20 suggests that this is not an unreasonable choice. Further discussion on this point will follow in the next subsection.

VII.4 Scaling violation fits to the hydrogen data

The violations of scaling may be investigated more quantitatively by fitting the data. The Q^2 dependence can be shown by fitting $F_2(Q^2, x)$ in bands of constant x to the form

$$F_2(Q^2) = F_2(Q_o^2)(Q^2/Q_o^2)^b \qquad Q_o^2 = 3 \text{ GeV}^2 \qquad (13)$$

Note that b is the value of $d[\ln F_2]/d[\ln Q^2]$; b = 0 corresponds to exact Bjorken scaling. Within the Q^2 range of the data, a fit can as easily be made with a term which is a power of $\ln Q^2$. The measured values of b are shown in Fig. 21. The fits used only data with $Q^2 > 1$ GeV^2. The effects of changes in R are again indicated in the figure by horizontal bars. The values of b obtained when R is assumed to be zero are shown in the figure as crosses when they differ significantly from the values obtained when R = 0.52. The error bars are similar in size in each case. If the Q^2 dependent value of R is assumed, the resulting scaling violations are approximately the same as those for R = 0; they are slightly smaller at very low x. This is still significantly different from b = 0, and it is important to note that no reasonable parametrization of R eliminates the scaling violations seen in the data.

It is not clear whether the rise of b at low x is real. The data are essentially flat in b when the parametrization $R = 1.20(1-x)/Q^2$ is used. The Q^2 range of the very low x bins is restricted and close to $Q^2 = 1$ GeV^2, and the "approach to scaling" effect may be inflating the violation measured in that region. An attempt was made to estimate the size of this "kinematic inflation" of b by increasing the lower Q^2 limit of the data allowed in the fits. No clear conclusion could be drawn from this process. The violation parameter b should decrease as the minimum Q^2 is increased, if kinematic inflation is

important. Some of the low x bins did show such a decrease, but others fluctuated, and others increased. It is possible, of course, that the value of Q^2 at which the "onset of scaling" takes place is an increasing function of ω, and that all of the high ω violation is of the kinematic variety. Only data at higher Q^2 can resolve this question.

VII.5 Low Q^2 data

For the muon-hydrogen scattering data at 219 Gev a special effort was made to remove the muon electron scattering events from the data. This was done by plotting the distribution of cross section versus Q^2 at various ν. On such a plot the muon-electron scattering cross section appeared as a distinct peak at the kinematic value $Q^2 = 2M_e\nu$. The data was fitted by a smooth line from each side of the bump.

Since F_2 goes to zero as Q^2 goes to zero we found it more convenient to plot the virtual photoproduction cross section $d\sigma/dQ^2 \equiv \sigma_T + \varepsilon\sigma_L$ as shown in fig. 22 for the limited range 319 $GeV^2 < W^2 <$ 375 GeV^2. We fit this curve with the form $\sigma(Q^2, \nu) = A(\nu)[1/(1 + Q^2/M_o^2)]$ for $Q^2_{min} < Q^2 < 0.4$ GeV^2/c and find $A = 132 \pm 13$ μb and $M_o^2 = 0.09 \pm 0.03$ GeV^2 ($\chi^2 = 11.3$ for 10 degrees of freedom). This value of A can be compared to the real photon cross section at the bin center $\sigma_\gamma(\nu = 184$ Gev$) = 118$ μb.[36] If we assume that in this range of ω that $\sigma_L/\sigma_T \equiv R = 0.52$ and drops sharply to zero at $Q^2 = 0$, then $\sigma_\gamma = \sigma_T(0, \nu)$ becomes 111 μb, in good agreement.

VII.6 Fits

A different approach to scaling and its violations involves fitting a global form, preferably one suggested by theory, to the data. The most desir-

able form would be a theoretically-derived function, valid for all Q^2 and x. Unfortunately, field theoretic approaches cannot predict the value of the structure function at all at low Q^2, and must make assumptions to predict it even at higher Q^2. Other theoretical approaches have other difficulties. Vector Dominance, for example, works well enough at low Q^2, but requires too many assumptions or parameters to be appealing in the "scaling region." Several different fits have been made, each with a different set of assumptions.

These fits include some of the lower energy SLAC and MIT-SLAC data.[33] In order to reduce computational complexity, some of the lower energy data points have been combined in somewhat larger bins, and points in the resonance region (W < 2 GeV) have been removed from the fits. All the points have had a 5% "systematic" error added in quadrature to the statistical error; this amount is consistent with the estimated systematic errors of all the experiments. The "full" data set includes the combined hydrogen data from this experiment, the SLAC data, and the MIT-SLAC data. In all cases a value of R = 0.14 was used to extract the structure function from the lower-energy cross-sections; either R = 0.52 or R = 1.20 $(1-x)/Q^2$ was used for the data from this experiment. The value of R used will identify which version of the full data set was used in a particular fit. Changes in R will affect the shape of the structure function at low x. The use of R = 0.14 for the lower energy data does not significantly affect the answers, since in the worst case the change in F_2 is only 6%, about the same size as the systematic effects.

The first approach starts from the scaling violation fits described above. The value of b(x) can be fit with a term logarithmic in (1-x), and a polynomial in (1-x) was used to fit $F_2(Q_o^2, x)$ giving as a global form

$$F_2(Q^2, x) = \left[\sum_{i=1}^{3} a_i(1-x)^i\right] \quad (Q^2/Q_o^2)^{\,C_1 + C_2 \ln(1-x)}$$

$$Q_o^2 = 3 \text{ GeV}^2 \qquad (14)$$

The full data with $Q^2 \geq 1$ GeV^2 were fit to the above form. The result is shown in Table X; the function is plotted in Fig. 23. The value of $C_1 + C_2 \ln(1-x) \equiv b(x)$ is also shown in Fig. 21.

Another approach rests on the development by Buras and Gaemers[37] of analytical forms for the quark and gluon distributions which reproduce the Q^2 variation of the moments predicted by QCD. The free parameters in their fit are the values of the moments of the distributions at a fixed Q_o^2, since the theory can predict the evolution in Q^2 given a starting point. They have fit their form to SLAC and early hydrogen data from this experiment. The agreement is reasonable at high x where their fit is dominated by the SLAC data. However, at low x, the fit is first too high, then too low, as x decreases. The increase with Q^2 tends to be too swift, also. At low x, the quark sea is beginning to dominate the scattering. The sea distributions increase in importance with Q^2, causing the rise of F_2 at low x. The shape of the sea distribution at an input value of $Q^2 = Q_o^2$ determines the amount of sea contribution to F_2 at Q_o^2 as well as the rate of increase. Buras and Gaemers find the initial quark momentum distributions proportional to $(1-x)^{10}$, but indicate that $(1-x)^5$ might serve almost as well. The discrepancies mentioned above, however, suggest that the distributions should be yet more concentrated towards $x = 0$.

The methods employed by Buras and Gaemers include fitting the Q^2 dependence of the first twelve moments of the valence quark distributions, and a re-

petition of their complete fit is beyond the scope of this paper. Several fits were made, allowing the parameters describing the sea quark and gluon distributions to vary, but keeping the valence terms fixed. The gluon distributions resulting from these fits were found to have an exponent consistent with those mentioned in Ref. 37, but the sea quark distribution was found to have a significantly larger exponent. However, the scarcity of data at low x and high Q^2 meant that the fits were not well determined.

The shape of the sea distributions can be deduced from other data, notably from lepton pair production by hadrons.[38] These experiments assume that the dominant source of direct lepton pairs is the Drell-Yan mechanism, and use existing knowledge of the proton structure function to extract the sea quark distributions. Those data[38] indicate that the exponent should lie in the range 8-10.

The previously described fits did not include the data at low Q^2, by design. By the same token, fits to the low Q^2, "approach to scaling" region usually do not

venture beyond Q^2 ~ 1-2 GeV^2, for similar reasons. Many approaches at both high and low Q^2 use, either implicitly or explicitly, the parton model or parton distribution functions to derive the value of F_2, suggesting that a properly designed form based on a parton model approach might accomodate both the scaling region and the approach to scaling.

Such an approach has been devised by Kirk.[39] Here,

$$F_2(Q^2, x) = P_3(2 + g_3)\, x\, (1 - x)^{1+g_3} + P_5 \frac{14}{9} \frac{4+g_5}{5+g_5} (1 - x)^{3+g_5} \frac{Q^2}{Q^2+m_o^2} \qquad (15)$$

where

$$g_3 = g_{03} + \varepsilon$$

$$g_5 = g_{05} + \varepsilon$$

$$\varepsilon = \kappa \ln[(Q^2 + m_o^2)/m_o^2]$$

and P_3, P_5, g_{03}, g_{05}, κ, and m_o are free parameters.

The model views the proton as having accessible to it a number of states with different numbers of quarks and gluons in each; there is an associated probability that the proton will be in that state when the muon scattering takes place. The terms in Eq. 15 represent the two simplest such configurations. The first term considers scattering from a state of three valence quarks and g_3 gluons. The partons (quarks plus gluons) are given a one dimensional phase space momentum distribution after Bjorken and Paschos.[40] The second term considers scattering from a state which has a quark-antiquark pair in the sea, and includes an explicit Q^2 dependence for the approach to scaling in the generalized vector dominance spirit, as developed by Devenish and Schildknecht.[41]

The form was fit to the full data set with $Q^2 \geq 0.3$ $(\text{Gev/c})^2$, and the results are shown in Table XI and Fig. 24. The fit with R = 0.52 had a χ^2 of 285 for 279 degrees of freedom.

Since the form includes explicit terms intended to fit the approach to scaling, the limit of the fit as Q^2 goes to zero is of interest. The fits in Table IX give σ_γ = 105 μbarn, and σ_γ = 121 μbarn, to be compared with σ_γ (E_γ = 200 GeV) = 118 μbarn.[36] Considering that the normalization of the second term is not completely reliable when $Q^2 \lesssim m_o^2$, an effect which tends to suppress the fit value of σ_γ, the agreement is quite satisfying.

VII.6 Moments of the Structure Functions

It is of particular interest to see to what extent the deviations from scaling, made evident in these experiments, correspond to the predictions of QCD. These predictions are given most directly in terms of the Q^2 behavior of the moments,[10-14]

$$I_i(n,Q^2) = \int_0^1 x^{n-2} F_i(x,Q^2)dx \qquad (16)$$

rather than the structure functions themselves. According to QCD the moments are given by a sum of terms which vary as negative powers of $\log(Q^2/\Lambda^2)$ as Q^2 becomes large. These powers are the anomalous dimensions given explicitly in the theory. While every field theory predicts scaling violations as $Q^2 \to \infty$, only QCD makes the prediction specific and subject to experimental verification.

The predictions are simplest for the flavor nonsinglet structure functions such as $F_2^{ep} - F_2^{en}$ in deep inelastic electron (and muon) scattering, or the vector-axial vector interference structure function xF_3 in charged current νN and $\bar{\nu}N$ scattering. In these cases the Q^2 behavior of each moment is given by a single term,

$$M_{NS}(n,Q^2) = M_{NS}(n,Q_0^2)e^{-\lambda_{NS}^{(n)}s} \qquad (17)$$

Here $M_{NS}(n,Q_0^2)$ is the value of the moment at some arbitrary value Q_0^2, $s = \ln[\ln(Q^2/\Lambda^2)/\ln(Q_0^2/\Lambda^2)]$ gives the Q^2 dependence in terms of a scale parameter Λ which must be determined from the data. The quantities $\lambda_{NS}^{(n)}$ are the "anomalous dimensions" of the theory, given by

$$\lambda_{NS}^{(n)} = \frac{4}{33 - 2f}\left[1 - \frac{2}{n(n+1)} + 4\sum_{j=2}^{n}\frac{1}{j}\right] , \qquad (18)$$

where f is the number of flavors.

The moments of the structure function F_2 are complicated by the presence of two additional singlet terms, S_+ and S_-. In this case QCD gives

$$M_2^{(N)}(n,Q^2) = M_{NS}^{(N)}(n,Q_o^2)e^{-\lambda_{NS}^{(n)}s} + M_+(n,Q_o^2)e^{-\lambda_+^{(n)}s} + M_-(n,Q_o^2)e^{-\lambda_+^{(n)}s} \qquad (19)$$

where N is either P for proton or N for neutron. QCD specifies the values of the $\lambda_i^{(n)}$. The coefficients $M_i(n,Q_o^2)$ are not calculated in the theory but have to be determined from the data. They may have negative as well as positive values. However, the observed moments $M_2^{(N)}(n,Q^2)$ are necessarily positive.

Expressions (17) and (19) are correct to leading order in the theory and can be expected to apply provided Q^2 is large enough. For values of Q^2 in the range covered by present experiments, higher order and target mass effects can be quite substantial. Nachtmann[42] has shown that by modifying the expression for the moments, the principal target mass effects can be accounted for. The Nachtmann moments for F_2 may be written

$$M_2(n,Q^2) = \int_0^{\xi_{max}} \xi^{n-2}[1 - (M^4/Q^4)\xi^4](1 + Q^2/\nu^2)(1 + 3n_n)F_2(\xi,Q^2)d\xi \qquad (20)$$

where M is the nucleon mass and

$$n_n = [(n + 1)M\nu\xi - (n + 2)Q^2]/[(n + 2)(n + 3)(\nu^2 + Q^2)]$$

$$\xi = [(\nu^2 + Q^2)^{1/2} - \nu]/M$$

$$\xi_{max} = \left[\frac{1}{2} + \left(\frac{1}{4} + M^2/Q^2\right)^{1/2}\right]^{-1}$$

In what follows we use the Nachtmann moments in applying Eq. (19) to our data. We carry out the analysis first to leading order and then to 2nd order in the coupling constant α_s. By restricting the analysis to the data with $Q^2 > 3$ GeV^2 these effects keep within manageable proportions.

The moments were calculated from the experimental data by numerical integration. To cover the full range of x adequately we combined our muon scattering data with the electron scattering data from the SLAC[33] and MIT-SLAC[33] experiments. Our muon data, which covers the region of small

x, complements nicely the rather extensive electron data over the rest of the range. This is seen in a sample plot of the combined data for $8 \leq Q^2 \leq 10$ GeV^2 in Fig. 25. The integrals were calculated from the data in several Q^2 bins. In each case their value from X_{min} to x_{max} was calculated by direct numerical integration of the data, where x_{min} (x_{max}) is the smallest (largest) value of x for which there is data. This procedure correctly includes the effects of the nucleon resonances since there is electron data right through the resonances. The contribution to the integral from 0 to x_{min} was estimated by assuming $F_2(x = 0) \equiv F_2(x_{min})$. The contribution from x_{max} to $x = 1$ was calculated by setting $F_2(x = 1) = 0$. Except for the highest Q^2 bin, $30 \leq Q \leq 50$ Gev^2, these corrections were generally quite small. The contribution to the integral from elastic scattering was included using the dipole formula for the elastic form factors, as given in Appendix 1.

The values of F_2 obtained from the measured cross sections depend on the choice of R. We used various values of R at various times. In the latest analysis reported here, we used the constant values, $R = 0.52 \pm 0.10$ for the muon data (Section VII.1) and $R = 0.21 \pm 0.10$ for the electron data[32]. The moments were calculated using bin centered values of F_2. The values of F_2 for the muon data given in Table IX are at the bin centered Q^2. To put the electron data on the same basis we adjusted each data point to the bin center using Eq. (13) in Sec. VII.4, with $b = 0.25 - x$, to give the Q^2 variation of F_2 within the bin. The effect on the moments of this adjustment was very small. For the muon data the values of F_2 listed in Table IX were used. However, we did not use the values shown in brackets because, as noted above, these lie outside the range of the cuts imposed on the value of ν.

The moments calculated in this manner are tabulated in Table 12. We give both the even and odd moments from $n = 2$ to $n = 10$. The errors stated include, besides the statistical errors associated with the measured values of F_2, errors of extrapolation, estimated as 25% of the amount of the extrapolation, an uncertainty of 10% of the amount of the elastic scattering contribution, and a 2.5% systematic error added in quadrature to take into account uncertainties in normalization. A further uncertainty is due to the lack of knowledge of R. This was included by calculating the moments using values of R greater or smaller by one standard deviation as given above. The error due to R was estimated as being 1/2 the difference obtained and

added in quadrature to the other errors. This contribution was generally the largest of all, amounting to 5% more or less depending on n and Q^2.

The deuteron moments are given per deuteron (not per nucleon) without correction for the Fermi motion. The elastic correction is included, obtained by summing the contribution of the neutron and the proton, taken as free.

The values used for the elastic scattering contribution are listed in Table A1 in the Appendix. The correction is particularly large for low Q^2 and high n. These values of the moments should be applied with caution.

VII.7 The Energy-Momentum Sum Rule

In parton theory the integral $I_2 = \int_0^1 F_2(Q^2,x)dx$ measures the fraction of the energy-momentum of the proton carried by the charged partons, weighted by their charge squared.

In the naive parton model the expected value for the proton, made of two "up" quarks and one "down" quark, is 0.333. For the neutron, made of one "up" quark and two "down" quarks, the expected value is 0.222. In QCD, in the large Q^2 limit, the integral has the value[12]

$$I_2 = \sum_i q_i^2/(3f + 2g),$$

where q_i is the charge on the i^{th} quark. The sum runs over all f flavors and three colors, and g = 8 is the number of gluons. For f = 4, I_2 = 0.119. The same for the neutron as for the proton, because in QCD, at high enough Q^2, the two are indistinguishable.

In Fig. 26 the second (Nachtmann) moments for the proton and the deuteron given in Table 12 are shown plotted as a function of Q^2. There is very little Q^2 dependence. The value for the proton, 0.18, is well below that cited for the naive parton model, implying that only 54% of the energy-momentum of the proton is carried by the charged quarks. In the light of QCD the missing energy momentum is carried by gluons and at the present values of Q^2 the quarks that are in evidence are mainly the valence quarks. In the case of the deuteron the value of the second moment is 0.30. The value for the neutron, obtained by difference is thus 0.12. Again, at our relatively low values of Q^2, the quarks in evidence in the neutron are mainly the valence quarks and these

carry 54% of the energy momentum. In both cases gluons carry the remainder, 47%.

These rough considerations are borne out by a more detailed analysis using QCD in leading order. Following the method used in Ref. (48) the moment coefficients are written in terms of the quark and gluon moments at $Q^2 = Q_0^2$. For up quarks,

$$\langle u\rangle_n = \int_0^1 x^{n-1} u(x,Q_0^2)dx \quad , \tag{21}$$

where $u(x,Q_0^2) = N_u(x,Q_0^2) + N_{\bar{u}}(x,Q_0^2)$, and similarly for the d and s quarks (we neglect the c quarks); for gluons $G(x,Q_0^2) = N_G(x,Q_0^2)$. Here, N_i is the number of quarks, antiquarks, or gluons per unit momentum interval, in units of the nucleon momentum. In terms of these moments the moment coefficients of Eq. (19) may be written

$$M_{NS}^P(n,Q_0^2) = \frac{1}{6}\left[\langle u\rangle_n - \langle d\rangle_n - \langle s\rangle_n\right] \tag{22}$$

$$M_{NS}^N(n,Q_0^2) = \frac{1}{6}\left[-\langle u\rangle_n + \langle d\rangle_n - \langle s\rangle_n\right] \tag{23}$$

$$M_+(n,Q_0^2) = \frac{5}{18}\left[a_n^-(\langle u\rangle_n + \langle d\rangle_n + \langle s\rangle_n) - \langle G\rangle_n\right]/(a_n^- - a_n^+) \tag{24}$$

$$M_-(n,Q_0^2) = \frac{5}{18}\left[a_n^+(\langle u\rangle_n + \langle d\rangle_n + \langle s\rangle_n) - \langle G\rangle_n\right]/(a_n^+ - a_n^-) \quad . \tag{25}$$

The constants a_n^+ and a_n^- are given in the theory by the formulas stated in Appendix 2. For $n = 2$, $a_2 = -18/5$, $a_2^- = 24/5$.

A fit to the data is found by choosing a value of Λ and then finding the values of the $\langle q_i\rangle$ and $\langle G\rangle$ by least squares. The value of Λ is then varied until the best overall fit is found. The moments $\langle q_i\rangle_2$ give directly the energy momentum carried by the quarks q_i. Energy-momentum conservation gives

$$\sum_i \langle q_i\rangle_2 + \langle G\rangle_2 = 1. \tag{26}$$

We used the second moments listed in Table 12, modifying the elastic scattering correction for the neutron by using a form factor 42% of its normal value to avoid some double counting in the data due to Fermi motion. Taking $Q_0^2 = 10$ GeV^2 we found $\langle u \rangle_2 = 0.34$, $\langle d \rangle_2 = 0.17$, $\langle s \rangle_2 = 0.06$ and $\langle G \rangle_2 = 0.43$. The solid curves of Fig. 26 show the fit obtained. The fit is rather insensitive to the value of Λ which turned out to be $\Lambda = 183 \pm 282$ MeV. A simultaneous fit of the $n = 2,4,6$ moments carried out in the manner of Ref. 48 is more restrictive and gave a common value of $\Lambda = 637 \pm 153$ MeV. This fit is shown as the dashed curve in Fig. 26. While these results seem plausible and in agreement with what had been obtained previously they make it clear that for a useful test of QCD it is important to study the higher moments.

VII.8 Higher Moments

In leading order QCD the Q^2 dependence of the n^{th} moment is given by Eq. (19). The value of Λ is the same for all n and is related to the coupling constant of the theory by the expression

$$\frac{\alpha_s(Q^2)}{\pi} \equiv \frac{\bar{g}^2(Q^2)}{4\pi^2} = \frac{4}{\beta_0 \, \ell n(Q^2/\Lambda^2)} \quad . \tag{27}$$

The inclusion of the next higher term leads to the expression[43-46]

$$\frac{\alpha_s(Q^2)}{\pi} = \frac{1}{\beta_0 \, \ell n(Q^2/\Lambda^2)} \left[1 - \frac{\beta_1}{\beta_0^2} \frac{\ell n \, \ell n(Q^2/\Lambda^2)}{\ell n(Q^2/\Lambda^2)}\right] \tag{28}$$

where

$$\beta_0 = 11 - \tfrac{2}{3}f$$

$$\beta_1 = 102 - \tfrac{38}{3}f$$

and f is the number of flavors.

The inclusion of the higher order corrections alters the relation between Λ and the coupling constant. Moreover, the additional terms in the Wilson operator expansion that must be included complicate the Q^2 dependence of the moments. If an analysis based on the leading order expressions is carried out apparent values of Λ will be obtained which will be different for each n. We denote these values by Λ_n. Such values of Λ_n may give a good fit to the data but are no longer simply related to the coupling constant.

To study this behavior we carried out an analysis of the higher moments based on Eq. (19) together with Eqs. (22-25). In the analysis for $n > 2$ we set $\langle s \rangle_n = 0$ to reduce the number of free parameters in the fit, since this quantity is known to be small in any case.

Table 13 lists the values of Λ_n obtained together with the values of the quark and gluon moments for each n up to $n = 10$. The values of Λ_n show a regular progression, increasing with n, as shown in Fig. 27. Good fits to the data are obtained as indicated by the small χ^2 values obtained for each n compared to the number of degrees of freedom, 14. The fits are shown in Fig. 28 for hydrogen and in Fig. 29 for deuterium. We show only the even moments. The increase in Λ_n from $n = 4$ to $n = 10$ amounts to 63%. However, the sensitivity of the fit to Λ_n is so poor that an acceptable fit with a constant Λ can also be obtained.

The evidence presented here is indicative of the presence of higher order QCD effects. This is in contrast with the neutrino data[47-50] for which such evidence is lacking.

In Bosetti, et. al.,[47] a quantitative verification of QCD is given based on the leading order expression:

$$\frac{d \log M_{NS}(n,Q^2)}{d \log M_{NS}(m,Q^2)} = \frac{\lambda_{NS}^{(n)}}{\lambda_{NS}^{(m)}} \quad . \tag{29}$$

The experimental values of the left-hand side of Eq. (29) are shown to agree remarkably well with the QCD value of the ratios $\lambda_{NS}^{(n)}/\lambda_{NS}^{(m)}$. A similar agreement has been obtained by de Groot, et al.[50] Such an agreement implies that $\Lambda_n = \Lambda_m$. However, if $\Lambda_n > \Lambda_m$, as our results indicate, the ratio of the slopes would be increased. With $\Lambda_4 = 0.59$ and $\Lambda_6 = 0.82$ as in Table 13 the expected value of the slope would be raised to 1.63.

The analysis given by Bosetti, et al.[47] is simplified by the use of the moments of xF_3 which are purely nonsinglet in character. In leading order QCD these have a simple exponential dependence on the variable s as given in Eq. (17).

In general, the moments of the structure function F_2 as given in Eq. (19) include a large singlet contribution. Contributions come from three terms with different exponential coefficients. However, the singlet contribution designated S_+ is relatively small while the exponential coefficients of the nonsinglet and the singlet S_- terms are closely the same for $n \geq 4$. Thus, the moments of F_2 for $n \geq 4$ can be expected to exhibit a simple exponential behavior with a slope approaching that of the NS term alone.

In Fig. 30 we display log M_6 versus log M_4. A least-squares fit to the points gave d log M_6/d log $M_4 = 1.62 \pm 0.19$, a value appreciably larger than the value 1.29 expected from leading order QCD but in good agreement with the expectation taking into account the change in Λ_n. This value of the slope is not changed much when the contribution of the S_+ term is removed.

We also display log M_{10} versus log M_6. The least-squares fit to the points gave d log M_{10}/d log M_6 = 1.60 ± 0.14 compared to the value 1.29 from lowest order QCD, again the larger slope can be accounted for by the increase in Λ_n, while the effect of the S_+ term is relatively small. In Table 14 we summarize the results for the slopes taking various combinations of even moments. The observed ratio of slopes is consistently greater than the lowest order QCD prediction, reflecting the monotonic rise of Λ_n with n.

VII.9 Second Order Corrections

Recently Floratos, Ross and Sachrajda[46] have calculated the second order corrections in the Wilson operator expansion. They included both the singlet and the non-singlet terms, making the corrections applicable to the structure function F_2. We carried out an analysis of the moments in the same way as for the leading order, but included the correction terms given in Ref. (46). We attempted to fit only the even moments listed in Table 12. As before, we reduced the neutron form factor to 42% of its normal value to avoid double counting of the data due to Fermi motion smearing in the elastic scattering.

We carried out the analysis setting $\langle s \rangle_n = 0$ except for n = 2. In Table (15) we give the best fit values of the quark and gluon moments obtained by allowing Λ_n to vary for each n separately. Good fits are obtained, with $\chi^2 < 7$ for 14 degrees of freedom. The main effect of including the second order corrections is to reduce the value of Λ by a factor of about 0.62.

Finally, we carried out the analysis after correcting for the effect of Fermi motion in deuterium. We used the formalism of Atwood and West[51] and

the Reid hard-core model for the deuteron.[52] The effect on the observed (inelastic part) of the deuteron moments is to increase the n = 2 moment by a factor 1.0158 and decrease the n = 4,6,8,10 moments by factors 0.9997, 0.9593, 0.8933, and 0.7989, respectively, without appreciable Q^2 dependence over our range of values. The results are given in Table 15. Figure 31 shows the variation of Λ_n with n.

A rising trend is indicated. This may imply that additional corrections, e.g. twist four, need to be included. On the other hand, these will mainly affect the higher moments, while most of the rise appears because Λ_n is so low. We have no ready explanation for this low value other than it occurs with a large error. We can make a global fit to the data using all even moments from n = 2 to n = 10 and obtain a good fit with a common value $\Lambda = 459 \pm 111$ MeV. The results of the analysis are given in Table 16. The χ^2 for n = 2 has now become 10.3, but this is still a good fit since there are effectively 15 degrees of freedom in this case. Accordingly, we take this value of Λ as the best value from our data. The overall fit to the data is shown in Figure 32. Inserting this value in Eq. (28) we obtain for the coupling constant $\alpha_s/\pi = .033 \pm .006$ at $Q^2 = 3$ GeV^2.

This value of the coupling constant is sufficiently small compared to 1 to suggest that further higher order corrections will be small. The general accord of the data to the behavior prescribed by QCD constitutes a strong statement of the essential correctness of this theory.

VIII. Conclusions

1. We have measured the value of $R = \sigma_L/\sigma_T$ in a previously inaccessible region. The data are not sufficiently precise to prescribe any kinematic variation, but are consistent with several forms, including $R = 0.52^{+0.17}_{-0.15}$; $R = R_o(1-x)/Q^2$, $R_o = 1.20^{+0.43}_{-0.36}$ GeV^2; $R = R'_o(1-x)/\ln(Q^2/\Lambda^2)$, $R'_o = 1.18^{+0.39}_{-0.33}$, $\Lambda = 0.5$ GeV. The last is suggested by QCD, although the approximations used to derive the form begin to fail in the region where the measurement was made. This result is therefore illustrative but not a test of the theory.

2. Using the first value of R derived above, we extracted the structure function $F_2(Q^2, x)$. Violations of Bjorken scaling in this function are clearly established by the data. The exact form of the violation at low x depends on the value of R, and on as yet unconstrained kinematic effects of the approach to scaling. The violations, however, cannot be removed by any reasonable choice of values for R, and as such, the data support the scaling violation prediction of QCD.

3. The value of F_2 can be fit to forms suggested by QCD. In one case, we use specific analytical forms for the quark distributions; in another, empirical forms are devised to fit the data. These fits do tolerably well, but the details are dependent on the shape of F_2, which is in turn strongly dependent on R, and the last is not well determined at low x.

The data can also be fit with a model which incorporates scale-violating terms into a simple parton model, and which fits both the "approach to scaling" and the "scaling" regions well.

4. The Callan-Gross sum rule integral I_2 shows, when evaluated using data extracted with R = 0.52, a slow decrease with Q^2, as expected by QCD.

5. An analysis of the even Nachtmann moments to 2nd order in α from $n = 2$ to $n = 10$ finds excellent agreement with the predictions of QCD. The gluons carry about 47% of the total energy-momentum and have a momentum distribution like that of the valence quarks. Only a small fraction of the energy-momentum distribution is concentrated at small x. We find $\Lambda = 0.46 \pm 0.11$ GeV, corresponding to a coupling constant $\alpha_s(Q^2 = 3\ \text{GeV}^2)/\pi = 0.033 \pm 0.006$.

IX. Acknowledgements

Many people, beyond the authors of the paper, made essential contributions to this experiment. At the Enrico Fermi Institute, R. Gabriel, T. Nunamaker, R. Norton, K. Burns, B. Grumman, and D. Turner fabricated and maintained the beam and 1m x 1m MWPC and shift-register chambers; W. Nakagawa and F. Quinn maintained the Σ-7 computer; J. Hansley made significant contributions to the on-line software. At Harvard, E. Sadowski designed the large 2 x 6 meter chambers, H. Weedon designed the high voltage pulsers for these chambers and R. Burns, R. Haggerty and J. O'Kane played a major role in constructing this chamber system. D. Rolinski who typed an innumerable number of drafts of this paper, deserves special thanks. At Oxford, P. Burton mounted the hodoscopes and was an enthusiastic helper in any arduous task that came to hand, while Leslie Jones and John MacAllister solved many computing problems with great efficiency. E.W.G. Wallis and his staff at the Rutherford Laboratory were responsible for the construction of the hodoscopes and the magnet-measuring apparatus. We thank all these invaluable people as well as many others in the Neutrino Department who made the experiment possible.

This research was supported by the National Science Foundation under contracts PHY-71-02186-A05, MPS 71-03-186, and PHY-76-23478, by the U.S. Department of Energy under contracts No. EY-76-C-02-3064 and No. E(11-1)-1195, and by the Science Research Council (United Kingdom).

APPENDIX I

The elastic structure function in terms of the Sachs' form factor is

$$W_2^{el}(Q^2,\nu) = \frac{G_E^2(Q^2) + \frac{Q^2}{4M^2} G_M^2(Q^2)}{1 + \frac{Q^2}{4M^2}} \delta(\frac{Q^2}{2M} - \nu) \quad .$$

where M is the nucleon mass.

To obtain the elastic contribution, substitute into the formula for the Nachtmann moments and change the variable from ν to ξ in the δ function and integrate. The result is, for the nth moment, an elastic contribution of

$$\frac{Q^2}{2M^2}[1 - (1 + 4M^2/Q^2)^{-1/2}](1 - \frac{M^4}{Q^4}\xi_{max}^4)(1 + \frac{4M^2}{Q^2})\xi_{max}^{n-2}(1 + 3\eta_n) \frac{G_E^2(Q^2) + \frac{Q^2}{4M^2} G_M^2(Q^2)}{1 + \frac{Q^2}{4M^2}} \quad ,$$

where

$$\eta_n = \frac{(n + 1)\xi_{max}/2 - (n + 2)}{(n + 2)(n + 3)(1 + \frac{Q^2}{4M^2})} \quad ,$$

$$\xi_{max} = 2/(1 + (1 + 4M^2/Q^2)^{1/2}) \quad .$$

We use the simple scaling law

$$G_E^p(Q^2) = \frac{G_M^p(Q^2)}{\mu_p} = \frac{G_M^N(Q^2)}{\mu_N} = G(Q^2) \quad ,$$

$$G_E^N(Q^2) = 0 \quad ,$$

A-1

and the empirical dipole formula

$$G(Q^2) = \left(1 + \frac{Q^2}{M_v^2}\right)^{-2} \quad \text{with } M_v = 0.84 \text{ GeV}.$$

APPENDIX 2

The constants a_n^+ and a_n^- are given by[48] [We use Nachtmann's formulation]

$$a_n^+ = \frac{36}{5} \frac{d_{G\psi}^n}{d_{\psi\psi}^n - \lambda_-^n}$$

$$a_n^- = \frac{36}{5} \frac{d_{G\psi}^n}{d_{\psi\psi}^n - \lambda_+^n}$$

where

$$d_{\psi\psi}^n = \frac{4}{33 - 2f}\left[1 - \frac{2}{n(n+1)} + 4\sum_{j=2}^{n}\frac{1}{j}\right]$$

$$d_{G\psi}^n = -\frac{4}{33 - 2f}\,\frac{n^2 + n + 2}{n(n^2 - 1)}$$

$$d_{\psi G}^n = -\frac{12f}{33 - 2f}\,\frac{n^2 + n + 2}{n(n+1)(n+2)}$$

$$d_{GG}^n = \frac{9}{33 - 2f}\left[\frac{1}{3} + \frac{2f}{9} - \frac{4}{n(n-1)} - \frac{4}{(n+1)(n+2)} + 4\sum_{j=2}^{n}\frac{1}{j}\right]$$

$$\lambda_\pm^n = \frac{1}{2}(d_{\psi\psi}^n + d_{GG}^n) \pm \frac{1}{2}\left((d_{\psi\psi}^n - d_{GG}^n)^2 + 4d_{G\psi}^n d_{\psi G}^n\right)^{1/2}$$

REFERENCES

1. I. Kostoulas, A. Entenberg, H. Jostlein, A.C. Melissinos, L.M. Lederman, P. Limon, M. May, P. Rapp, H. Gittleson, T. Kirk, M. Murtagh, M.J. Tannenbaum, J. Sculli, T. White, T. Yamanouchi, Phys. Rev. Lett. 32, 489 (1974).

2. A. Entenberg, H. Jostlein, I. Kostoulas, A.C. Melissinos, L.M. Lederman, P. Limon, M. May, P. Rapp, H. Gittleson, T. Kirk, M. Murtagh, M.J. Tannenbaum, J. Sculli, T. White, T. Yamanouchi, Phys. Rev. Lett. 32, 486 (1974).

3. J. Friedman and H. Kendall, Ann. Rev. Nuc. Sci. 22, 203 (1972).

4. J.D. Bjorken, Phys. Rev. 179, 1547 (1969).

5. J.D. Bjorken, Phys. Rev. Lett. 16, 408 (1966).

6. R.E. Taylor, Proceedings of the 1975 International Symposium on Lepton and Photon Interactions at High Energies, W.T. Kirk, ed., Stanford University, Stanford, California (1975), p. 679.

7. R.P. Feynman, Photon-Hadron Interactions, W.A. Benjamin, Inc., Reading, Mass. (1972).

8. K. Wilson, Phys. Rev. 179, 1499 (1969).

9. K. Wilson, Phys. Rev. D3, 1818 (1971).

10. H.D. Politzer, Phys. Rev. Lett. 30, 1346 (1973).

11. D. Gross and F. Wilczek, Phys. Rev. Lett. 30, 1343 (1973); Phys. Rev. D8, 3633 (1973); Phys. Rev. D9, 980 (1974).

12. H.D. Politzer, Physics Reports 14C, 129 (1974) and references contained therein.

13. A. de Rujula, Howard Georgi, and H. David Politzer, Ann. Phys. 103, 315 (1977).

14. H.D. Politzer, Phys. Lett. 70B, 430 (1977), and Nucl. Phys. B129, 301 (1977).

15. I. Hinchliffe and C.H. Llewellyn-Smith, Phys. Lett. 66B, 281 (1977).

16. R.P. Feynman, R.D. Field, and G.C. Fox, California Institute of Technology preprint CALT-68-651 (1978).

17. D.H. Perkins, P. Schreiner, and W.G. Scott, Phys. Lett. 67B, 347 (1977).

18. I. Hinchliffe and C.H. Llewellyn Smith, Phys. Lett. 70B, 247 (1977).

19. Y. Watenabe, L.N. Hand, S. Herb, A. Russell, C. Chang, K.W. Chen, D.J. Fox, A. Kotlewski, P.F. Kunz, S.C. Loken, M. Strovink, W. Vernon, Phys. Rev. Lett. 35, 898 (1975).

20. C. Chang, K.W. Chen, D.J. Fox, A. Kotlewski, P.F. Kunz, L.N. Hand, S. Herb, A. Russell, Y. Watenabe, S.C. Loken, M. Strovink, W. Vernon, Phys. Rev. Lett. 35, 901 (1975).

21. H.L. Anderson, V.K. Bharadwaj, N.E. Booth, R.M. Fine, W.R. Francis, B.A. Gordon, R.H. Heisterberg, R.G. Hicks, T.B.W. Kirk, G.I. Kirkbridge, W.A. Loomis, H.S. Matis, L.W. Mo, L.C. Myrianthopoulos, F.M. Pipkin, S.H. Pordes, T.W. Quirk, W.D. Shambroom, A. Skuja, L.J. Verhey, W.S.C. Williams, Richard Wilson, S.C. Wright, Phys. Rev. Lett. 37, 4 (1976).

22. H.L. Anderson, V.K. Bharadwaj, N.E. Booth, R.M. Fine, W.R. Francis, B.A. Gordon, R.H. Heisterberg, R.G. Hicks, T.B.W. Kirk, G.I. Kirkbridge, W.A. Loomis, H.S. Matis, L.W. Mo, L.C. Myrianthopoulos, F.M. Pipkin, S.H. Pordes, T.W. Quirk, W.D. Shambroom, A. Skuja, M.A. Staton, L.J. Verhey, W.S.C. Williams, Richard Wilson, S.C. Wright, Phys. Rev. Lett. 38, 1450 (1977).

23. B.A. Gordon, T.W. Quirk, H.L. Anderson, N.E. Booth, W.R. Francis, R.G. Hicks, W.W. Kinnison, T.B.W. Kirk, W.A. Loomis, H.S. Matis, L.W. Mo, L.C. Myrianthopoulos, F.M. Pipkin, J. Proudfoot, A.L. Sessoms, W.D. Shambroom, A. Skuja, M.A. Staton, C. Tao, W.S.C. Williams, Richard Wilson, S.C. Wright, Phys. Rev. Lett. 41, 615 (1978).

24. H.D. Politzer, Harvard Preprint HUTP-77/A038 (1977).

25. T.A. Nunamaker and D.B. Turner, Nucl. Inst. and Meth. 113, 445 (1973).

26. Y.S. Tsai, Proc. Nuc. Structure Conf., Stanford, California (1963).

27. L.W. Mo and Y.S. Tsai, Rev. Mod. Phys. 41, 205 (1969).

28. E. M. Riordan, et al., "Extraction of Structure Functions and $R = \sigma_-/\sigma_+$ from Deep Inelastic e-p and e-d Cross Sections," SLAC-PUB 1634 (1975).

29. R. P. Feynman, private communication.

30. L. N. Hand, Proc. of 1977 International Symposium on Lepton and Photon Interactions at High Energies, F. Gutbrod, ed., (1977).

31. T. H. Bauer, R. D. Spital, D. R. Yennie, and F. M. Pipkin, Rev. Mod. Phys. 50, 261 (1978).

32. R. E. Taylor, 19th International Conference on High Energy Physics, Tokyo, Japan (1978). M. D. Mestayer, "A Measurement of the Proton Structure Functions Using Inelastic Electron Scattering," SLAC-214 Thesis (1978).

33. R. E. Taylor, W. B. Atwood, and M. D. Mestayer kindly made available a complete set of the electron-scattering results from the SLAC and MIT-SLAC experiments: SLAC E4B, G. Miller, "Inelastic Electron Scattering at Large Angles," SLAC-129 Thesis (1971); SLAC E49A, J. S. Poucher, et al. Phys. Rev. Lett. 32, 118 (1974) and "High Energy Single Arm Inelastic e-p and e-d Scattering at 6° and 10°," SLAC-1309 (1973); SLAC E49B, A. Bodek, "Inelastic Electron-Deuteron Scattering and the Structure of the Neutron," Technical Report 93, MIT Thesis (1972); SLAC E87, E. M. Riordan, Ref. 28 and private communication (1976); SLAC E89-1, W. B. Atwood, et al., Phys. Lett. 64B, 479 (1976); W. B. Atwood, "Electron Scattering of Hydrogen and Deuterium at 50° and 60°," SLAC-185 Thesis (1978); SLAC E89-2, see Ref. 32.

34. H. Georgi and H. D. Politzer, Phys. Rev. Lett. 36, 1281 (1976).

35. W. Chen, Michigan State preprint MSU-CSL-51 (1977).

36. D. O. Caldwell, et al., XIX International Conference on High Energy Physics, Tokyo, Japan, 1978, Contribution 647.

37. A. J. Buras and K. J. F. Gaemers. Nuc. Phys. B132, 249 (1978).

38. D. M. Kaplan, R. J. Fisk, A. S. Ito, H. Jöstlein, J. A. Appel, B. C. Brown, C. N. Brown, W. R. Innes, R. D. Kephart, K. Ueno, T. Yamanouchi, S. W. Herb, D. C. Hom, L. M. Lederman, J. C. Sens, H. D. Snyder, J. K. Yoh, Phys. Rev. Lett. 40, 435 (1978).

39. T. B. W. Kirk, Fermilab Report No. TM-791, 1978 (unpublished).

40. J. D. Bjorken and E. A. Paschos, Phys. Rev. 185, 1975 (1968).

41. R. Devenish and D. Schildknecht, Phys. Rev. D14, 93 (1976).

42. W. A. Bardeen, A. J. Buras, D. W. Duke and T. Muta, Phys. Rev. D18, 3998 (1978).

43. G. Altarelli, R. K. Ellis and G. Martinelli, Nucl. Phys. B143, 521 (1978).

44. E. G. Floratos, D. A. Ross, C. T. Sachrajda, Nucl. Phys. B129, 66 (1977) and CERN report TH 2566-CERN (1978) and Phys. Lett. 80B, 269 (1979).

45. E. G. Floratos, D. A. Ross, C. T. Sachrajda, Phys. Lett. 80B, 269 (1979).

46. P. C. Bosetti, et al., Nucl. Phys. B142, 1 (1978).

47. H. L. Anderson, H. S. Matis, and L. C. Myrianthopoulos, Phys. Rev. Lett. 40, 1061 (1976).

48. H. L. Anderson, L. C. Myrianthopoulos, and H. S. Matis, Los Alamos preprint LA-UR 78-1891 (1978) and presented at the XIX International Conference on High Energy Physics, Tokyo, Japan, 1978.

49. J. deGroot et al., "Comparison of Moments of Valence Structure Function with QCD," CERN preprint (Nov. 1978).

50. W. B. Atwood and G. B. West, Phys. Rev. D7, 733 (1973).

51. R. V. Reid, Jr., Ann. Phys. (N.Y.) 50, 411 (1968).

TABLE I. Kinematic Variables

Masses

m_e	electron
m_μ	muon
M	nucleon

Four Vectors

$p_\alpha = (E, \underline{p})$	incident muon
$p'_\alpha = (E', \underline{p}')$	scattered muon
$P_\alpha = (M, 0)$	target nucleon
$q_\alpha = (\nu, \underline{q})$	virtual photon
$q_\alpha = p_\alpha - p'_\alpha$	

$\nu = E - E'$

$\underline{q} = \underline{p} - \underline{p}'$

$p = |\underline{p}|$

$p' = |\underline{p}'|$

θ = angle between $\underline{p}$ and $\underline{p}'$

$Q^2 \equiv -q_\alpha q^\alpha = 4EE' \sin^2(\theta/2) + m_\mu \nu^2/EE' + O(m_\mu^3/E^3)$

$Q^2_{min} \equiv 2(EE' - pp' - m_\mu^2)$

scaling variables

$\omega \equiv 2M\nu/Q^2$

$x \equiv 1/\omega$

$\omega' = \omega + M^2/Q^2$

$\xi = 2x/(1 + \sqrt{1 + 4M^2x^2/Q^2}) = (\sqrt{\nu^2 + Q^2} - \nu)/M$

other quantities

$W^2 = 2M\nu + M^2 - Q^2$ the square of the center of mass energy of the photon-nucleon system

$\Gamma = \frac{\alpha}{2\pi} \frac{K}{Q^2} \frac{1}{p^2} \frac{1}{1-\epsilon}$ flux of transverse photons

$K = \nu - Q^2/2M$ energy of a real photon, which, incident on a stationary target proton, gives center of mass energy W

$$\epsilon = \left[1 + \frac{2(Q^2 + \nu^2) \tan^2(\theta/2)}{Q^2(1 - Q^2_{min}/Q^2)^2} \right]^{-1}$$ ratio of longitudinal to transverse photon flux

TABLE II. Incident Beam Flux and Analysed Event Statistics

Data Set	Total Incident Beam	Analysed Events $Q^2 > 0.2$ GeV^2	Analysed Events $Q^2 > 1$ GeV^2
Run 1 147 GeV Deuterium	2.04×10^{10}	1.19×10^4	7312
Run 2 96 GeV Hydrogen	2.46×10^{10}	1.50×10^4	6533
Run 3 147 GeV Hydrogen	2.37×10^{10}	0.67×10^4	3059
Run 4 147 GeV Hydrogen	2.66×10^{10}	1.09×10^4	6767
Run 5 219 GeV Hydrogen	7.44×10^{10}	3.61×10^4	19883

Incident Energy (GeV)	Target	ϵ_1	ϵ_2	ϵ_3	ϵ_4	ϵ_5	ϵ_6	ϵ
96	H_2	68.5± 0.7	100	99.5 ± 0.5	99.2 ± 0.5	99.9 ± 0.1	97.7	65.9 ± 0.9
147	H_2	72.7± 0.6	99.0 ± 0.5	99.5 ± 0.5	98.7 ± 0.1	99.9 ± 0.1	97.7	69.6 ± 0.8
219	H_2	61.6± 0.6†	100	99.5 ± 0.5	93.7 ± 0.4*	99.9 ± 0.1	97.7	56.1 ± 0.8
147	D_2	76.0± 0.1	99.3 ± 0.03	99.5 ± 0.5	98.6 ± 0.1	99.9 ± 0.1	98.5 ± 0.1	72.9 ± 0.8

Table III. The kinematic independent efficiencies for various data sets. The efficiencies are: ϵ_1 = beam reconstruction, ϵ_2 = two incident muon, ϵ_3 = downstream spark chambers, ϵ_4 = upstream MWP chambers, ϵ_5 = counter. ϵ_6 corrects for neglect of vapor in target empty runs. $\epsilon = \epsilon_1 \epsilon_2 \epsilon_3 \epsilon_4 \epsilon_5 \epsilon_6$.

*include x-link efficiency
†includes cuts to remove beam tails

TABLE IV. Calculated Radiative Tail Fraction at 219 GeV in Parts Per Thousand: $1000 \times N_{ert}(\Delta Q^2, \Delta\omega) / W_{sum}(\Delta Q^2, \Delta\omega)$ (see equation (9))

E SCAT																					
50.00-80.00	0	1	4	83	28	0	0	0	0	0	0	0	0	0	0	0	0	0	0	0	0
30.00-50.00	0	0	1	3	5	18	83	160	0	0	0	0	0	0	0	0	0	0	0	0	0
15.00-30.00	0	0	0	0	1	3	7	16	49	64	0	0	0	0	0	0	0	0	0	0	0
10.00-15.00	0	0	0	0	0	1	2	3	8	47	221	0	0	0	0	0	0	0	0	0	0
8.00-10.00	0	0	0	0	0	0	1	1	4	23	91	0	0	0	0	0	0	0	0	0	0
7.00- 8.00	0	0	0	0	0	0	1	1	2	12	85	131	0	0	0	0	0	0	0	0	0
6.00- 7.00	0	0	0	0	0	0	0	1	2	6	26	97	245	0	0	0	0	0	0	0	0
5.00- 6.00	0	0	0	0	0	0	0	1	1	4	16	46	129	0	0	0	0	0	0	0	0
4.00- 5.00	0	0	1	0	0	0	0	0	1	3	9	22	87	163	0	0	0	0	0	0	0
3.50- 4.00	0	0	0	1	0	0	0	1	1	2	6	15	36	145	0	0	0	0	0	0	0
3.00- 3.50	0	0	0	0	0	0	0	1	1	2	5	9	25	115	275	0	0	0	0	0	0
2.75- 3.00	0	0	0	0	1	0	0	0	1	2	3	6	18	69	228	0	0	0	0	0	0
2.50- 2.75	0	0	0	0	0	1	1	1	1	1	4	6	13	44	183	0	0	0	0	0	0
2.25- 2.50	0	0	0	0	0	1	1	1	1	1	3	5	12	32	148	391	0	0	0	0	0
2.00- 2.25	0	0	0	0	0	1	1	1	1	1	3	7	10	25	93	228	0	0	0	0	0
1.75- 2.00	0	0	0	0	0	0	0	0	0	0	0	0	0	178	69	169	0	0	0	0	0
1.50- 1.75	0	0	0	0	0	0	0	0	0	0	0	0	0	0	41	143	447	0	0	0	0
1.25- 1.50	0	0	0	0	0	0	0	0	0	0	0	0	0	0	81	82	216	0	0	0	0
1.00- 1.25	0	0	0	0	0	0	0	0	0	0	0	0	0	0	0	42	173	0	0	0	0
.90- 1.00	0	0	0	0	0	0	0	0	0	0	0	0	0	0	0	0	194	290	0	0	0
.80- .90	0	0	0	0	0	0	0	0	0	0	0	0	0	0	0	0	109	295	0	0	0
.70- .80	0	0	0	0	0	0	0	0	0	0	0	0	0	0	0	0	102	328	0	0	0
.60- .70	0	0	0	0	0	0	0	0	0	0	0	0	0	0	0	0	0	301	438	0	0
.50- .60	0	0	0	0	0	0	0	0	0	0	0	0	0	0	0	0	0	215	338	0	0
.40- .50	0	0	0	0	0	0	0	0	0	0	0	0	0	0	0	0	0	0	385	0	0
.30- .40	0	0	0	0	0	0	0	0	0	0	0	0	0	0	0	0	0	0	368	381	0
.20- .30	0	0	0	0	0	0	0	0	0	0	0	0	0	0	0	0	0	0	0	311	0
DELTA	1.	2.	3.	4.	5.	7.	9.	11.	14.	20.	30.	45.	60.	80.	120.	160.	240.	400.	600.	1000.	1400.

TABLE V. Radiative Corrections at 219 GeV for Inelastic Region Calculated From Data Fit Ratio of True/ (Measured-Elastic Radiative Tail)

Q SQRD															
47.50	.000	.000	.000	.000	.000	1.141	1.085	1.038	1.011	.992	.975	.960	.943	.917	.855	.749
42.50	.000	.000	.000	.000	1.164	1.115	1.072	1.030	1.005	.986	.971	.956	.938	.912	.846	.739
37.50	.000	.000	.000	.000	1.127	1.095	1.060	1.022	.959	.981	.966	.951	.933	.906	.838	.728
32.50	.000	.000	.000	.000	1.103	1.079	1.049	1.014	.952	.975	.960	.946	.928	.900	.828	.716
27.50	.000	.000	.000	1.140	1.083	1.063	1.037	1.006	.985	.969	.954	.940	.922	.892	.816	.703
22.50	.000	.000	1.198	1.106	1.065	1.048	1.026	.957	.978	.962	.948	.933	.915	.883	.804	.689
17.50	.000	.000	1.121	1.079	1.047	1.033	1.013	.987	.969	.954	.941	.926	.907	.872	.790	.674
12.50	.000	1.160	1.083	1.054	1.028	1.017	.999	.976	.959	.945	.932	.916	.895	.860	.774	.662
9.75	.000	1.114	1.064	1.039	1.017	1.007	.991	.969	.953	.939	.926	.910	.888	.851	.764	.657
9.25	.000	1.108	1.060	1.037	1.015	1.005	.989	.967	.951	.938	.924	.908	.887	.850	.763	.657
8.75	.000	1.102	1.057	1.034	1.013	1.002	.987	.966	.950	.936	.923	.907	.885	.848	.761	.657
8.25	.000	1.096	1.053	1.031	1.010	1.000	.985	.964	.949	.935	.921	.906	.884	.846	.760	.656
7.75	.000	1.090	1.049	1.028	1.008	.998	.983	.963	.947	.934	.920	.904	.882	.844	.758	.656
7.25	.000	1.084	1.046	1.025	1.005	.996	.981	.961	.946	.932	.919	.903	.881	.843	.757	.657
6.75	.000	1.079	1.042	1.022	1.003	.994	.979	.959	.944	.931	.917	.901	.879	.841	.756	.657
6.25	.000	1.073	1.038	1.019	1.000	.991	.977	.957	.942	.929	.916	.900	.877	.839	.755	.659
5.75	.000	1.067	1.034	1.016	.998	.989	.975	.955	.940	.928	.914	.898	.875	.837	.754	.661
5.25	.000	1.061	1.030	1.012	.995	.986	.972	.953	.938	.926	.912	.896	.874	.835	.753	.663
4.75	.000	1.054	1.025	1.008	.991	.983	.970	.951	.937	.924	.910	.894	.872	.834	.753	.667
4.25	1.108	1.048	1.021	1.004	.988	.980	.967	.949	.934	.922	.909	.892	.870	.832	.753	.671
3.75	1.124	1.042	1.016	1.000	.984	.976	.964	.946	.932	.921	.907	.891	.868	.831	.754	.678
3.25	1.115	1.035	1.010	.995	.980	.973	.960	.943	.930	.918	.905	.889	.866	.830	.756	.685
2.75	1.104	1.028	1.002	.988	.974	.966	.955	.938	.928	.913	.900	.885	.863	.828	.759	.695
2.25	1.069	1.017	.996	.983	.969	.962	.951	.935	.922	.911	.898	.883	.862	.828	.764	.708
1.75	1.061	1.009	.983	.976	.963	.956	.946	.931	.919	.910	.896	.882	.861	.830	.774	.725
1.25	1.044	.998	.980	.968	.958	.951	.941	.927	.916	.909	.895	.881	.868	.835	.789	.747
.95	1.033	.991	.974	.963	.955	.947	.938	.925	.914	.908	.898	.882	.865	.841	.802	.762
.85	1.028	.988	.972	.961	.952	.945	.937	.924	.914	.905	.895	.883	.867	.845	.809	.770
.75	1.023	.985	.969	.959	.951	.944	.936	.924	.914	.905	.896	.884	.870	.848	.816	.776
.65	1.019	.982	.967	.957	.948	.943	.935	.923	.914	.906	.897	.890	.873	.855	.824	.782
.55	1.013	.979	.964	.956	.948	.942	.934	.923	.917	.907	.898	.889	.877	.861	.832	.785
.45	1.007	.975	.962	.954	.945	.941	.934	.924	.916	.908	.901	.892	.882	.867	.839	.780
.35	1.001	.972	.960	.952	.944	.940	.934	.925	.932	.911	.904	.897	.887	.874	.844	.750
.25	.994	.969	.958	.951	.945	.941	.936	.928	.921	.915	.909	.902	.894	.881	.840	.693
.15	.983	.967	.958	.953	.948	.945	.941	.934	.929	.923	.917	.910	.900	.881	.769	.000
NU	2.5	7.5	12.5	17.5	25.0	35.0	45.0	60.0	80.0	100.0	120.0	140.0	160.0	180.0	200.0	210.0

TABLE VI. Comparison of Analyses

Task	First Analysis	Second Analysis
Trackfinding starting point	6 m magnetostrictive chambers	all 20 planes
Trackfinding algorithm	spark chambers give initial track	spark pairs provide road for search
Muon identification	track linked or counter labelled	counter identification and presence of sparks in multiple scattering cone
Upstream-downstream linking	x or y link	x and y link
Vertex cut around target	yes	no
Track reconstruction	measured by inserting tracks	estimated to be less than 1%

TABLE VII. R From Data Set Comparison

x	Q^2	R
0.100	1 - 30	$-0.31 \begin{smallmatrix}+0.50\\-0.41\end{smallmatrix}$
0.080	1 - 15	$0.54 \begin{smallmatrix}+2.63\\-0.81\end{smallmatrix}$
0.059	1 - 15	$0.00 \begin{smallmatrix}+0.48\\-0.28\end{smallmatrix}$
0.036	1 - 8	$0.49 \begin{smallmatrix}+0.49\\-0.32\end{smallmatrix}$
0.025	1 - 6	$1.48 \begin{smallmatrix}+0.34\\-0.73\end{smallmatrix}$
0.019	1 - 5	$0.25 \begin{smallmatrix}+0.36\\-0.25\end{smallmatrix}$
0.014	1 - 3.5	$0.35 \begin{smallmatrix}+0.54\\-0.34\end{smallmatrix}$
0.010	0.9 - 2.5	$0.25 \begin{smallmatrix}+0.39\\-0.27\end{smallmatrix}$
0.007	0.8 - 1.75	$0.71 \begin{smallmatrix}+0.75\\-0.50\end{smallmatrix}$
0.005	0.6 - 1.25	$1.45 \begin{smallmatrix}+0.49\\-0.78\end{smallmatrix}$
0.003	0.4 - 0.8	$1.81 \begin{smallmatrix}+0.47\\-0.96\end{smallmatrix}$

TABLE VIII. Contributions to Systematic Errors in R

Source	Change in R
Change normalization by 5%	0.23
Shift beam momentum ΔE by 1 GeV	0.00
Change trackfinding efficiency by 5% at worst point, scaled back to no change at 100% efficiency	0.15
Change all inner edges of the geometric acceptance by 2.5 mm, the measured uncertainty in position	0.10

m	X	Q^2 (GeV^2)	$F_2^{D_2}$ (147 GeV) 1974		F_2^P (96 GeV) 1975		F_2^P (147 GeV) 1974		F_2^P (147 GeV) 1975		F_2^P (219 GeV) 1976		F_2^P Combined	
1 - 2	.66667	6.500	.077	.022										
1 - 2	.66667	7.500	.047	.019										
1 - 2	.66667	9.000	.063	.018	.059	.024			.074	.026			.066	.018
1 - 2	.66667	12.500	.065	.016	.035	.016	.054	.016	.037	.015	.057	.010	.049	.007
1 - 2	.66667	22.500	.054	.012	.015	.010	.035	.010	.034	.014	.037	.005	.033	.004
1 - 2	.66667	40.000	.066	.024			.018	.013	.056	.033	.036	.009	.031	.007
2 - 3	.40000	3.250			.680	.238			.276	.160			.371	.133
2 - 3	.40000	3.750			.111	.056			.214	.076			.147	.045
2 - 3	.40000	4.500	.302	.056	.168	.042			.221	.048			.191	.032
2 - 3	.40000	5.500	.302	.056	.165	.050			.276	.062			.221	.039
2 - 3	.40000	6.500	.342	.066	.205	.059	.323	.188	.266	.074			.241	.045
2 - 3	.40000	7.500	.265	.067	.135	.055	.210	.080	.292	.085	.211	.045	.168	.030
2 - 3	.40000	9.000	.261	.054	.159	.051	.175	.043	.190	.047	.178	.025	.171	.018
2 - 3	.40000	12.500	.310	.043	.131	.039	.193	.033	.127	.037	.195	.021	.175	.015
2 - 3	.40000	22.500	.286	.039	.274	.070	.158	.028	.127	.037	.208	.020	.165	.015
2 - 3	.40000	40.000	.198	.060			.277	.070	.184	.083	.158	.026	.173	.023
2 - 3	.40000	65.000									.199	.045	.179	.045
3 - 4	.11571	2.375			.716	.415			.418	.296			.518	.241
3 - 4	.28571	2.625			.409	.145			.183	.062			.348	.076
3 - 4	.28571	2.875			.300	.101			.404	.109			.345	.074
3 - 4	.28571	3.250	.484	.093	.230	.058			.394	.072			.295	.045
3 - 4	.28571	3.750	.643	.106	.338	.078			.322	.074			.330	.054
3 - 4	.28571	4.500	.374	.062	.242	.054			.378	.067			.296	.042
3 - 4	.28571	5.500	.461	.076	.263	.066	.234	.076	.327	.075	.381	.054	.314	.033
3 - 4	.28571	6.500	.276	.067	.297	.082	.251	.066	.355	.096	.288	.039	.292	.030
3 - 4	.28571	7.500	.338	.063	.343	.103	.175	.059	.311	.099	.246	.039	.242	.030
3 - 4	.28571	9.000	.360	.069	.262	.076	.276	.059	.224	.068	.309	.035	.285	.026
3 - 4	.28571	12.500	.446	.059	.122	.046	.252	.044	.255	.060	.299	.029	.250	.020
3 - 4	.28571	22.500	.403	.055	.234	.084	.326	.050	.300	.066	.259	.025	.273	.021
3 - 4	.28571	40.000	.424	.140			.313	.114	.268	.131	.311	.045	.304	.040
3 - 4	.28571	65.000									.330	.061	.330	.061
4 - 5	.22222	1.875			.146	.146			.382	.272			.199	.129
4 - 5	.22222	2.125	.620	.213	.406	.105			.194	.074			.264	.060
4 - 5	.22222	2.375	.453	.140	.369	.085			.229	.067			.279	.053
4 - 5	.22222	2.625	.661	.158	.182	.069			.559	.110			.288	.056
4 - 5	.22222	2.875	.529	.143	.339	.098			.219	.073			.262	.059
4 - 5	.22222	3.250	.450	.093	.289	.070			.372	.075			.328	.051
4 - 5	.22222	3.750	.487	.098	.430	.096	.204	.204	.501	.101			.437	.066
4 - 5	.22222	4.500	.522	.078	.279	.064	.307	.069	.363	.072	.304	.041	.309	.028
4 - 5	.22222	5.500	.497	.067	.187	.062	.311	.066	.260	.067	.273	.036	.253	.026
4 - 5	.22222	6.500	.407	.069	.264	.068	.268	.073	.370	.103	.263	.039	.272	.031
4 - 5	.22222	7.500	.505	.108	.197	.068	.295	.086	.271	.102	.282	.044	.270	.034
4 - 5	.22222	9.000	.519	.088	.259	.067	.242	.059	.409	.102	.359	.041	.321	.030
4 - 5	.22222	12.500	.562	.074	.305	.084	.212	.045	.419	.087	.333	.033	.302	.024
4 - 5	.22222	22.500	.544	.075	.348	.140	.407	.065	.212	.064	.372	.034	.349	.027
4 - 5	.22222	40.000	.748	.239			.495	.266	.663	.561	.233	.045	.243	.044
5 - 7	.10667	1.375			.412	.131			.231	.135			.324	.094
5 - 7	.10667	1.625			.381	.062			.360	.075			.381	.048
5 - 7	.10667	1.875			.323	.051			.277	.051			.300	.036
5 - 7	.10667	2.125	.467	.108	.309	.056			.310	.056			.310	.040
5 - 7	.10667	2.375	.571	.114	.446	.075			.242	.052			.308	.043
5 - 7	.10667	2.625	.497	.106	.421	.083			.263	.059			.316	.048
5 - 7	.10667	2.875	.561	.115	.356	.062	.346	.202	.341	.071			.347	.052
5 - 7	.10667	3.250	.594	.083	.285	.057	.514	.103	.428	.064	.409	.056	.365	.032
5 - 7	.10667	3.750	.681	.091	.383	.074	.217	.054	.362	.069	.288	.037	.294	.026
5 - 7	.10667	4.500	.687	.069	.325	.056	.322	.049	.314	.053	.336	.028	.329	.021

Table IX. Value of $F_2(x, Q^2)$ using R = 0.52

m	x	Q^2 (GeV^2)	$F_2^{D_2}$ (147 GeV) 1974		F_2^P (96 GeV) 1975		F_2^P (147 GeV) 1974		F_2^P (147 GeV) 1975		F_2^P (219 GeV) 1976		F_2^P Combined	
6 - 7	.16667	6.500	.628	.078	.380	.073	.309	.065	.274	.063	.362	.031	.336	.024
6 - 7	.16667	6.500	.574	.083	.370	.088	.192	.047	.283	.073	.355	.035	.301	.025
6 - 7	.16667	7.500	.565	.087	.346	.096	.187	.055	.305	.088	.322	.037	.288	.028
6 - 7	.16667	9.000	.705	.089	.330	.080	.323	.057	.338	.075	.363	.033	.361	.025
6 - 7	.16667	12.500	.656	.069	.432	.088	.306	.046	.273	.059	.357	.028	.339	.021
6 - 7	.16667	22.500	.480	.060	.774	.450	.271	.046	.530	.088	.404	.029	.379	.024
6 - 7	.16667	40.000					2.155	.733	.840	.511	.491	.062	.508	.061
7 - 9	.12500	1.125			.261	.060			.293	.105			.269	.052
7 - 9	.12500	1.375			.349	.044			.364	.063			.354	.036
7 - 9	.12500	1.625			.383	.054			.306	.057			.347	.034
7 - 9	.12500	1.875			.445	.067			.463	.073			.453	.049
7 - 9	.12500	2.125	.354	.113	.326	.065	.287	.295	.368	.069			.344	.047
7 - 9	.12500	2.375	.282	.091	.379	.079	.408	.175	.324	.069	.372	.091	.357	.044
7 - 9	.12500	2.625	.803	.160	.241	.073	.101	.059	.344	.077	.366	.066	.248	.034
7 - 9	.12500	2.875	.455	.115	.311	.090	.346	.107	.383	.088	.334	.058	.341	.040
7 - 9	.12500	3.250	.564	.095	.316	.070	.486	.091	.369	.069	.357	.042	.366	.030
7 - 9	.12500	3.750	.547	.092	.414	.090	.349	.075	.405	.083	.392	.045	.389	.033
7 - 9	.12500	4.500	.583	.073	.355	.068	.298	.055	.421	.071	.335	.030	.340	.023
7 - 9	.12500	5.500	.629	.087	.356	.084	.278	.057	.424	.088	.338	.034	.335	.026
7 - 9	.12500	6.500	.728	.107	.530	.121	.336	.072	.490	.113	.356	.039	.375	.032
7 - 9	.12500	7.500	.616	.129	.417	.126	.364	.088	.448	.120	.446	.050	.427	.039
7 - 9	.12500	9.000	.616	.092	.455	.114	.360	.075	.453	.102	.361	.038	.380	.031
7 - 9	.12500	12.500	.601	.076	.407	.112	.333	.056	.474	.092	.403	.035	.393	.027
7 - 9	.12500	22.500	.628	.090	(2.533	1.037)	.543	.134	.436	.103	.424	.036	.432	.033
7 - 9	.12500	40.000					(2.242	2.312)			.533	.100	.533	.100
9 - 11	.10000	.650			.492	.247							.492	.247
9 - 11	.10000	.950			.258	.067							.258	.067
9 - 11	.10000	1.125			.339	.040			.269	.062			.324	.034
9 - 11	.10000	1.375			.328	.047			.449	.076			.361	.040
9 - 11	.10000	1.625			.303	.054			.343	.068			.318	.042
9 - 11	.10000	1.875			.406	.072			.296	.065			.346	.046
9 - 11	.10000	2.125	.545	.161	.397	.081	.613	.173	.298	.069	.508	.086	.400	.043
9 - 11	.10000	2.375	.609	.156	.273	.076	.276	.107	.411	.090	.265	.057	.294	.038
9 - 11	.10000	2.625	.691	.161	.407	.115	.473	.133	.438	.098	.338	.065	.410	.046
9 - 11	.10000	2.875	.845	.178	.193	.079	.246	.094	.155	.064	.425	.070	.254	.037
9 - 11	.10000	3.250	.721	.116	.529	.100	.289	.076	.457	.086	.394	.047	.398	.034
9 - 11	.10000	3.750	.501	.101	.293	.084	.556	.110	.319	.082	.381	.048	.372	.035
9 - 11	.10000	4.500	.606	.088	.352	.078	.332	.063	.347	.072	.380	.036	.363	.027
9 - 11	.10000	5.500	.534	.089	.381	.099	.315	.067	.389	.095	.345	.039	.347	.030
9 - 11	.10000	6.500	.651	.111	.646	.153	.398	.089	.338	.102	.369	.045	.385	.036
9 - 11	.10000	7.500	.833	.144	.741	.193	.271	.079	.367	.122	.191	.037	.231	.032
9 - 11	.10000	9.000	.563	.102	.303	.108	.427	.088	.514	.125	.346	.045	.401	.036
9 - 11	.10000	12.500	.705	.095	.471	.176	.299	.061	.402	.095	.348	.037	.345	.030
9 - 11	.10000	22.500	1.316	.236	(6.318	3.628)	.782	.213	.522	.150	.427	.043	.446	.041
11 - 14	.06000	.650			.258	.262							.258	.262
11 - 14	.06000	.750			.299	.063							.299	.063
11 - 14	.06000	.850			.224	.040							.224	.040
11 - 14	.06000	.950			.285	.046							.285	.046
11 - 14	.06000	1.125			.302	.035			.281	.055			.296	.030
11 - 14	.06000	1.375			.307	.042			.236	.050			.278	.032
11 - 14	.06000	1.625			.334	.052			.492	.074			.386	.043
11 - 14	.06000	1.875			.374	.063			.378	.068			.376	.046
11 - 14	.06000	2.125	.645	.153	.525	.085	.263	.100	.358	.071	.322	.058	.361	.037
11 - 14	.06000	2.375	.506	.141	.403	.084	.425	.134	.516	.091	.356	.059	.415	.041
11 - 14	.06000	2.625	.844	.156	.443	.099	.278	.101	.293	.073	.307	.054	.317	.037
11 - 14	.06000	2.875	.661	.146	.478	.113	.188	.078	.297	.079	.467	.066	.353	.040

w	x	Q^2 (GeV^2)	F_2^{D2} (147 GeV) 1974		F_2^P (96 GeV) 1975		F_2^P (147 GeV) 1974		F_2^P (147 GeV) 1975		F_2^P (219 GeV) 1976		F_2^P Combined	
11 - 14	.08000	3.250	.669	.103	.363	.076	.224	.063	.452	.079	.258	.034	.266	.026
11 - 14	.08000	3.750	.728	.112	.614	.112	.381	.083	.379	.083	.299	.038	.345	.031
11 - 14	.08000	4.500	.618	.078	.344	.071	.412	.063	.373	.069	.419	.035	.401	.026
11 - 14	.08000	5.500	.869	.104	.377	.092	.314	.063	.590	.107	.363	.037	.371	.029
11 - 14	.08000	6.500	.650	.101	.485	.126	.415	.080	.509	.114	.406	.044	.424	.035
11 - 14	.08000	7.500	.770	.129	.217	.099	.244	.072	.413	.120	.430	.052	.350	.037
11 - 14	.08000	9.000	.647	.101	.324	.111	.499	.089	.334	.094	.418	.043	.410	.034
11 - 14	.08000	12.500	.767	.096	1.710	.728	.449	.072	.502	.103	.448	.030	.456	.033
11 - 14	.08000	22.500							(1.687	.617)	.519	.049	.519	.049
14 - 20	.05682	.650			.262	.032							.262	.032
14 - 20	.05682	.750			.361	.038							.361	.038
14 - 20	.05682	.850			.285	.036							.285	.036
14 - 20	.05682	.950			.322	.041							.322	.041
14 - 20	.05682	1.125			.326	.030			.272	.045			.309	.025
14 - 20	.05682	1.375			.349	.037			.420	.056			.371	.031
14 - 20	.05682	1.625			.413	.048			.367	.053			.392	.036
14 - 20	.05682	1.875			.364	.052			.317	.052			.340	.037
14 - 20	.05682	2.125	.704	.141	.317	.055	.356	.100	.464	.067	.438	.055	.395	.032
14 - 20	.05682	2.375	.469	.110	.420	.071	.351	.102	.446	.071	.290	.044	.372	.031
14 - 20	.05682	2.625	.763	.135	.305	.067	.223	.076	.204	.051	.418	.053	.294	.030
14 - 20	.05682	2.875	.725	.127	.359	.079	.448	.104	.387	.077	.385	.050	.367	.035
14 - 20	.05682	3.250	.690	.089	.389	.065	.336	.066	.253	.049	.276	.030	.292	.022
14 - 20	.05682	3.750	.676	.089	.346	.071	.296	.060	.363	.070	.345	.035	.341	.026
14 - 20	.05682	4.500	.633	.064	.367	.063	.318	.046	.434	.061	.406	.029	.366	.021
14 - 20	.05682	5.500	.659	.072	.411	.082	.284	.047	.434	.074	.405	.033	.376	.024
14 - 20	.05682	6.500	.740	.090	.508	.112	.448	.068	.436	.089	.465	.040	.461	.031
14 - 20	.05682	7.500	.657	.114	.276	.112	.260	.064	.479	.111	.428	.045	.379	.033
14 - 20	.05682	9.000	.750	.090	.620	.277	.442	.069	.384	.066	.405	.030	.412	.033
14 - 20	.05682	12.500	1.003	.136			.557	.099	.603	.116	.451	.034	.472	.031
14 - 20	.05682	22.500							(2.596	2.738)	(.483	.053)		
20 - 35	.03636	.650			.238	.024							.238	.024
20 - 35	.03636	.750			.238	.025							.238	.025
20 - 35	.03636	.850			.293	.029							.293	.029
20 - 35	.03636	.950			.224	.028							.224	.028
20 - 35	.03636	1.125			.279	.022			.366	.045			.296	.020
20 - 35	.03636	1.375			.362	.031			.408	.044			.377	.025
20 - 35	.03636	1.625			.358	.036			.387	.044			.370	.028
20 - 35	.03636	1.875			.344	.040			.339	.043			.342	.029
20 - 35	.03636	2.125	.388	.088	.350	.047	.429	.102	.260	.042	.376	.042	.340	.024
20 - 35	.03636	2.375	.490	.093	.336	.051	.343	.084	.317	.048	.352	.039	.338	.025
20 - 35	.03636	2.625	.511	.091	.309	.053	.361	.077	.469	.065	.437	.044	.347	.028
20 - 35	.03636	2.875	.714	.103	.363	.065	.273	.066	.500	.072	.398	.041	.384	.026
20 - 35	.03636	3.250	.723	.071	.306	.048	.325	.050	.461	.054	.383	.029	.370	.021
20 - 35	.03636	3.750	.757	.070	.461	.069	.333	.050	.[illegible]	.[illegible]	.380	.030	.377	.022
20 - 35	.03636	4.500	.787	.057	.413	.060	.387	.040	.[illegible]	.[illegible]	.382	.023	.369	.018
20 - 35	.03636	5.500	.668	.070	.521	.116	.481	.068	.357	.[illegible]	.478	.031	.457	.025
20 - 35	.03636	6.500	.694	.086	(.674	.271)	.476	.062	.571	.[illegible]	.531	.036	.523	.029
20 - 35	.03636	7.500	.756	.133	(.653	.714)	.521	.089	.380	.094	.412	.036	.422	.031
20 - 35	.03636	9.000	(.581	.105)			(.652	.125)	(.716	.153)	.414	.031	.414	.031
20 - 35	.03636	12.500					(1.395	.546)	(1.864	.847)	.529	.037	.529	.037
20 - 35	.03636	22.500									(1.219	.271)		
35 - 45	.02500	.650			.206	.038							.206	.038
35 - 45	.02500	.750			.298	.042							.298	.042
35 - 45	.02500	.850			.181	.035							.181	.035
35 - 45	.02500	.950			.280	.048							.280	.048
35 - 45	.02500	1.125			.322	.037			.350	.064			.329	.032

ω	x	Q^2 (GeV^2)	F_2^{D2} (147 GeV) 1974		F_2^P (96 GeV) 1975		F_2^P (147 GeV) 1974		F_2^P (147 GeV) 1975		F_2^P (219 GeV) 1976		F_2^P Combined	
35 - 45	.02500	1.375			.405	.050			.317	.058			.367	.038
35 - 45	.02500	1.625			.424	.059			.426	.068			.425	.045
35 - 45	.02500	1.875			.336	.060			.316	.064			.327	.044
35 - 45	.02500	2.125	.744	.189	.382	.074	.300	.134	.504	.067	.377	.060	.398	.039
35 - 45	.02500	2.375	.480	.129	.345	.079	.296	.118	.455	.069	.363	.058	.389	.039
35 - 45	.02500	2.625	.665	.134	.368	.092	.293	.092	.360	.084	.356	.059	.348	.039
35 - 45	.02500	2.875	.438	.099	.232	.083	.458	.117	.280	.079	.475	.067	.362	.041
35 - 45	.02500	3.250	.956	.089	.370	.084	.468	.080	.357	.070	.402	.044	.402	.031
35 - 45	.02500	3.750	.958	.122	.281	.112	.345	.073	.366	.063	.506	.052	.418	.036
35 - 45	.02500	4.500	.800	.090	(.714	.405)	.448	.067	.560	.069	.467	.040	.475	.032
35 - 45	.02500	5.500	1.023	.167			.325	.105	.491	.110	.451	.045	.449	.040
35 - 45	.02500	6.500	(.655	.277)			(.572	.226)	(.696	.293)	.494	.054	.494	.054
35 - 45	.02500	7.500									.456	.063	.456	.063
35 - 45	.02500	9.000									.562	.072	.562	.072
45 - 60	.01905	.650			.123	.024							.123	.024
45 - 60	.01905	.750			.207	.033							.207	.033
45 - 60	.01905	.850			.257	.040							.257	.040
45 - 60	.01905	.950			.318	.049							.318	.049
45 - 60	.01905	1.125			.323	.036			.373	.059			.337	.031
45 - 60	.01905	1.375			.432	.048			.331	.055			.318	.036
45 - 60	.01905	1.625			.342	.050			.370	.060			.353	.038
45 - 60	.01905	1.875			.302	.055			.358	.063			.326	.041
45 - 60	.01905	2.125	.824	.163	.405	.074	.280	.093	.561	.084	.254	.045	.333	.033
45 - 60	.01905	2.375	.622	.109	.400	.083	.466	.102	.407	.078	.412	.057	.410	.037
45 - 60	.01905	2.625	.816	.120	.355	.091	.484	.094	.324	.073	.425	.056	.367	.037
45 - 60	.01905	2.875	.636	.107	.426	.134	.441	.088	.361	.086	.398	.055	.401	.036
45 - 60	.01905	3.250	.876	.093	(.480	.185)	.377	.063	.461	.077	.426	.042	.419	.032
45 - 60	.01905	3.750	1.036	.111			.189	.157	.577	.100	.385	.043	.402	.038
45 - 60	.01905	4.500	1.068	.176			.366	.126	.638	.112	.407	.037	.477	.034
45 - 60	.01905	5.500							(.945	.522)	.613	.046	.513	.046
45 - 60	.01905	6.500									.516	.061	.516	.061
45 - 60	.01905	7.500									(.591	.120)		
60 - 80	.01429	.650			.256	.034							.256	.034
60 - 80	.01429	.750			.335	.043							.335	.043
60 - 80	.01429	.850			.286	.044							.286	.044
60 - 80	.01429	.950			.291	.044			.296	.304			.252	.044
60 - 80	.01429	1.125			.255	.031			.311	.050			.271	.026
60 - 80	.01429	1.375			.283	.039			.323	.052			.297	.031
60 - 80	.01429	1.625			.339	.052			.419	.062			.372	.040
60 - 80	.01429	1.875	.259	.193	.354	.064	.611	.312	.431	.066			.396	.045
60 - 80	.01429	2.125	.472	.082	.554	.103	.226	.054	.319	.060	.333	.049	.316	.030
60 - 80	.01429	2.375	.631	.107	(.453	.151)	.298	.069	.565	.090	.377	.050	.378	.035
60 - 80	.01429	2.625	.569	.065	(1.033	1.364)	.468	.077	.369	.080	.462	.056	.441	.039
60 - 80	.01429	2.875	.924	.113			.348	.073	.436	.099	.402	.053	.392	.039
60 - 80	.01429	3.250	.686	.157			.431	.113	.539	.097	.416	.039	.433	.034
60 - 80	.01429	3.750	(1.376	.256)			(.728	.194)	(.733	.224)	.487	.045	.467	.045
60 - 80	.01429	4.500							(1.343	1.364)	.454	.037	.454	.037
60 - 80	.01429	5.500									(.611	.078)		
80 - 120	.01000	.650			.264	.031							.264	.031
80 - 120	.01000	.750			.318	.036							.316	.030
80 - 120	.01000	.850			.285	.036			.237	.124			.261	.035
80 - 120	.01000	.950			.285	.039			.455	.078			.319	.035
80 - 120	.01000	1.125			.392	.034			.371	.043			.364	.027
80 - 120	.01000	1.375	.600	.120	.359	.042	.405	.098	.345	.041			.316	.028
80 - 120	.01000	1.625	.726	.078	(.424	.075)	.341	.068	.356	.044			.352	.037
80 - 120	.01000	1.875	.663	.069	(.394	.165)	.283	.056	.420	.052			.367	.038

ν	x	Q^2 (GeV^2)	F_2^{D2} (147 GeV) 1974		F_2^P (96 GeV) 1975		F_2^P (147 GeV) 1974		F_2^P (147 GeV) 1975		F_2^P (219 GeV) 1976		F_2^P Combined	
80 - 120	.01000	2.125	.739	.083			.440	.086	.422	.063	.404	.039	.413	.031
80 - 120	.01000	2.375	.857	.124			.436	.125	.576	.101	.447	.041	.463	.036
80 - 120	.01000	2.625	(.626	.195)			(.399	.232)	(.458	.129)	.461	.041	.461	.041
80 - 120	.01000	2.875	(1.442	.321)			(.667	.243)	(.338	.205)	.436	.041	.436	.041
80 - 120	.01000	3.250									.432	.033	.432	.033
80 - 120	.01000	3.750									.468	.053	.468	.053
80 - 120	.01000	4.500									(.690	.111)		
120 - 160	.00714	.650			.232	.031							.232	.031
120 - 160	.00714	.750			.211	.033			.457	.181			.219	.032
120 - 160	.00714	.850			.295	.043			.222	.060			.270	.035
120 - 160	.00714	.950			.437	.059			.312	.061			.377	.042
120 - 160	.00714	1.125	.577	.073	.350	.053	.323	.054	.425	.043			.375	.028
120 - 160	.00714	1.375	.617	.060	(.265	.299)	.231	.041	.408	.047			.367	.031
120 - 160	.00714	1.625	.738	.084			.352	.082	.344	.057	.431	.055	.382	.038
120 - 160	.00714	1.875	(1.147	.166)			(.497	.290)	(.834	.171)	.328	.034	.368	.034
120 - 160	.00714	2.125					(1.345	1.423)			.415	.036	.415	.036
120 - 160	.00714	2.375									.431	.041	.431	.041
120 - 160	.00714	2.625									.444	.057	.444	.057
120 - 160	.00714	2.875									(.466	.095)		
160 - 240	.00500	.450			.240	.034							.240	.034
160 - 240	.00500	.550			.280	.027							.280	.027
160 - 240	.00500	.650			.262	.027			.341	.069			.272	.025
160 - 240	.00500	.750			.261	.039	.694	.734	.287	.044			.273	.029
160 - 240	.00500	.850	.522	.138	(.362	.069)	.418	.088	.358	.041			.369	.037
160 - 240	.00500	.950	.511	.076	(.414	.149)	.131	.087	.336	.041			.299	.037
160 - 240	.00500	1.125	.654	.051			.362	.039	.310	.033	.371	.051	.319	.023
160 - 240	.00500	1.375	(.752	.099)			(.411	.118)	(.419	.077)	.401	.029	.401	.029
160 - 240	.00500	1.625					(1.642	1.830)			.412	.026	.412	.026
160 - 240	.00500	1.875									.490	.039	.490	.039
160 - 240	.00500	2.125									(.490	.067)		
240 - 400	.00312	.350			.213	.026							.213	.026
240 - 400	.00312	.450			.224	.019	.138	.094	.274	.044			.229	.017
240 - 400	.00312	.550	.384	.063	(.290	.039)	.181	.055	.283	.027			.263	.024
240 - 400	.00312	.650	.485	.045	(.202	.110)	.192	.057	.301	.027			.281	.024
240 - 400	.00312	.750	.538	.055			.270	.065	.322	.039	.496	.105	.326	.032
240 - 400	.00312	.850	(.738	.066)			(.263	.106)	(.479	.065)	.474	.043	.474	.043
240 - 400	.00312	.950	(.908	.146)			(.230	.163)	(.304	.119)	.322	.027	.322	.027
240 - 400	.00312	1.125					(2.182	1.317)	(1.247	1.424)	.411	.022	.411	.022
240 - 400	.00312	1.375									(.502	.040)		
400 - 600	.00200	.250			.155	.013			.240	.121			.156	.013
400 - 600	.00200	.350	.442	.035	(.220	.027)	.149	.049	.178	.018			.175	.017
400 - 600	.00200	.450	.434	.036			.165	.035	.264	.021			.238	.018
400 - 600	.00200	.550	(.429	.068)			(.269	.067)	(.168	.039)	.289	.025	.269	.025
400 - 600	.00200	.650					(1.216	1.065)	(.814	1.260)	.253	.017	.253	.017
400 - 600	.00200	.750									.268	.021	.268	.021
400 - 600	.00200	.850									(.414	.042)		
400 - 600	.00200	.950									(.900	.312)		
600 - 1000	.00125	.250	.340	.022	(.164	.021)	.153	.021	.211	.011			.199	.010
600 - 1000	.00125	.350	(.421	.036)			(.163	.043)	(.220	.023)	.200	.015	.200	.015
600 - 1000	.00125	.450					(1.045	.582)	(.912	1.458)	.276	.017	.276	.017
600 - 1000	.00125	.550									(.314	.041)		
600 - 1000	.00125	.650									(.587	.217)		
1000 - 1400	.00083	.250	(.336	.047)			(.157	.049)	(.229	.029)	.342	.010	.342	.010
1000 - 1400	.00083	.350									(.401	.022)		

TABLE X. Values of Parameters in fits to Eq. 14

Data set:	R = 0.52	R = 1.20 (1-x)/Q^2
a_1	0.0126 ± 0.0147	-0.0095 ± 0.0129
a_2	0.9986 ± 0.0394	1.0765 ± 0.0345
a_3	-0.6225 ± 0.0278	-0.6844 ± 0.0249
c_1	0.1577 ± 0.0095	0.1283 ± 0.0092
c_2	0.5329 ± 0.0195	0.4966 ± 0.0186
χ^2/329 DOF	343	335

TABLE XI . Value of Parameters in fits to Eq. 15

Data Set:	R = 0.52	R = 1.20 $(1-x)/Q^2$
P_3	0.517 ± 0.016	0.472 ± 0.104
g_{03}	0.679 ± 0.049	0.427 ± 0.087
P_5	0.345 ± 0.007	0.334 ± 0.116
g_{05}	1.28 ± 0.36	0.390 ± 0.205
κ	0.410 ± 0.100	0.436 ± 1.408
m_o^2	0.483 ± 0.029 GeV^2	0.391 ± 0.045 GeV^2
σ_γ	105 μbarn	121 μbarn
χ^2/273 DOF	285	361

Table XII

NACHTMANN MOMENTS FOR HYDROGEN

Q**2	N								
GEV**2	2	3	4	5	6	7	8	9	10
3.25	.186262	.053652	.022663	.011624	.006764	.004302	.002917	.002073	.001524
+-	.006597	.001665	.000705	.000401	.000272	.000203	.000158	.000126	.000102
3.75	.186974	.052362	.021904	.011167	.006446	.004056	.002718	.001910	.001393
+-	.007281	.001714	.000667	.000347	.000221	.000160	.000124	.000099	.000081
4.50	.184071	.051032	.021229	.010738	.006141	.003829	.002546	.001779	.001291
+-	.006939	.001684	.000662	.000329	.000195	.000132	.000097	.000076	.000061
5.50	.182329	.049092	.019867	.009769	.005482	.003297	.002141	.001465	.001047
+-	.007371	.001813	.000713	.000350	.000201	.000129	.000089	.000067	.000051
7.00	.179332	.046907	.018553	.008960	.004987	.002940	.001885	.001276	.000901
+-	.008202	.001810	.000666	.000303	.000159	.000094	.000061	.000042	.000032
9.00	.178386	.045097	.017478	.008298	.004461	.002619	.001644	.001083	.000755
+-	.008838	.001702	.000691	.000317	.000163	.000092	.000056	.000036	.000025
12.50	.172521	.042447	.016222	.007652	.004087	.002383	.001486	.000977	.000672
+-	.009285	.002001	.000787	.000377	.000198	.000112	.000067	.000043	.000028
22.50	.176594	.041830	.014749	.006634	.003438	.001953	.001187	.000760	.000508
+-	.010151	.002125	.000789	.000383	.000209	.000122	.000074	.000047	.000031
40.00	.184841	.043107	.013499	.005432	.002613	.001429	.000838	.000523	.000339
+-	.020135	.003632	.001201	.000609	.000364	.000231	.000151	.000099	.000066

NACHTMANN MOMENTS FOR DEUTERIUM

Q**2	N								
GEV**2	2	3	4	5	6	7	8	9	10
3.25	.318155	.086554	.035764	.018174	.010529	.006632	.004527	.003216	.002363
+-	.011528	.002532	.001052	.000595	.000402	.000298	.000231	.000184	.000148
3.75	.310267	.082082	.033717	.017029	.009777	.006139	.004112	.002893	.002110
+-	.012343	.002647	.001010	.000521	.000329	.000226	.000181	.000144	.000117
4.50	.309583	.080129	.032037	.015790	.008878	.005476	.003619	.002520	.001826
+-	.013507	.002619	.000970	.000468	.000273	.000184	.000136	.000107	.000087
5.50	.312418	.078836	.030965	.015037	.008325	.005056	.003289	.002258	.001618
+-	.015102	.002956	.001099	.000525	.000294	.000187	.000128	.000095	.000073
7.00	.297378	.073530	.028288	.013525	.007370	.004485	.002824	.001914	.001356
+-	.013141	.002754	.000994	.000455	.000240	.000142	.000092	.000064	.000048
9.00	.298693	.072539	.027048	.012589	.006713	.003933	.002481	.001657	.001158
+-	.014701	.003157	.001107	.000495	.000254	.000145	.000089	.000058	.000042
12.50	.300040	.070105	.025455	.011715	.006184	.003582	.002225	.001460	.001003
+-	.020461	.003529	.001249	.000570	.000297	.000167	.000099	.000062	.000041
22.50	.328509	.072134	.024072	.010644	.005506	.003135	.001915	.001239	.000839
+-	.038393	.005682	.001554	.000670	.000352	.000202	.000123	.000080	.000054
40.00	.281729	.078893	.025735	.010245	.004961	.002783	.001711	.001113	.000749
+-	.065236	.015635	.004569	.002010	.001176	.000756	.000494	.000326	.000215

TABLE 13

QUARK AND GLUON MOMENTS AND Λ_n

LEADING ORDER ANALYSIS

$Q^2 = 10\ GeV^2$

n	$\langle u \rangle_n$	$\langle d \rangle_n$	$\langle s \rangle_n$	$\langle G \rangle_n$	Λ_n(MeV)	χ^2
2	.3427	.1735	.0582	.4256	183 ± 282	2.98
3	.0926	.0374	--	.0893	369 ± 316	6.04
4	.0358	.0122	--	.0449	594 ± 270	2.90
5	.01696	.00525	--	.03117	753 ± 195	3.00
6	.00917	.00259	--	.01939	822 ± 150	4.29
7	.00542	.00141	--	.01238	867 ± 127	5.63
8	.00342	.00084	--	.00838	904 ± 111	6.90
9	.00227	.00054	--	.00602	938 ± 99	8.10
10	.00157	00037	--	.00462	971 ± 88	9.21

QUARK AND GLUON MOMENTS

LEADING ORDER ANALYSIS WITH COMMON Λ

$Q^2 = 10\ GeV^2$

n	$\langle u \rangle_n$	$\langle d \rangle_n$	$\langle s \rangle_n$	$\langle G \rangle_n$	Λ(MeV)	χ^2
2	.3473	.1832	0	.4696	637	4.52
4	.0357	.0123	--	.0522	"	2.93
6	.00931	.00239	--	.00656	"	5.37

TABLE (14)

F_2 MOMENT SLOPES AND QCD PREDICTIONS

Moments	Observed Slope	Leading Order QCD Predicted Values (4 flavors) $\lambda^{(m)}_{NS}/\lambda^{(n)}_{NS}$	$\lambda^{(m)}/\lambda^{(n)}$
$d\ell nM(n=6)/d\ell nM(n=4)$	1.62 ± 0.19	1.290	1.310
$d\ell nM(n=8)/d\ell nM(n=4)$	2.15 ± 0.24	1.499	1.533
$d\ell nM(n=10)/d\ell nM(n=4)$	2.61 ± 0.29	1.652	1.701
$d\ell nM(n=6)/d\ell nM(n=5)$	1.33 ± 0.12	1.162	1.166
$d\ell nM(n=10)/d\ell nM(n=6)$	1.62 ± 0.14	1.288	1.294
$d\ell nM(n=10)/d\ell nM(n=8)$	1.22 ± 0.09	1.109	1.107

TABLE 15

MOMENT ANALYSIS

(Including second order corrections)

n	$\langle u \rangle_n$	$\langle d \rangle_n$	$\langle s \rangle_n$	$\langle G \rangle_n$	A_n(MeV)	χ^2
2	.3521	.1819	.0137	.4523	91 ± 123	3.0
4	.0355	.0126	--	.0708	397 ± 171	2.6
6	.0091	.0027	--	.0286	503 ± 112	3.8
8	.0034	.0009	--	.0137	562 ± 80	5.4
10	.0015	.0004	--	.0076	599 ± 65	6.9

MOMENT ANALYSIS

(Including Fermi motion and second order corrections)

n	$\langle u \rangle_n$	$\langle d \rangle_n$	$\langle s \rangle_n$	$\langle G \rangle_n$	A_n(MeV)	χ^2
2	.3520	.1960	--	.4520	90 ± 119	3.1
4	.0355	.0126	--	.0708	397 ± 164	2.6
6	.0092	.0021	--	.0241	472 ± 108	3.8
8	.0035	.0004	--	.0089	500 ± 79	5.1
10	.0016	--	--	.0042	531 ± 52	7.1

TABLE 16

QUARK AND GLUON MOMENTS

(Including second order and Fermi motion corrections: global fit with common value of Λ)

n	$\langle u \rangle_n$	$\langle d \rangle_n$	$\langle s \rangle_n$	$\langle G \rangle_n$	Λ(MeV)	χ^2
2	.3389	.1871	--	.4740	459	10.3
4	.0353	.0130	--	.0883	"	2.7
6	.0093	.0021	--	.0225	"	3.8
8	.0035	.0032	--	.0065	"	5.4
10	.0016	--	--	.0019	"	8.6

Table A-1

ELASTIC CONTRIBUTION FOR HYDROGEN

Q**2	N								
GEV**2	2	3	4	5	6	7	8	9	10
3.25	.003945	.003400	.002877	.002411	.002008	.001666	.001378	.001138	.000938
3.75	.002625	.002299	.001981	.001692	.001437	.001216	.001027	.000865	.000728
4.50	.001527	.001363	.001199	.001047	.000909	.000787	.000680	.000587	.000505
5.50	.000820	.000745	.000668	.000596	.000529	.000468	.000414	.000365	.000322
7.00	.000375	.000347	.000318	.000290	.000263	.000238	.000215	.000195	.000176
9.00	.000161	.000151	.000141	.000131	.000121	.000112	.000103	.000095	.000088
12.50	.000051	.000049	.000046	.000044	.000041	.000039	.000037	.000034	.000032
22.50	.000006	.000006	.000006	.000005	.000005	.000005	.000005	.000005	.000005
40.00	.000001	.000001	.000001	.000001	.000001	.000001	.000001	.000001	.000001

ELASTIC CONTRIBUTION FOR DEUTERIUM

Q**2	N								
GEV**2	2	3	4	5	6	7	8	9	10
3.25	.005563	.004792	.004054	.003396	.002827	.002344	.001939	.001600	.001319
3.75	.003719	.003236	.002805	.002395	.002033	.001720	.001452	.001223	.001028
4.50	.002176	.001941	.001707	.001490	.001294	.001120	.000967	.000834	.000718
5.50	.001174	.001066	.000957	.000853	.000757	.000670	.000591	.000522	.000460
7.00	.000540	.000500	.000458	.000417	.000378	.000343	.000310	.000280	.000252
9.00	.000233	.000219	.000204	.000189	.000175	.000162	.000149	.000137	.000126
12.50	.000074	.000071	.000067	.000063	.000060	.000056	.000053	.000050	.000047
22.50	.000009	.000009	.000008	.000008	.000008	.000007	.000007	.000007	.000007
40.00	.000001	.000001	.000001	.000001	.000001	.000001	.000001	.000001	.000001

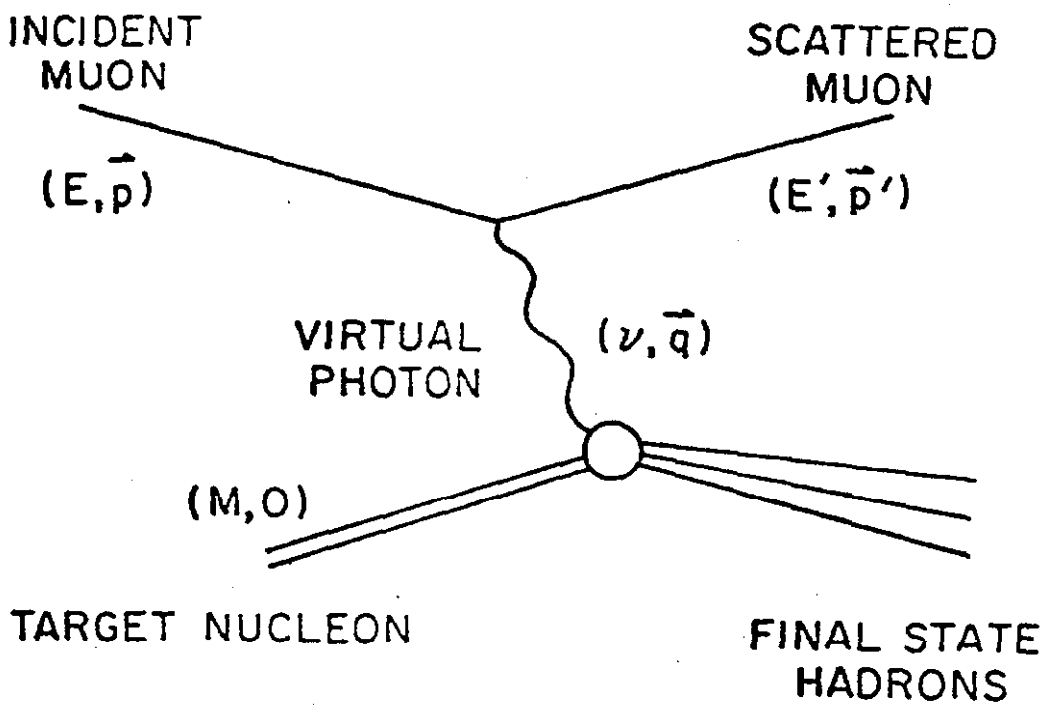

Fig. 1. Feynman diagram for one photon exchange.

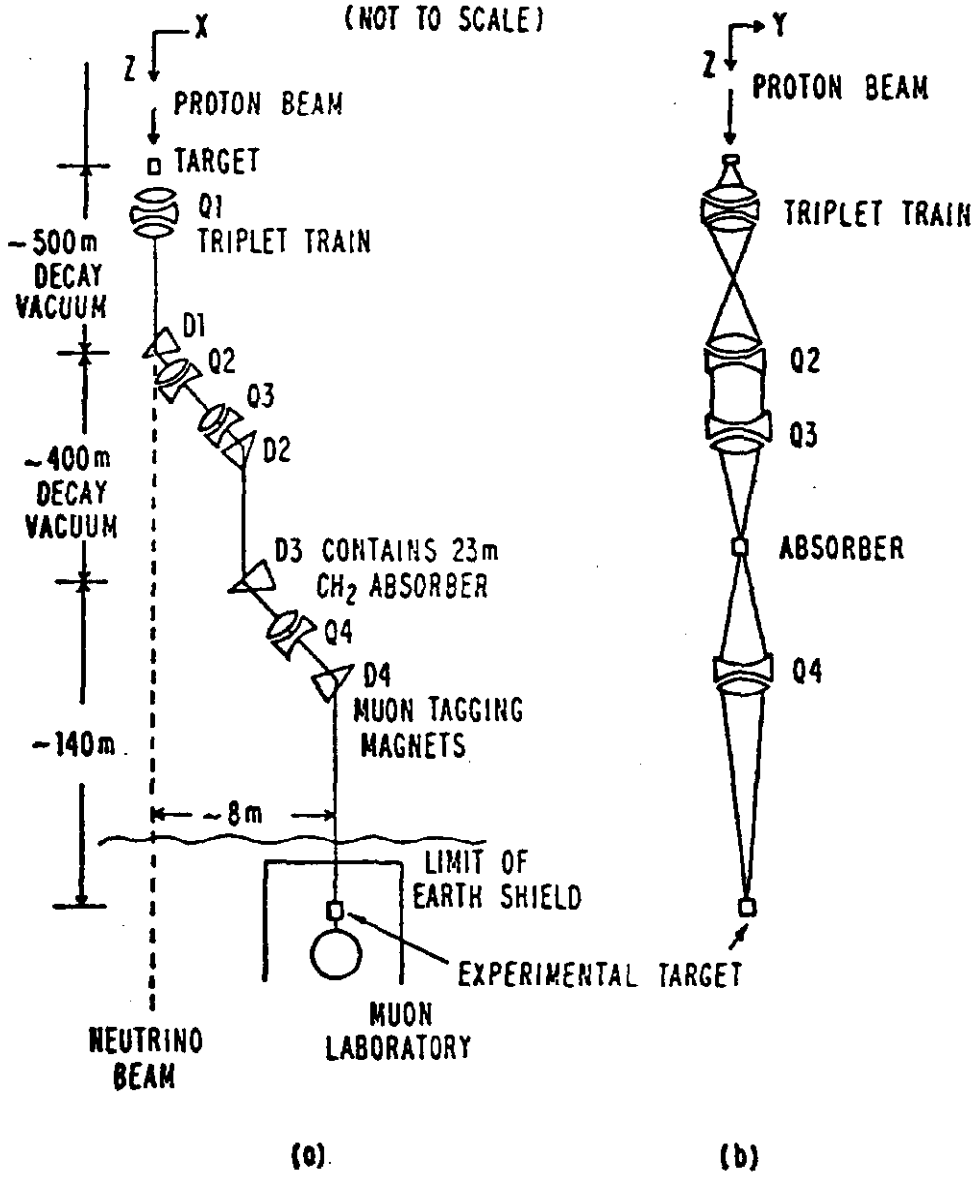

Fig. 2. Schematic diagram of Fermilab muon beam and beam optics.

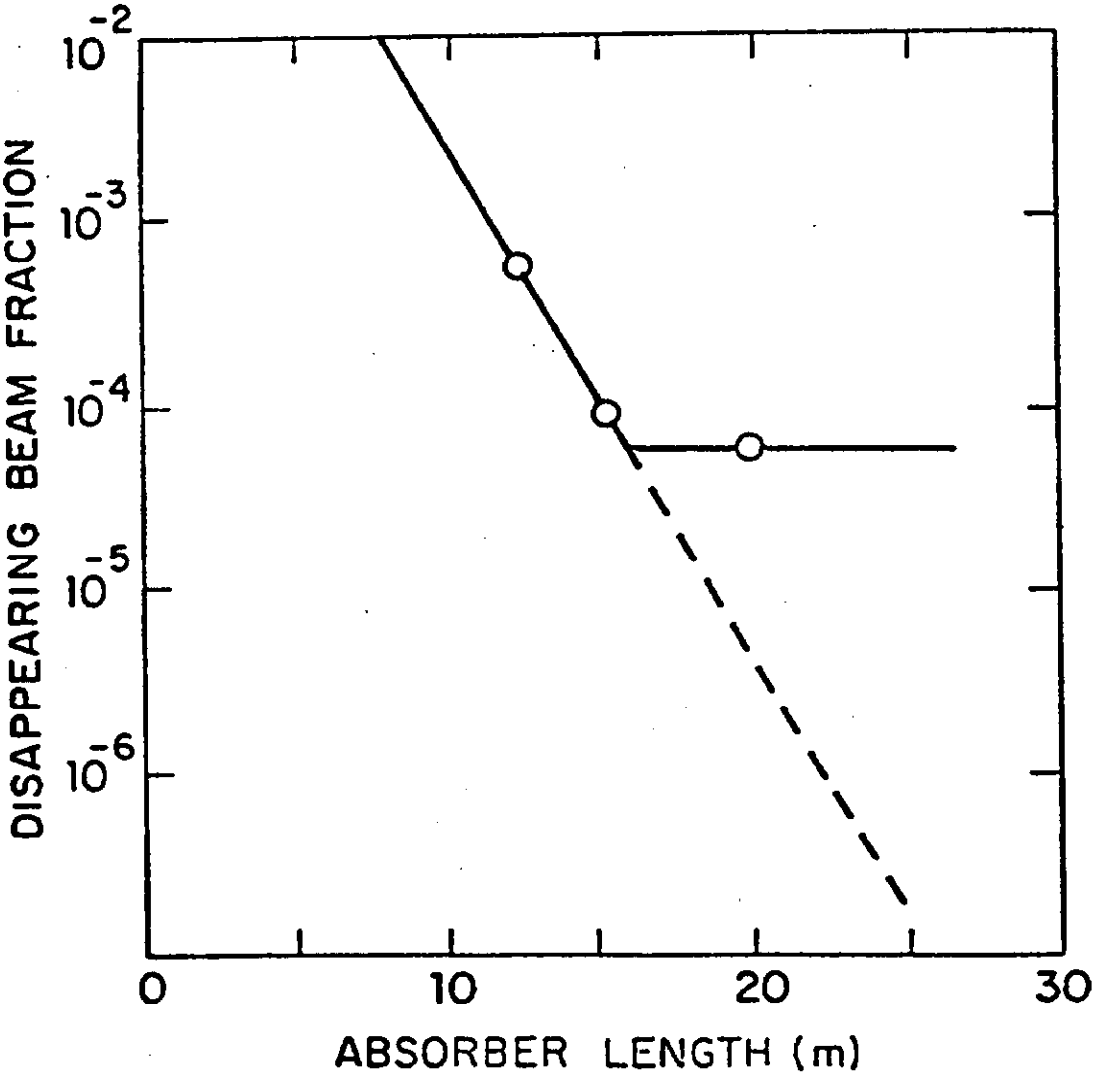

Fig. 3. Fraction of beam absorbed in steel hadron absorber as a function of polyethylene absorber in D3 magnets.

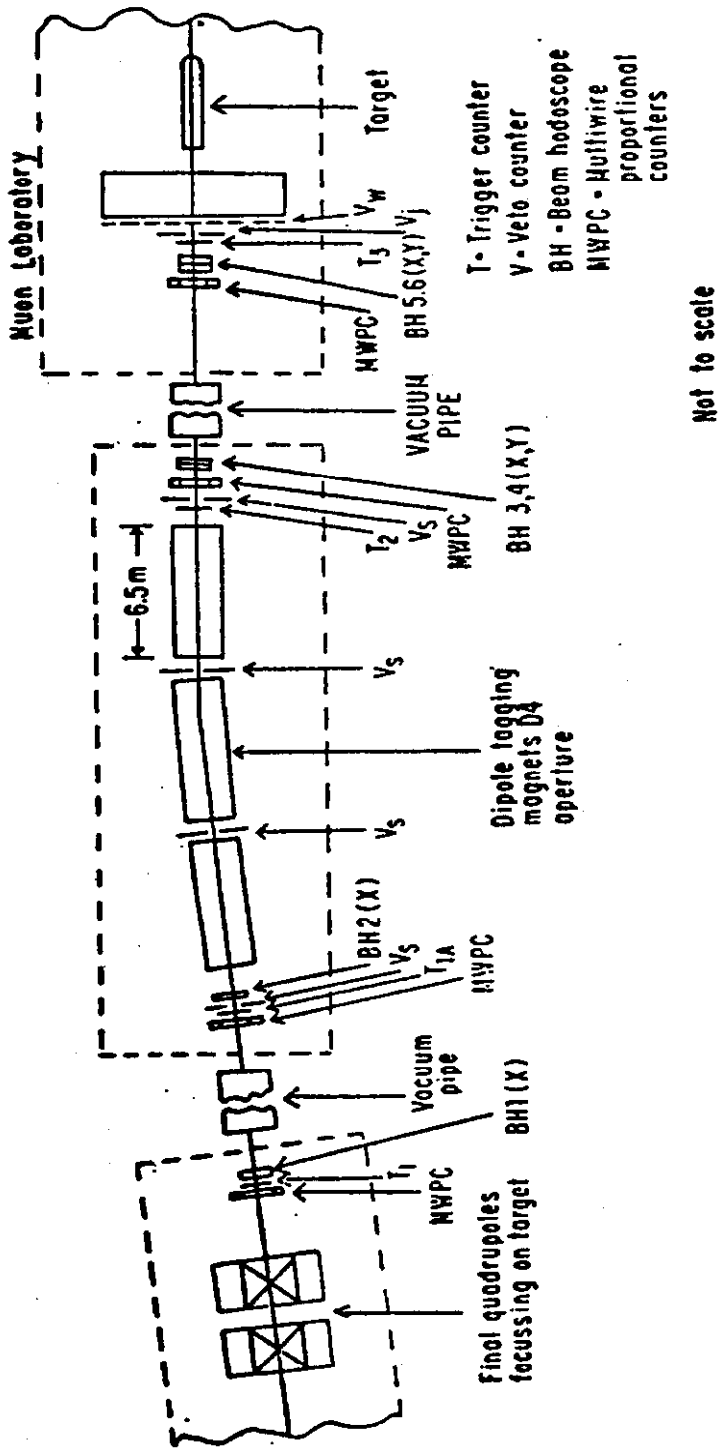

Fig. 4. Beam tagging system.

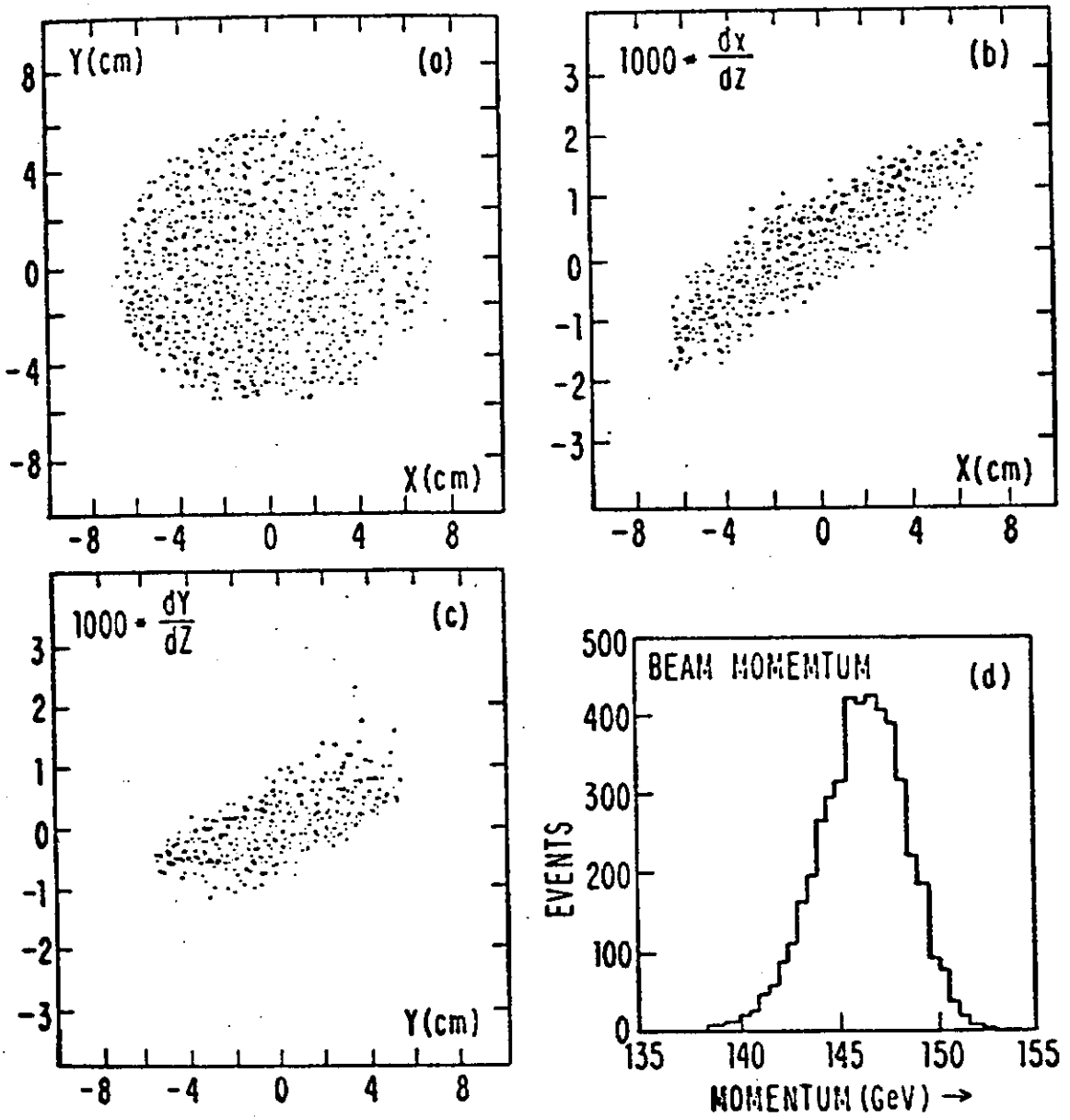

Fig. 5. Phase space of 147 GeV muon beam observed at experimental target. a) beam spot size; b) x vs. x slope correlations; c) y vs. y slope correlations; d) momentum distribution.

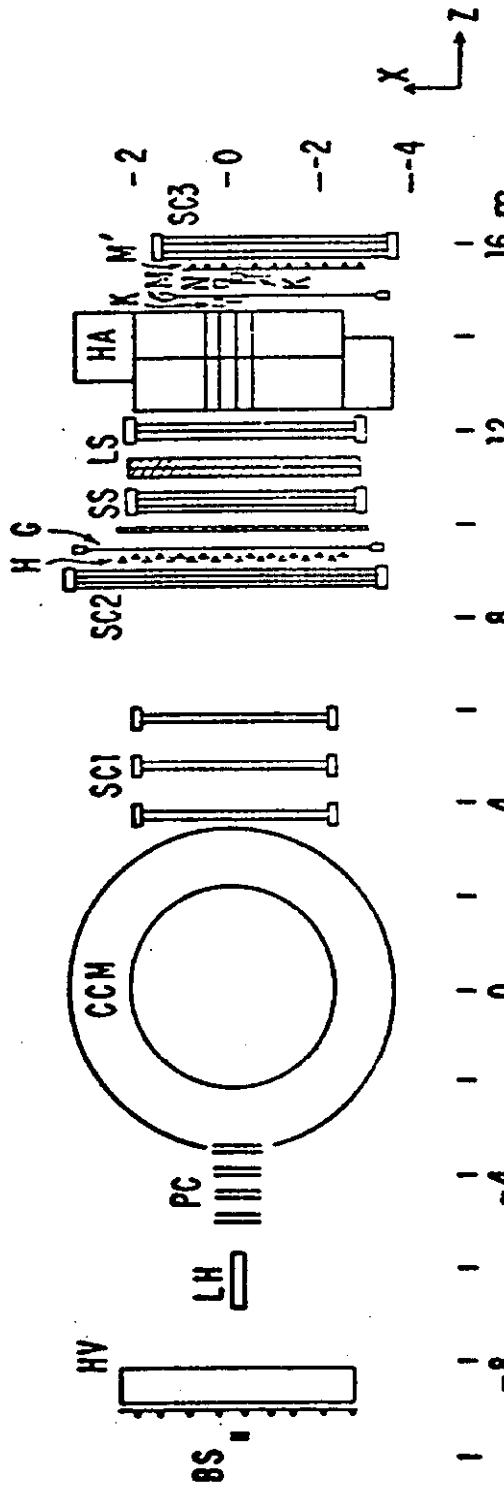

Fig. 6. Experimental apparatus seen from above. The muon beam enters at left. BS: last beam station; HV: Halo Veto wall and hodoscope; LH: Liquid Hydrogen target; PC: Multiwire proportional chambers; CCM: Chicago cyclotron magnet; SC1: Shift-register chambers; SC2: 6 m chambers; H: H hodoscope; G: G hodoscope; SS: Steel wall and spark chambers for photon and electron detection; LS: lead wall and spark chambers for hadron identification; HA: steel hadron absorber; K: beam veto hodoscope; M, N, M': muon hodoscopes; SC3: muon spark chambers.

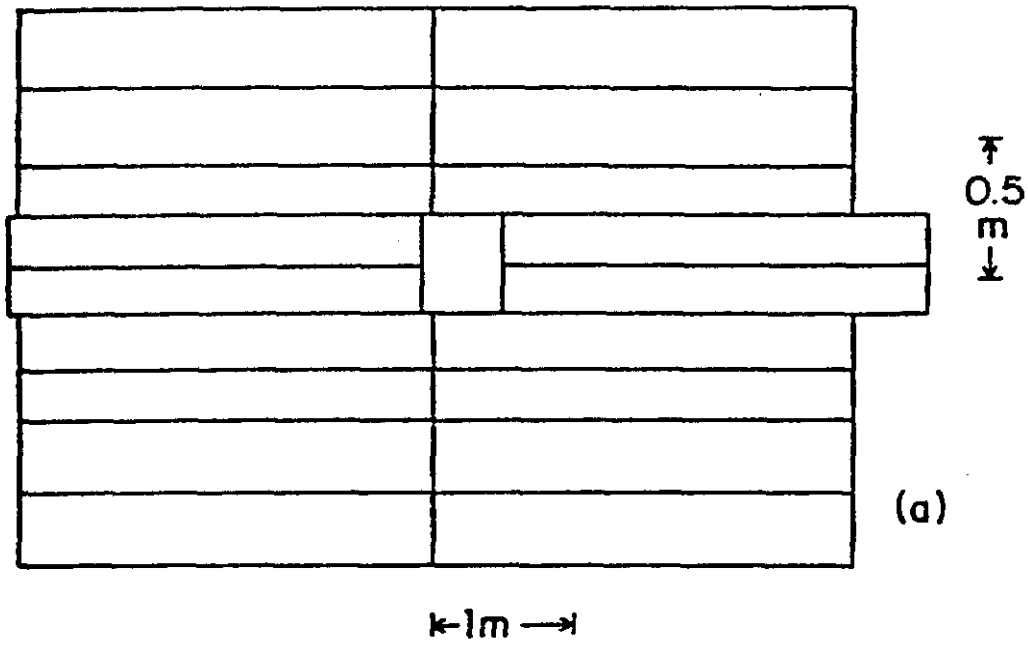

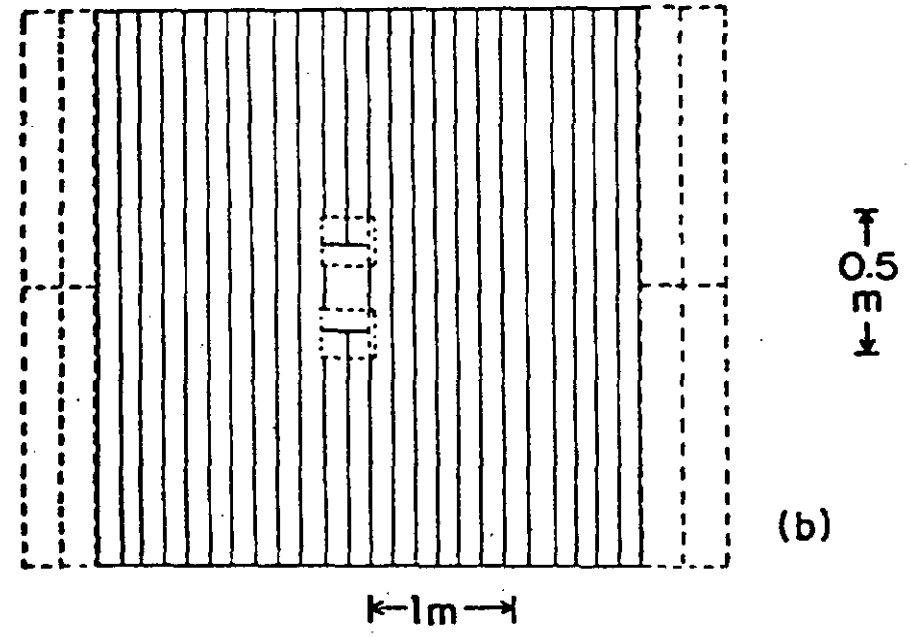

Fig. 7. Dimensions of (a) G and (b) H hodoscopes.

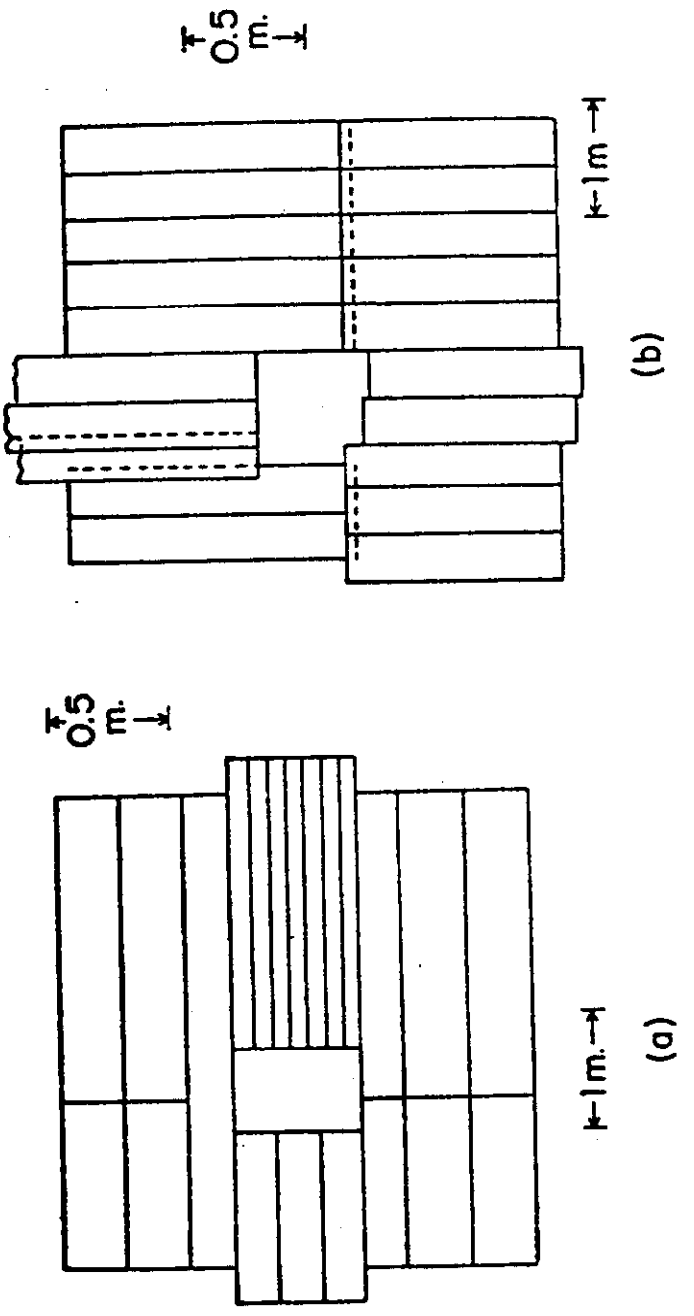

Fig. 8. Dimensions of (a) M, (b) M' and (c) N, hodoscopes. In the figure dotted lines show edges behind other counters.

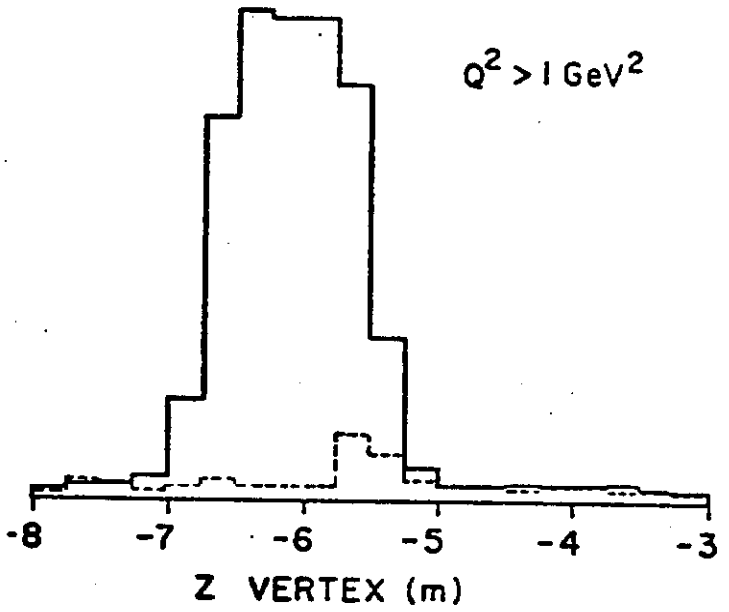

Fig. 9. Vertex distribution of analyzed events. Solid line: full target. Dotted line: empty target normalized to the same incident muon flux.

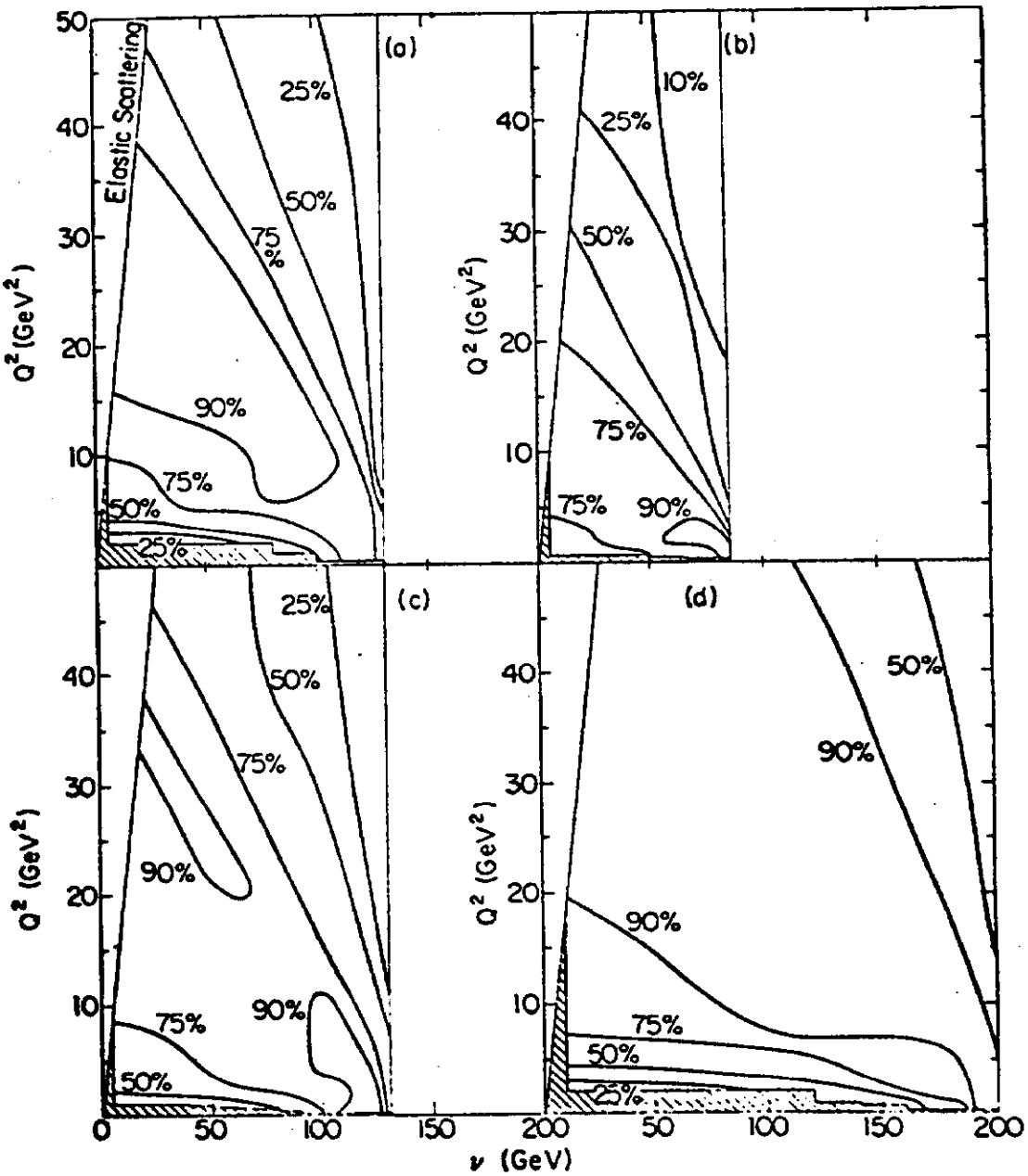

Fig. 10. Contours of constant acceptance for a) 1974 147-GeV data; b) 96-GeV data; c) 1975 147-GeV data; d) 219-GeV data.

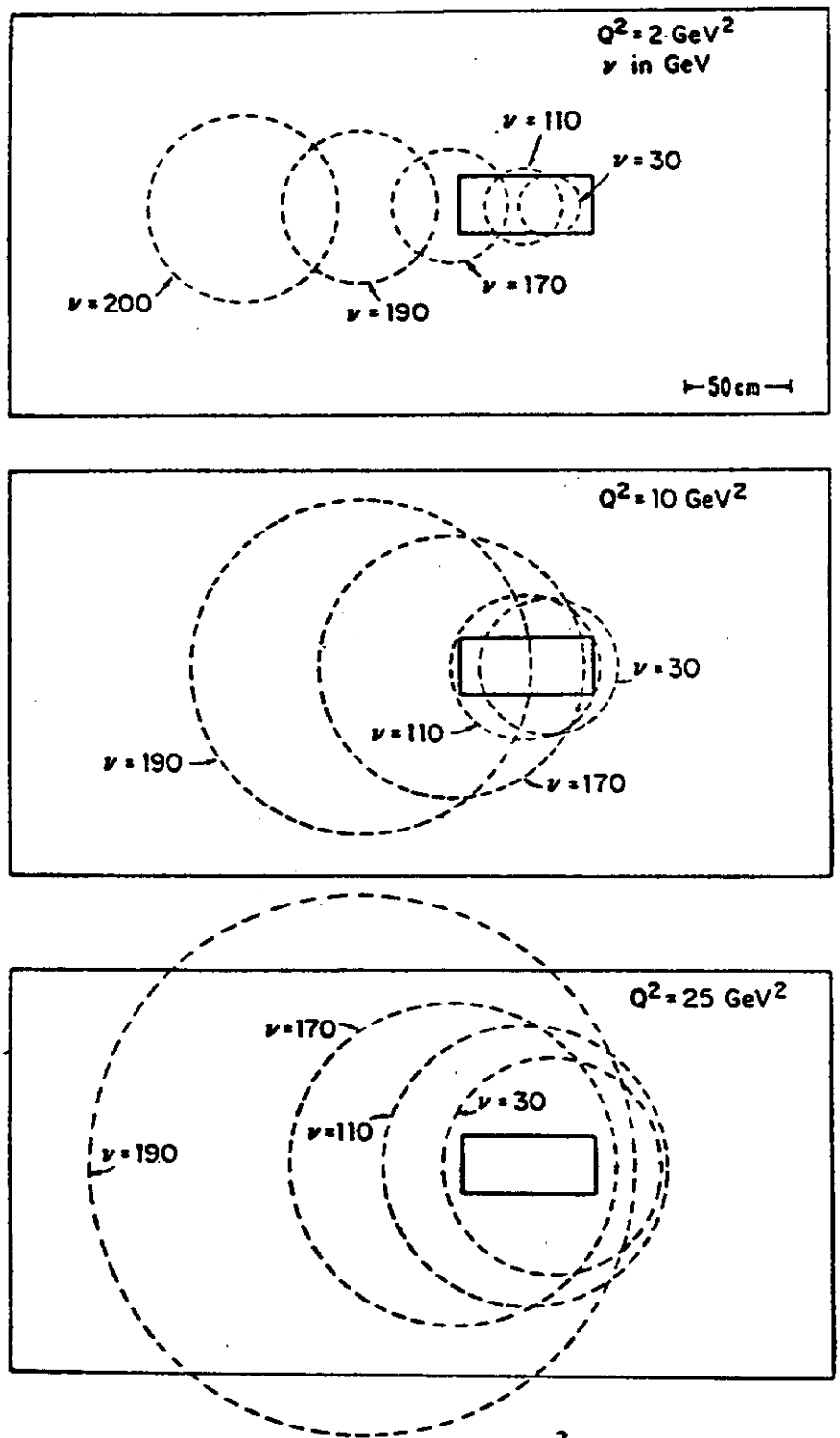

Fig. 11. Position of muons with constant Q^2, for several values of ν at the muon hodoscopes for the 219 GeV data.

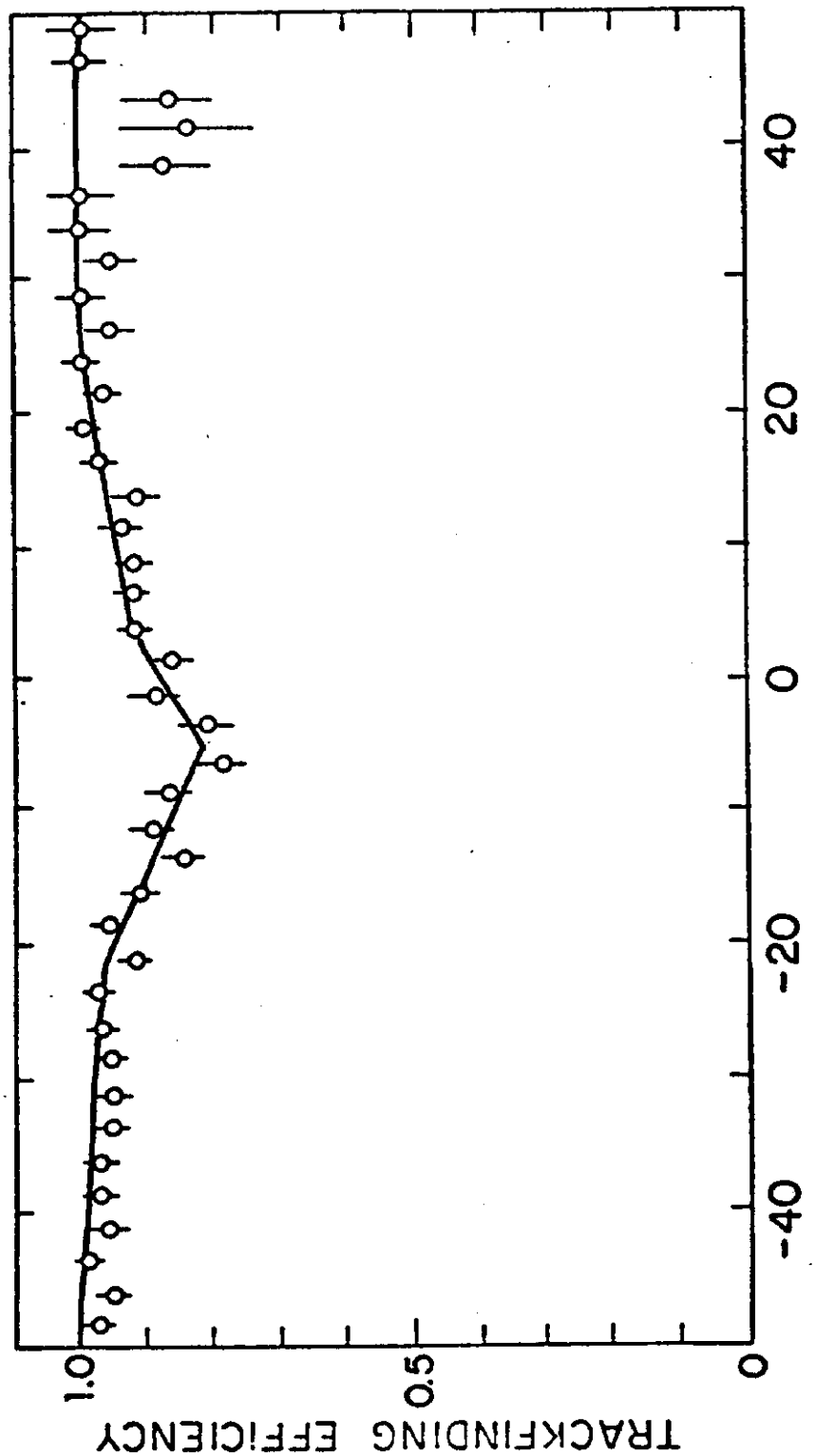

Fig. 12. Trackfinding efficiency across the 6 m chambers for the 21 9 GeV data.

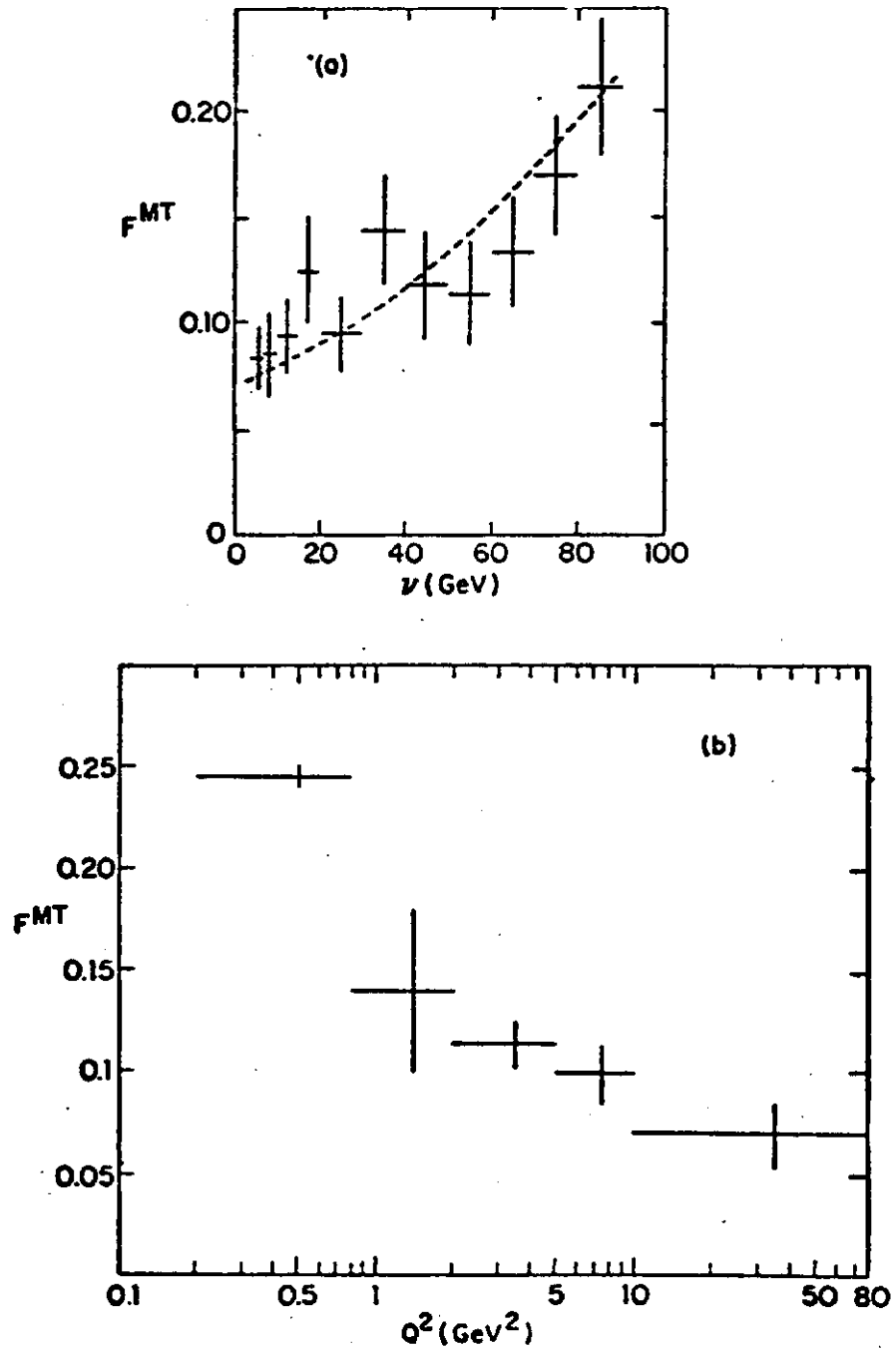

Fig. 13. Empty-target fraction for a) the 96 GeV data; b) the 219 GeV data

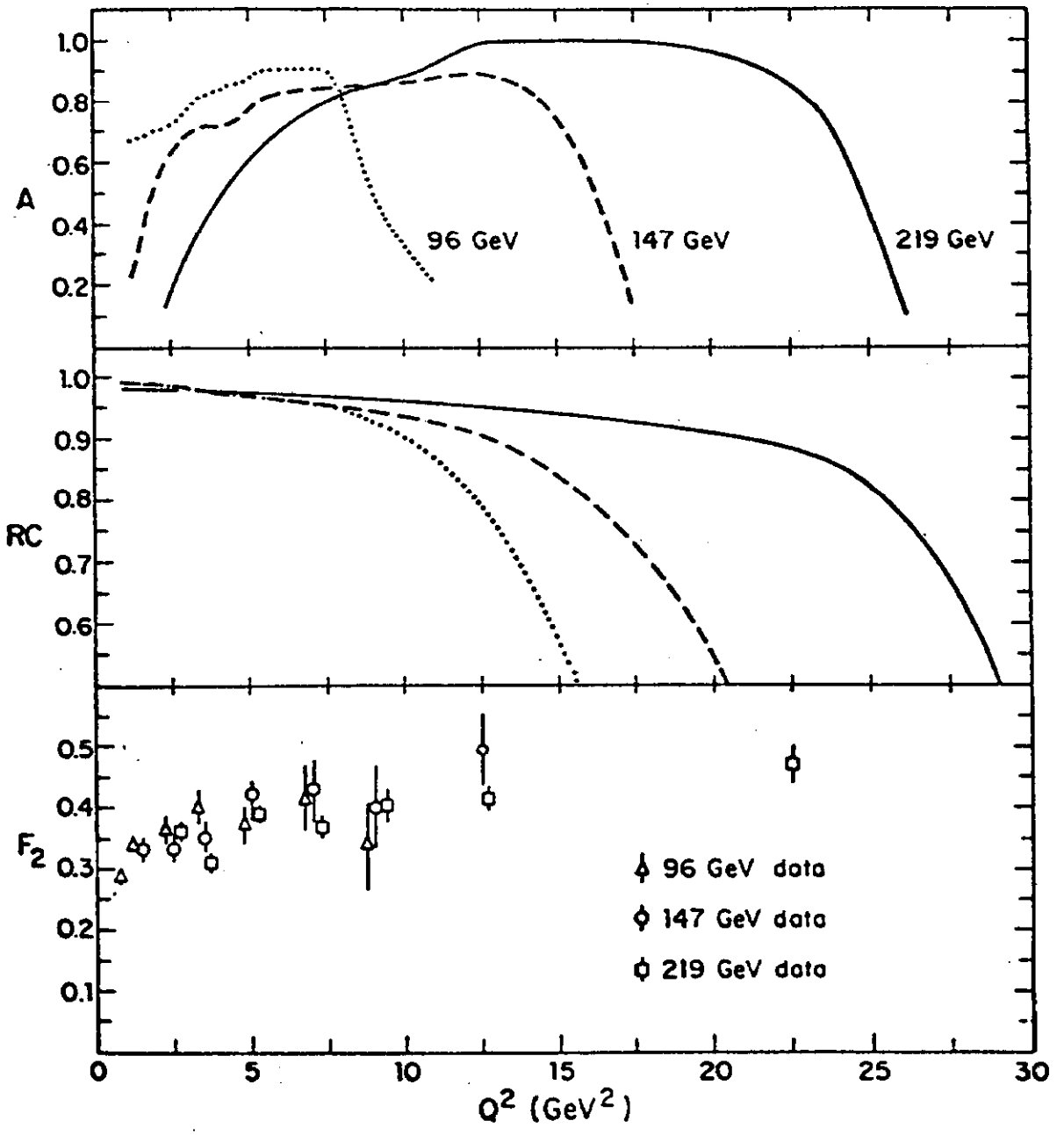

Fig. 14. Values of the acceptance, A, the inelastic radiative correction RC, and the extracted structure function F_2 versus Q^2 for $9 < \omega < 20$.

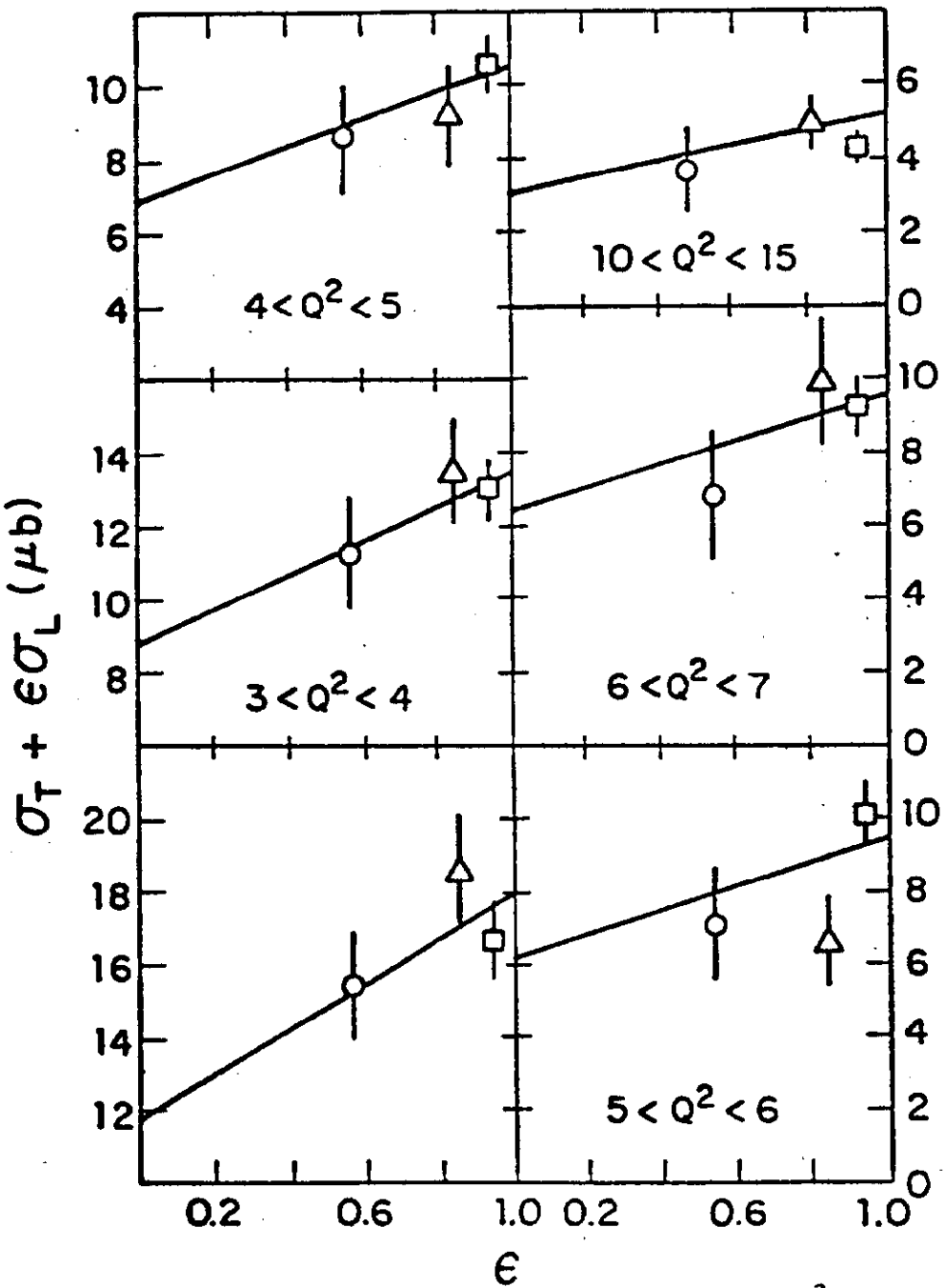

Fig. 15. Virtual photoproduction cross section for several Q^2 bins with $100 < W^2 < 144$ GeV^2. The straight line in each case is the best fit with R = 0.52.

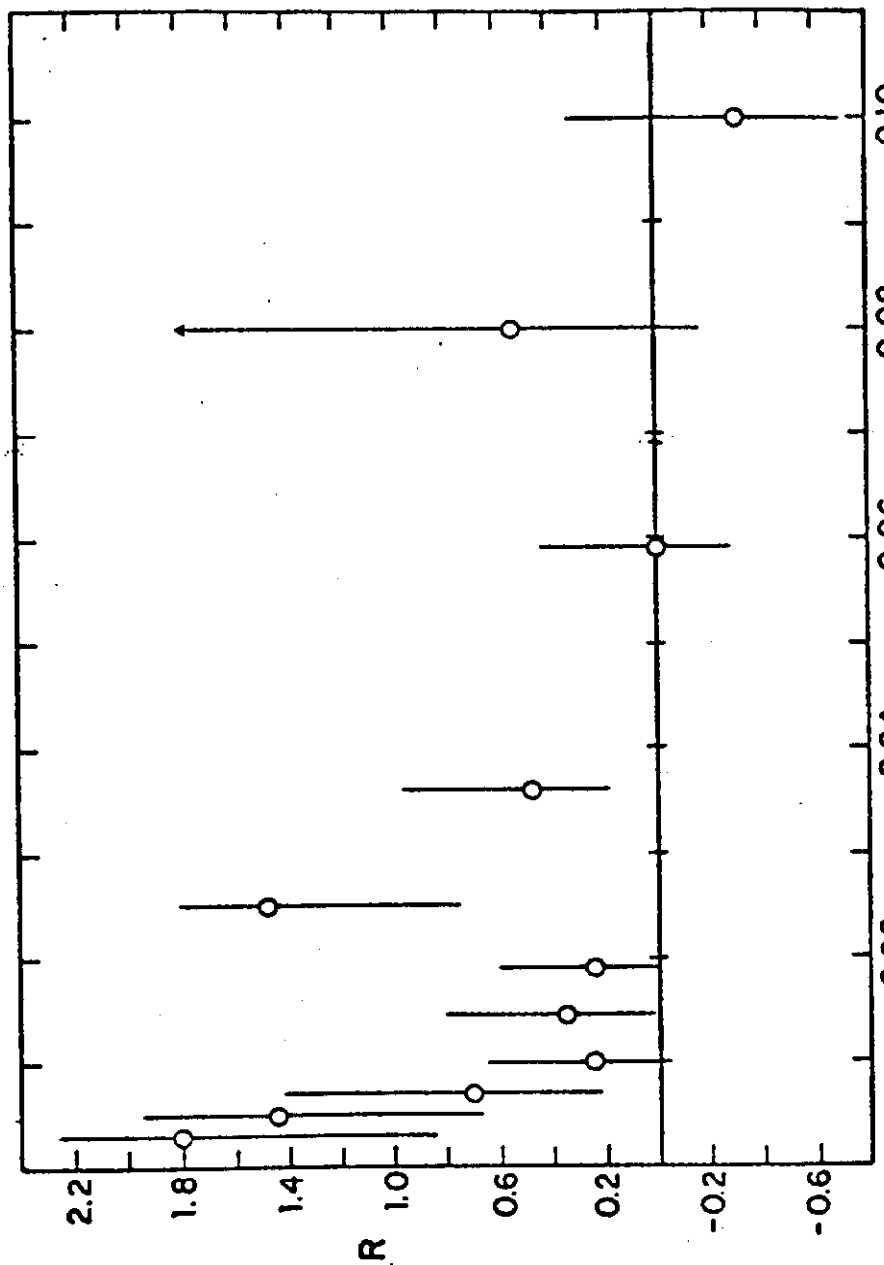

Fig. 16. Extracted values of R vs. x using the data comparison technique. The average value of Q^2 for each point is different, and decreases with x.

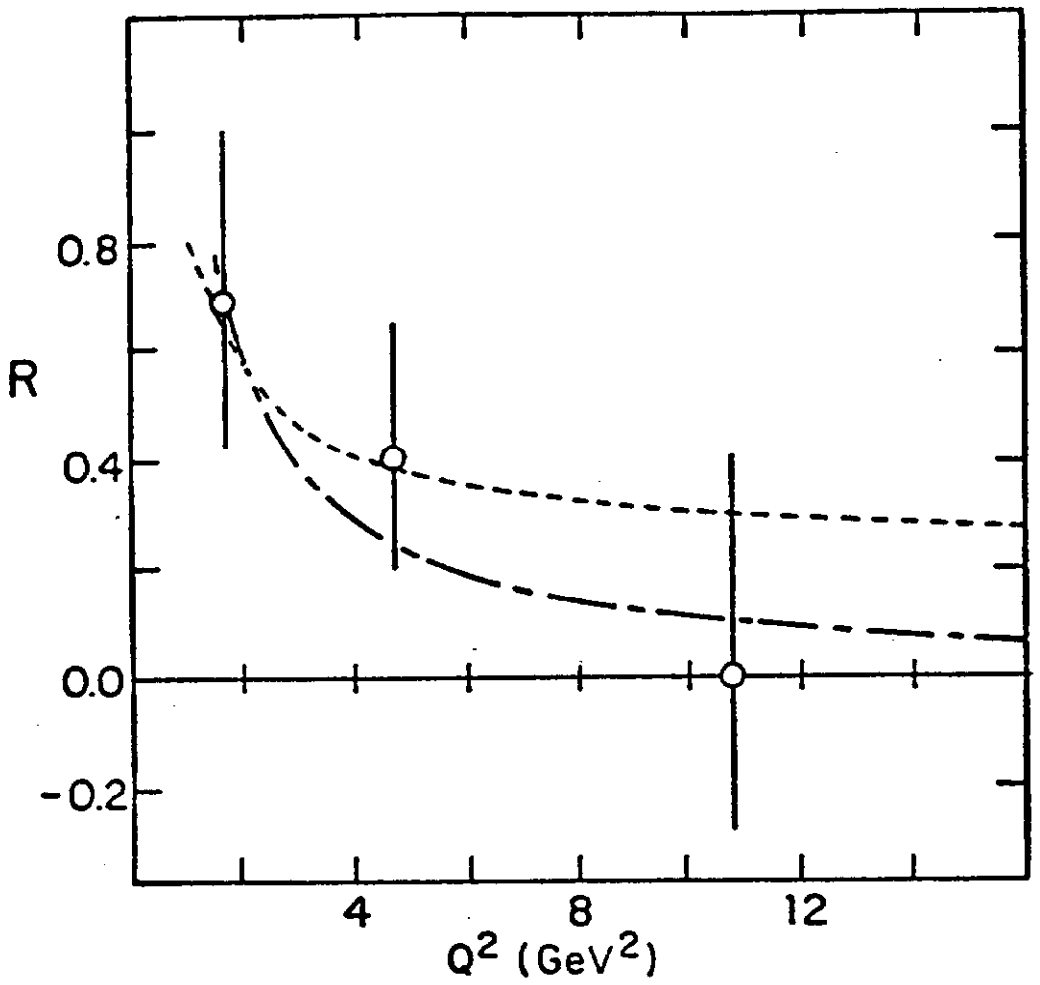

Fig. 17. Extracted values of R vs. Q^2. The dashed curve is $R = 1.18(1-x)/\ln(Q^2/\Lambda^2)$ with $\Lambda = 0.5$ GeV; the other curve is $R = 1.20(1-x)/Q^2$.

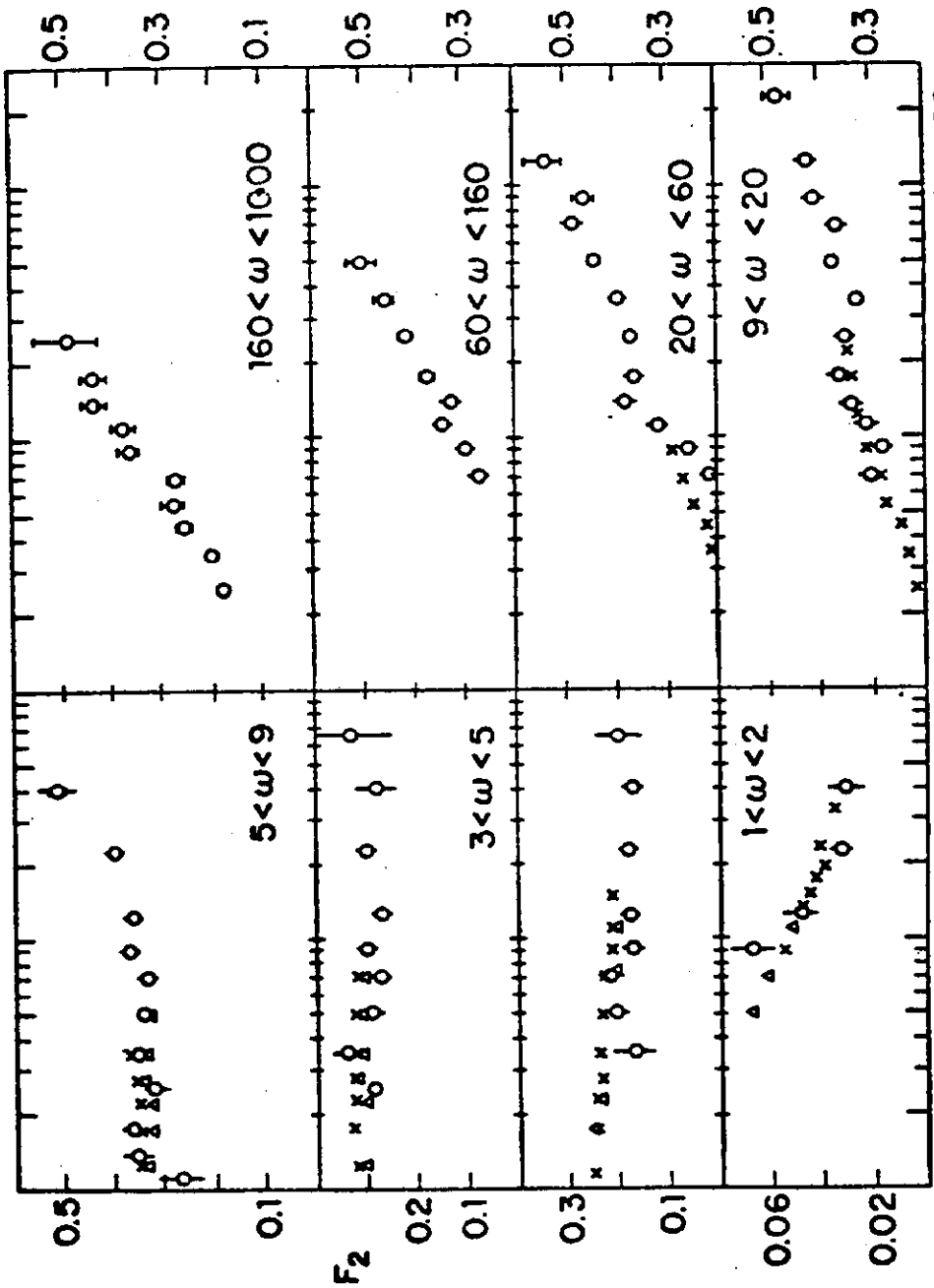

Fig. 18. F_2 for hydrogen as a function of Q^2 for various ω bins, using $R = 0.52$, showing the combined Fermilab data (circles), the MIT-SLAC data (triangles) (Ref. 28), and the SLAC data (crosses)(Ref. 33). The errors shown are statistical only. The horizontal bars indicate the effects of changing R to 0.69 and 0.37. Note the difference in scale and suppressed zeros on the ordinates.

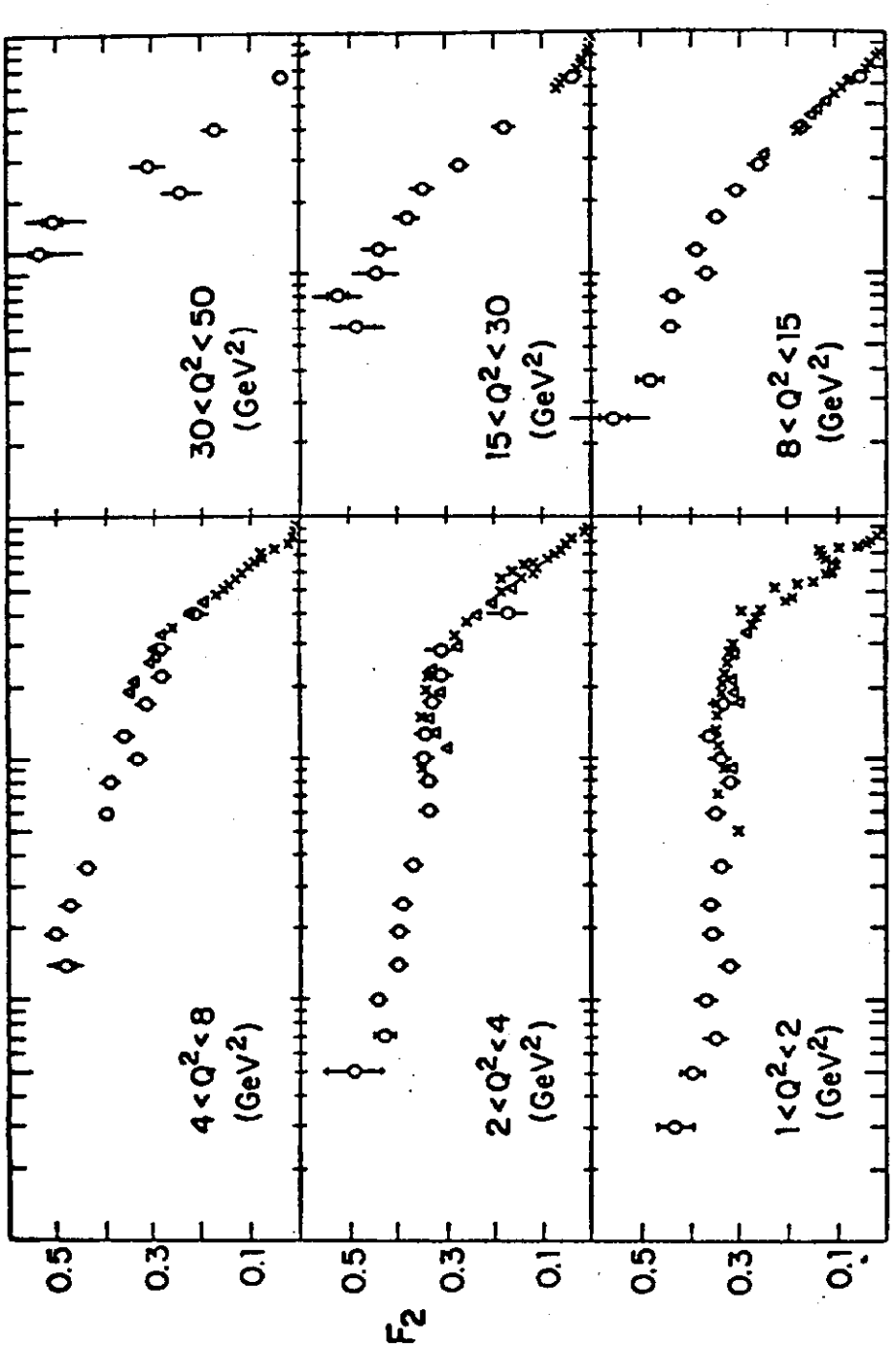

Fig. 19. F_2 for hydrogen as a function of x for various Q^2 bins, using R = 0.52. Additional SLAC/MIT points have been added.

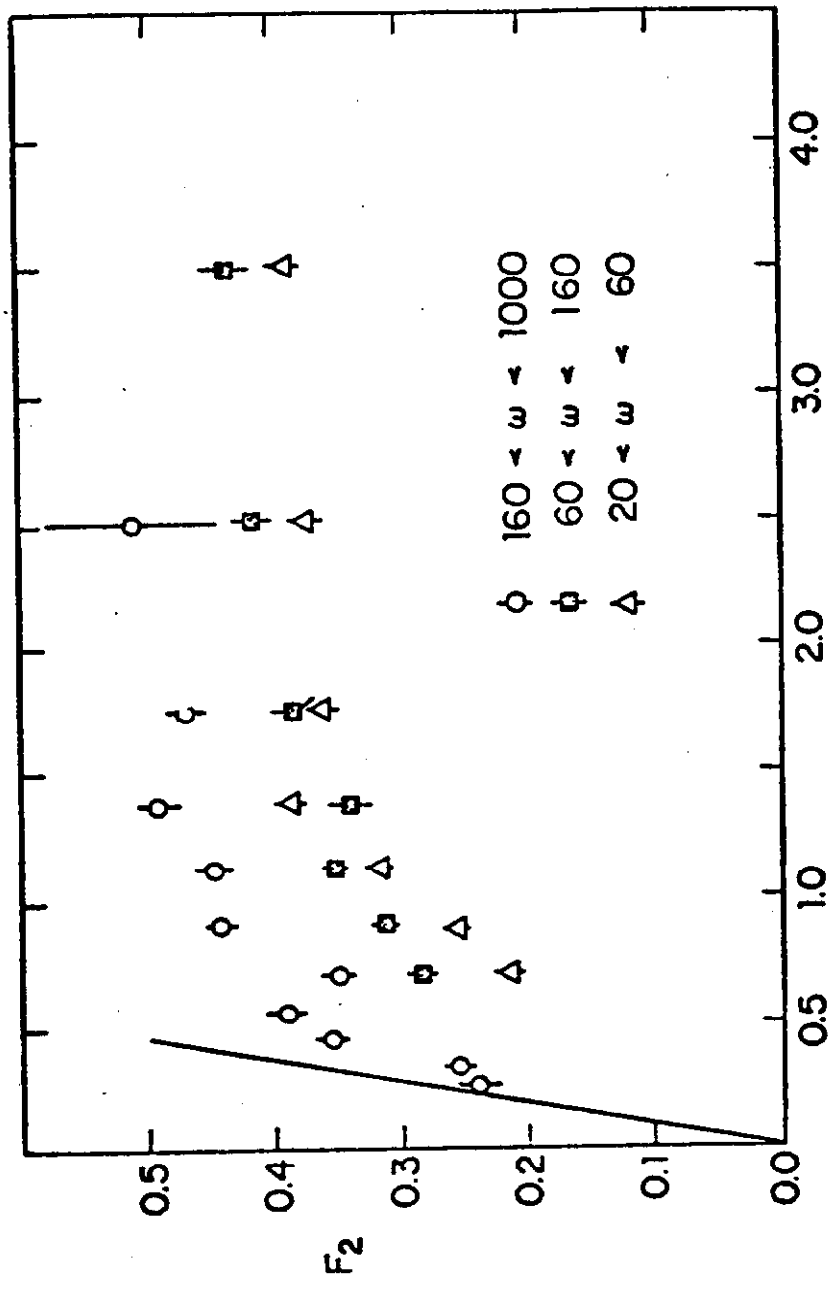

Fig. 20. F_2 for hydrogen as a function of Q^2 for several bands of ω. The line is the constraint on the low-Q^2 variation of F_2 imposed by the real photon cross section.

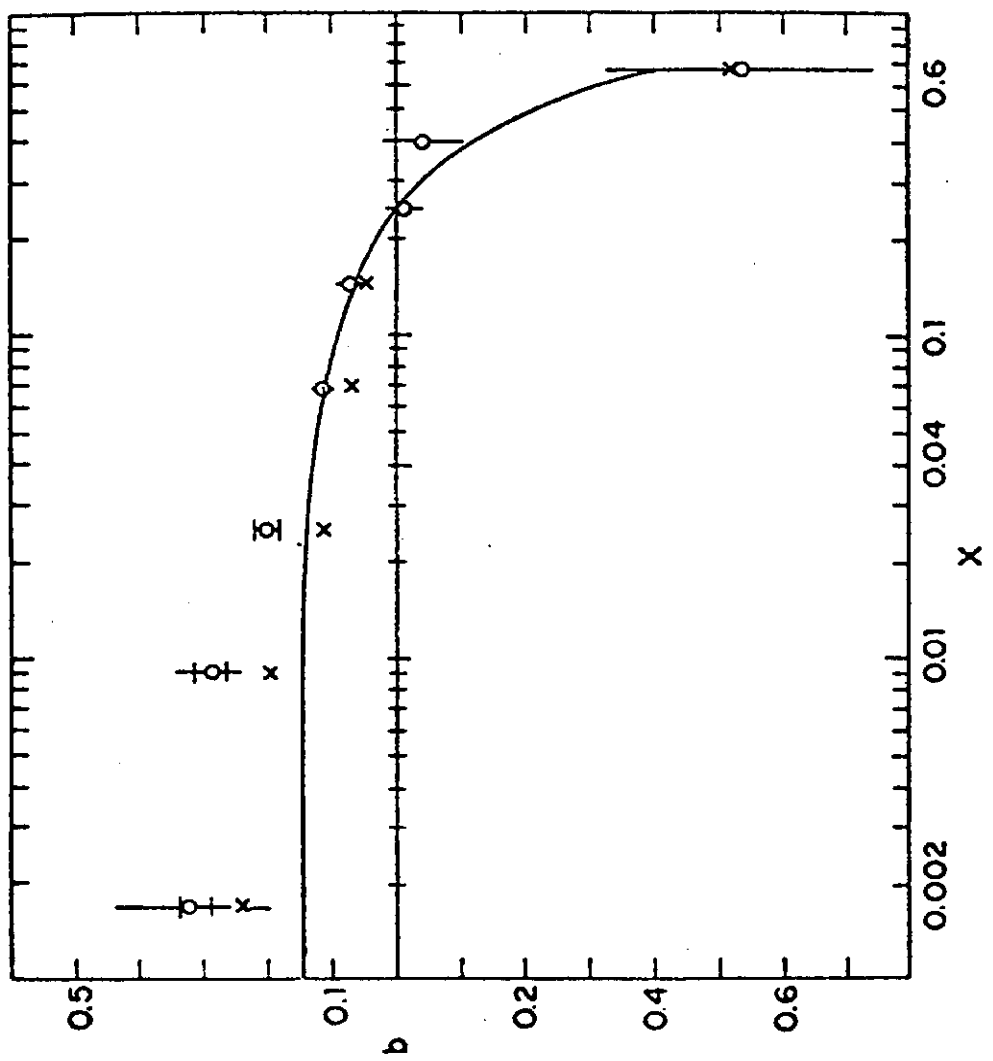

Fig. 21. The scaling violation parameter b of Eq. (13) as a function of x for all muon proton scattering data in this experiment. The horizontal bars indicate the change in b as R is changed from the central value of 0.52 to 0.69 or 0.37. The crosses are the values that would be obtained if we set R = 0. The errors are statistical only. The line is part of a global fit to the data using $b(x) = c_1 + c_2 \ln (1-x)[$Eq. (14)$]$. Also shown (dashed) is the simpler form $b(x) = 0.25 - x[$ Ref. (17)$]$.

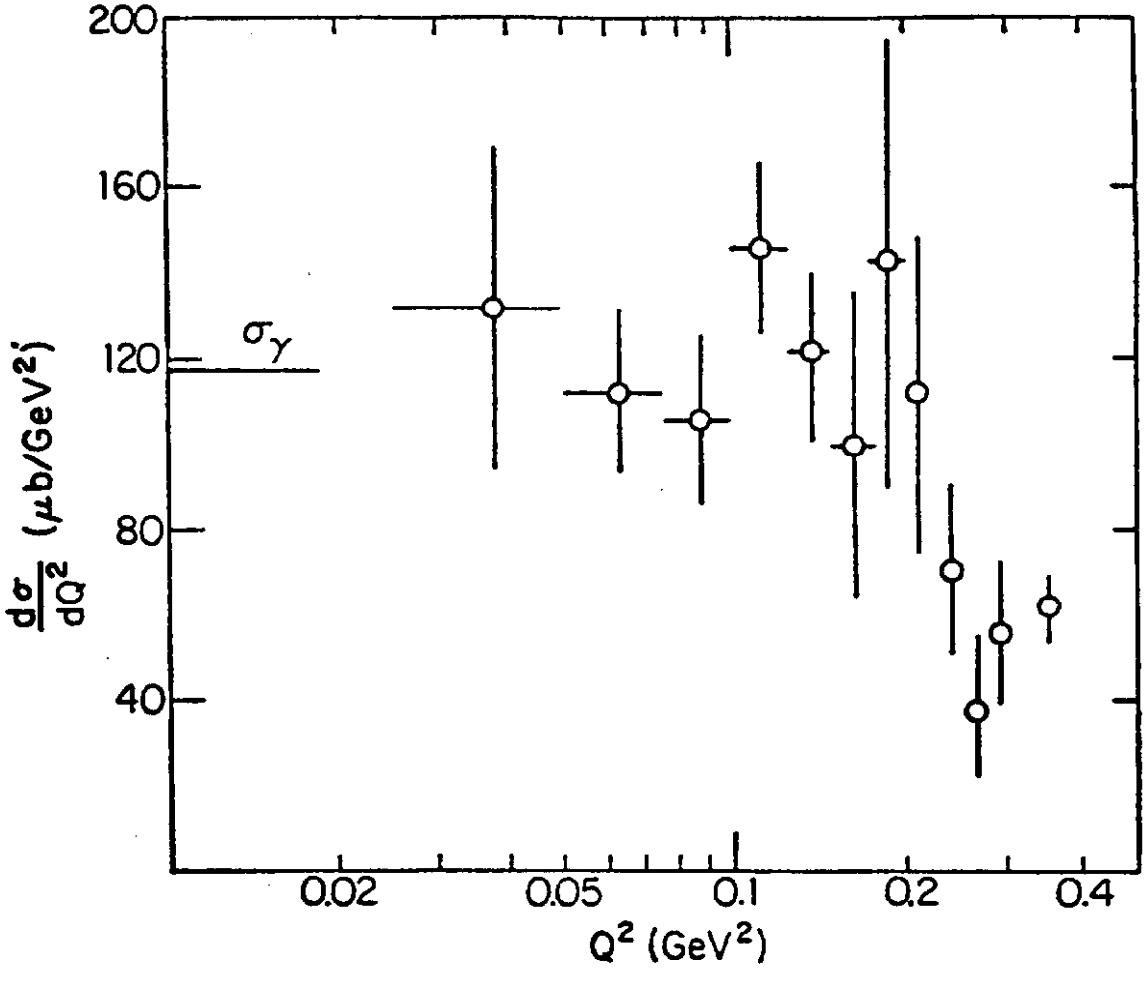

Fig. 22. $d\sigma/dQ^2 = (\sigma_T + \epsilon\sigma_L)$ as a function of Q^2 for $319 < W^2 < 375$ GeV^2

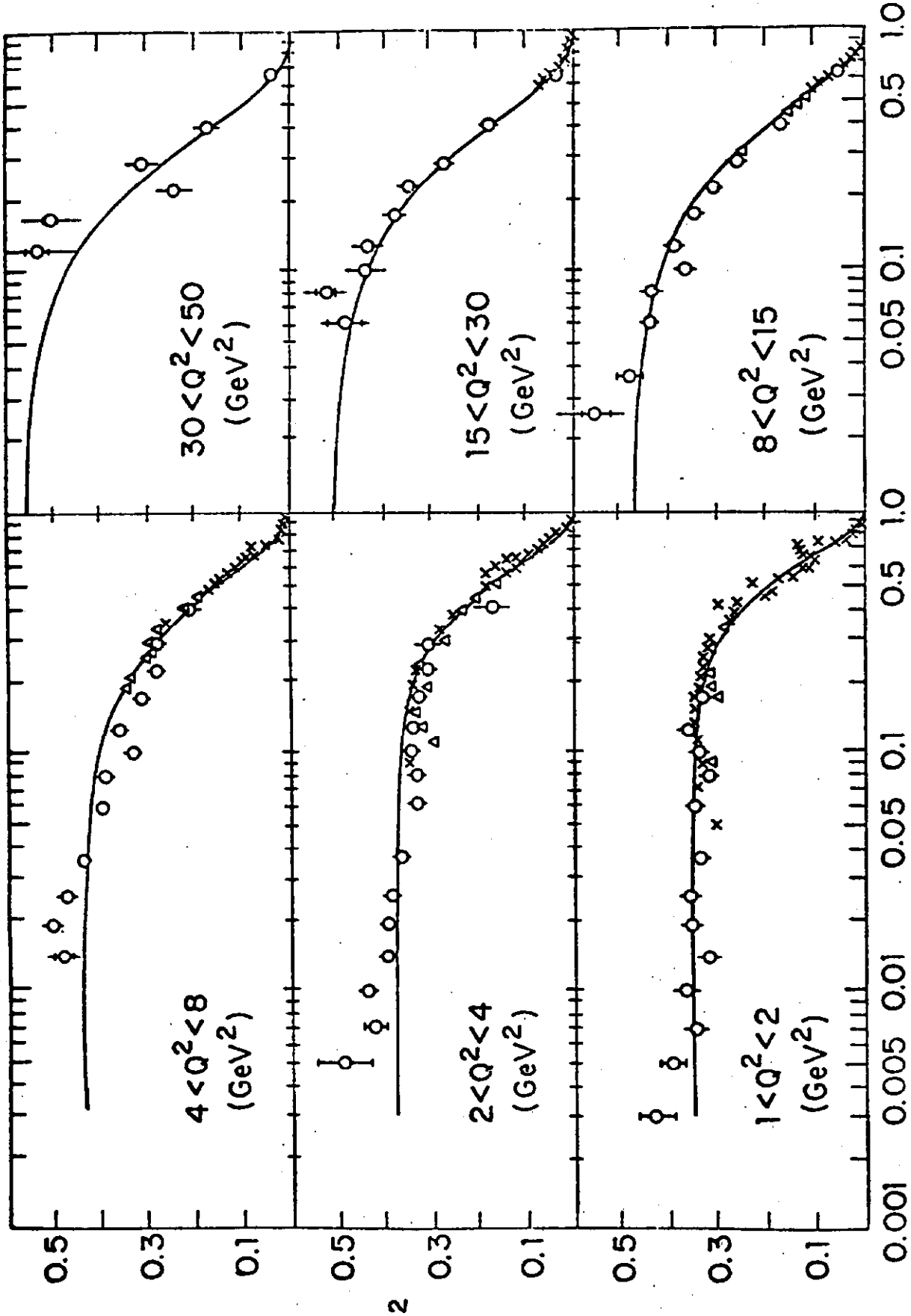

Fig. 23. F_2 for hydrogen as a function of x, showing the data of Fig. 19. The lines are the results of the global fit to the scaling region of Eq. (14).

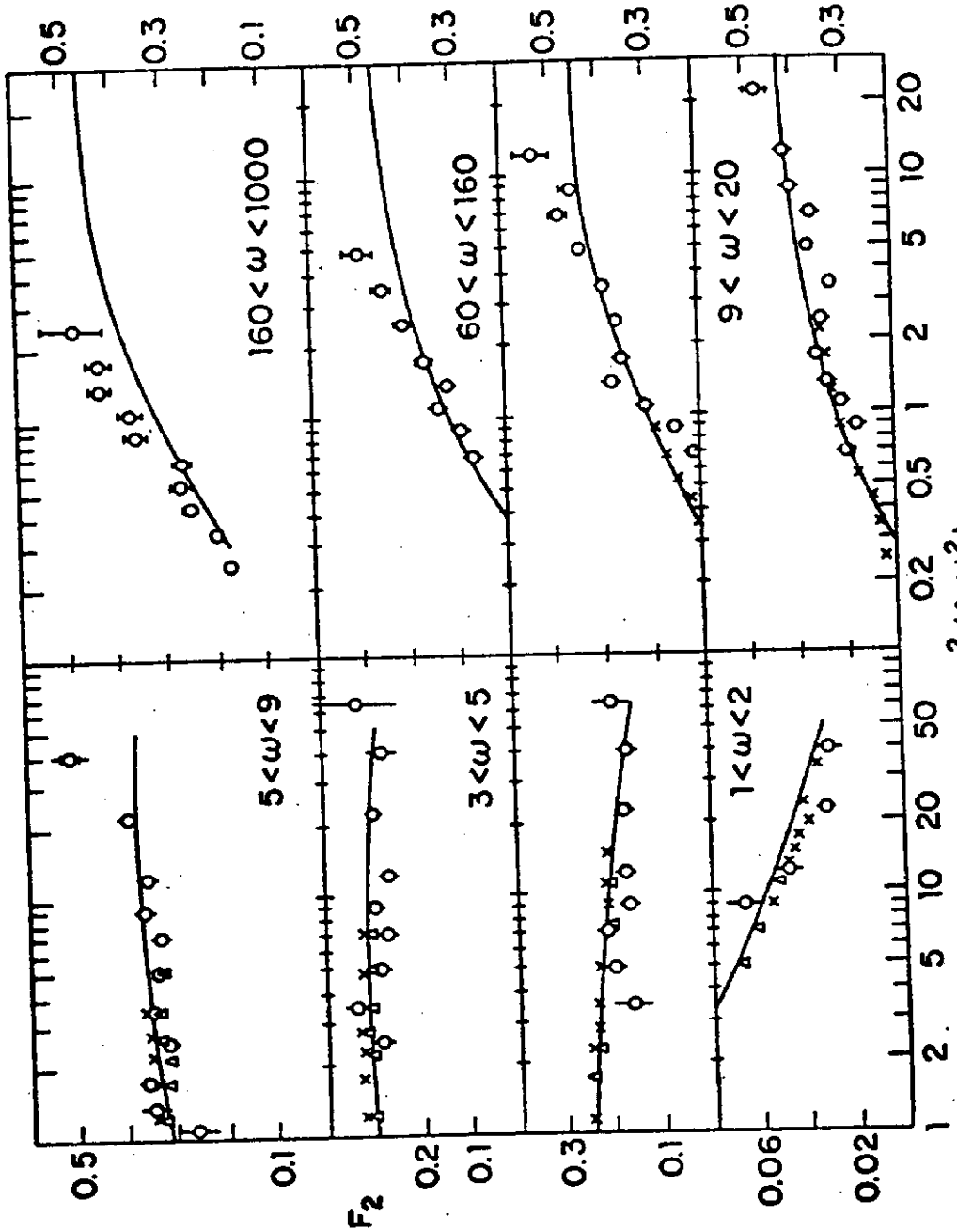

Fig. 24. F_2 for hydrogen as a function of Q^2, showing the data of Fig. 18. The lines are the results of fits to the approach to scaling and scaling regions of Eq. (15).

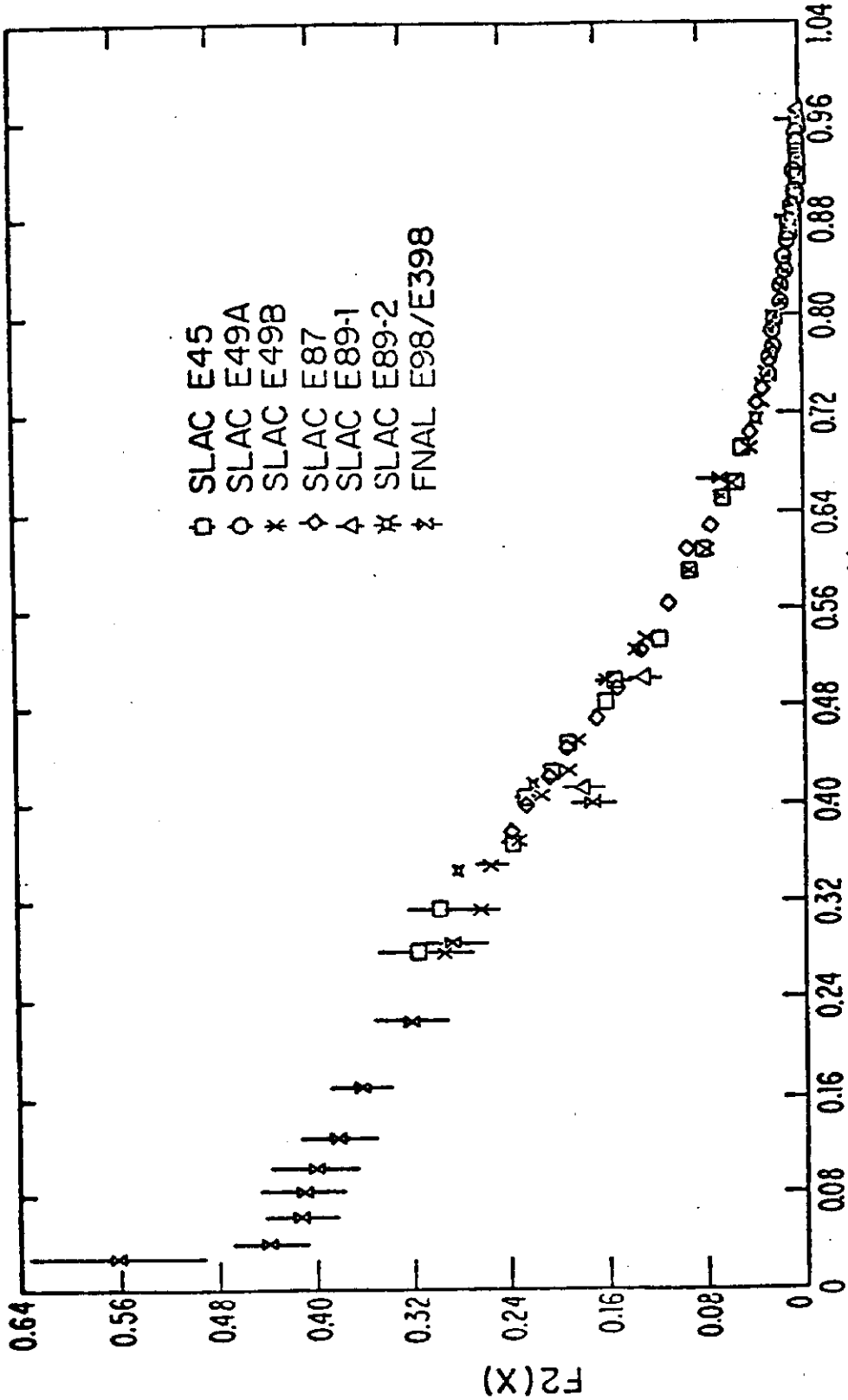

Fig. 25. Sample plot of data with $8 \leq Q^2 \leq 10$ GeV^2 used to obtain the moments of F_2 at $Q^2 = 9$ GeV^2. The μp data is from Fermilab E98/398. The ep data is from SLAC experiments as indicated. The value of R was taken to be 0.52 for μp, 0.21 for ep.

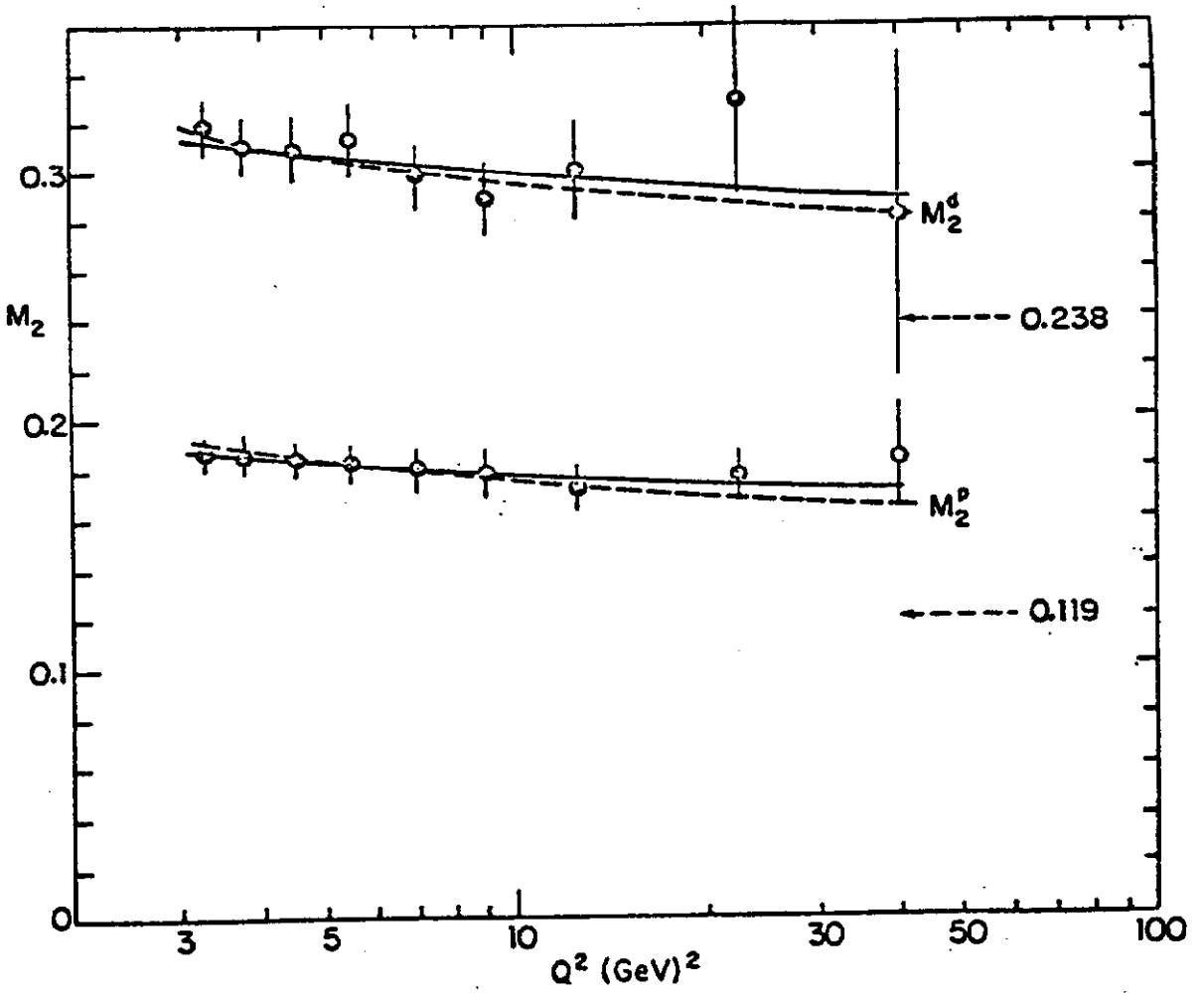

Fig. 26. Energy-momentum sum rule. The experimental Nachtmann moments $M_2(Q^2)$ for hydrogen and deuterium. Leading order QCD fits are shown. Solid curve is for $\Lambda = 0.18$ GeV, dashed curve for $\Lambda = 0.64$ GeV. The values 0.238 and 0.119 indicated by the arrows are the asymptotic $Q^2 \to \infty$ limits expected for the 4 flavor, 3 color quark-gluon model in QCD.

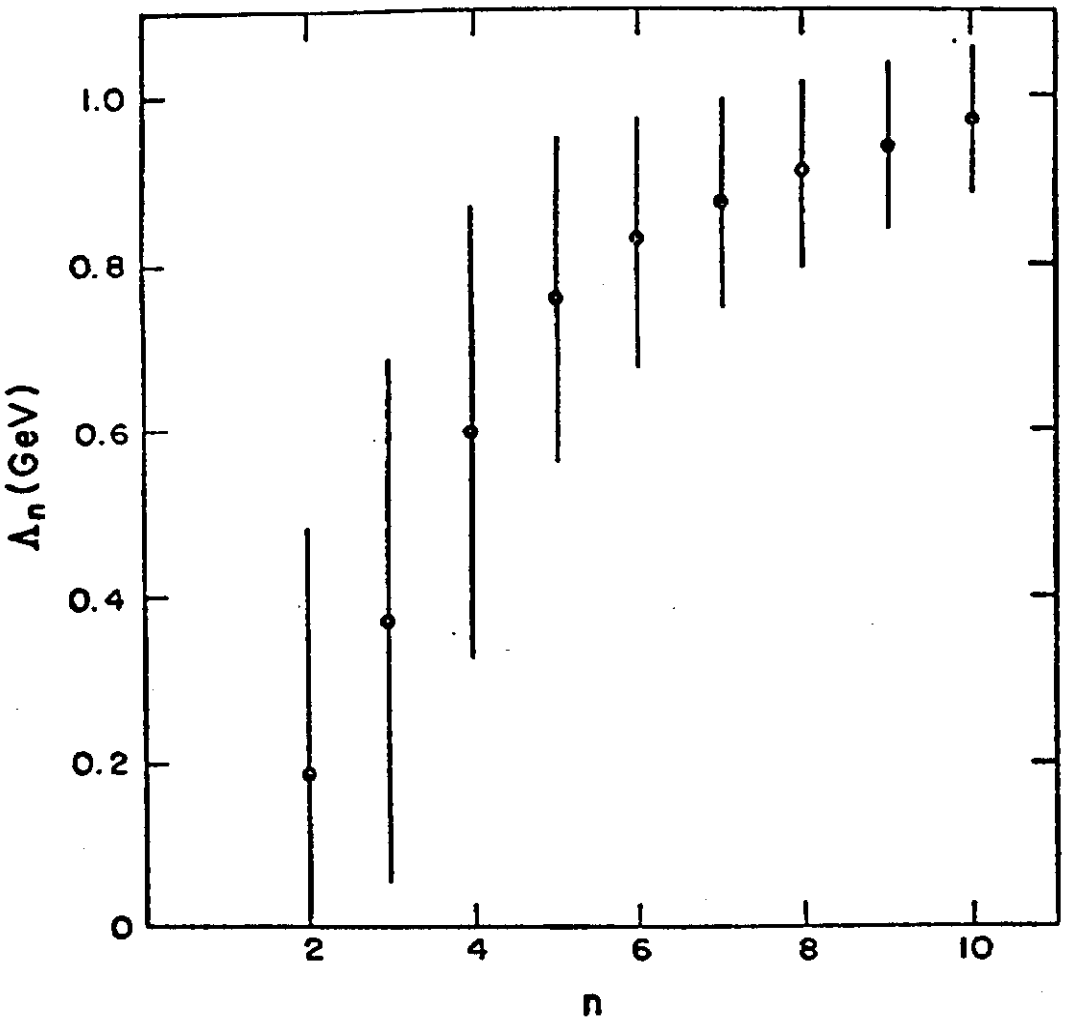

Fig. 27. Variation of Λ_n with n in leading order QCD analysis.

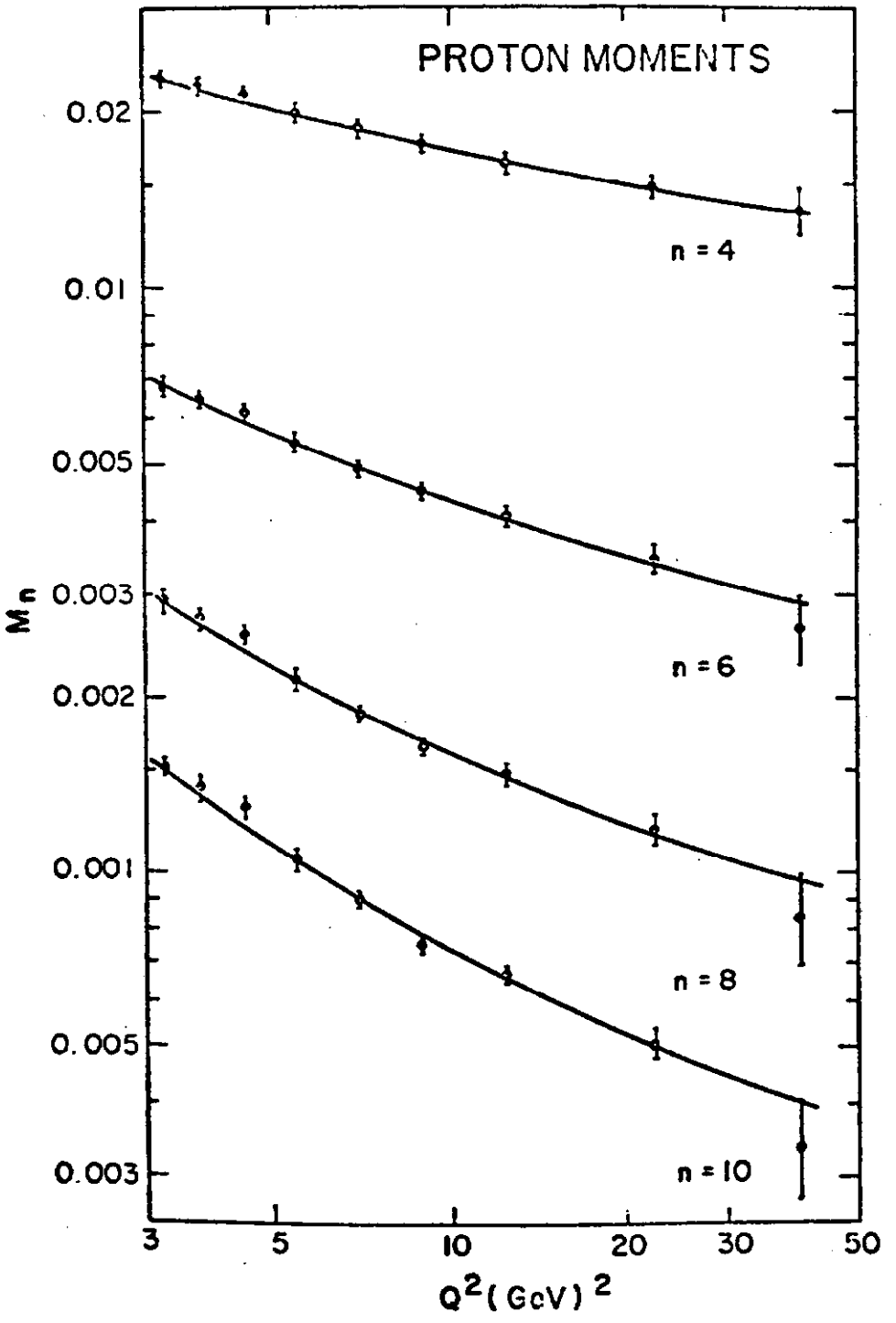

Fig. 28. The experimental Nachtmann moments for n = 4 to n = 10 for hydrogen and the fit in leading order QCD. Each n is analyzed separately.

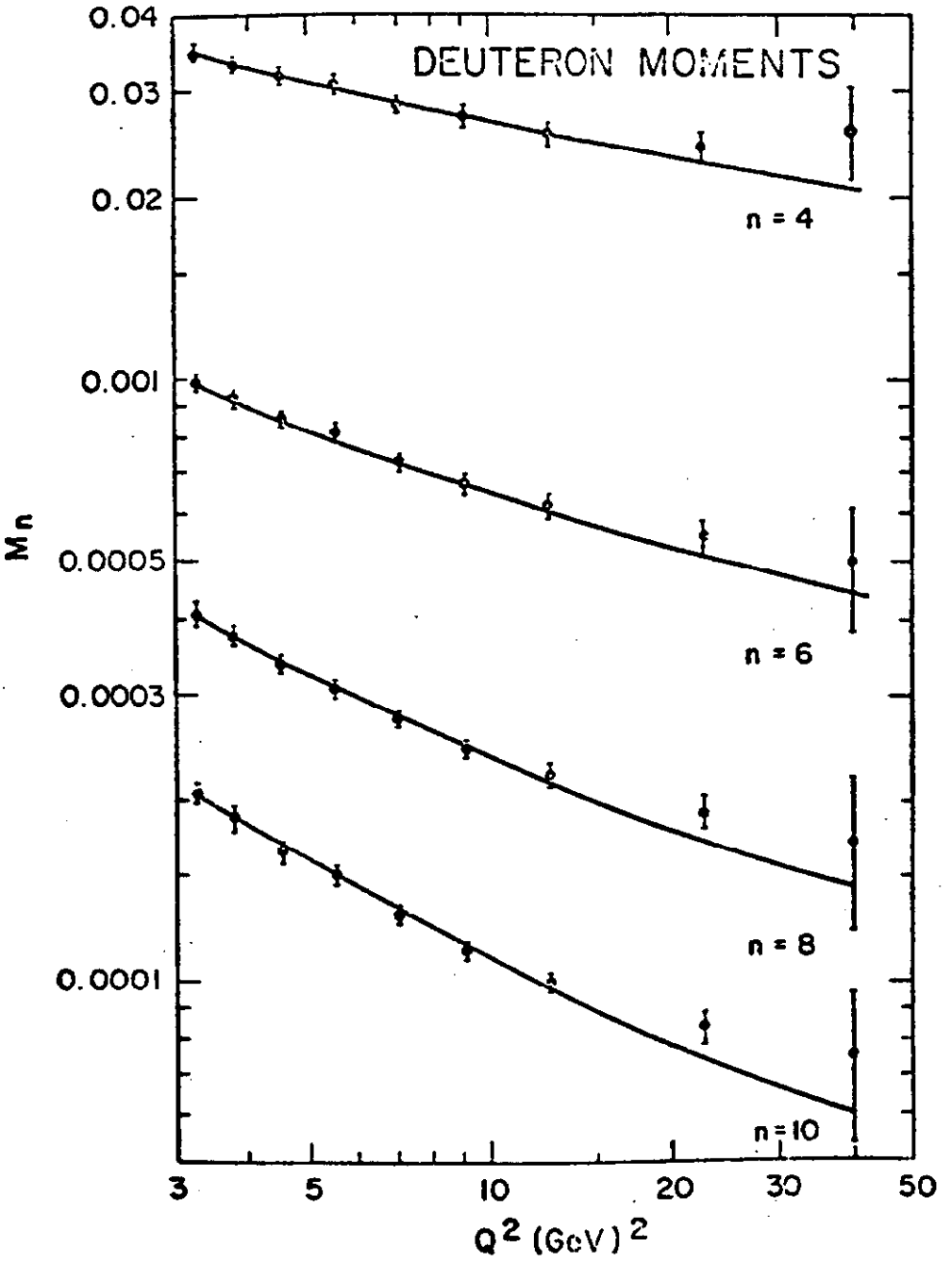

Fig. 29. The experimental Nachtmann moments for n = 4 to n = 10 for deuterium and the fit in leading order QCD. Each n is analyzed separately.

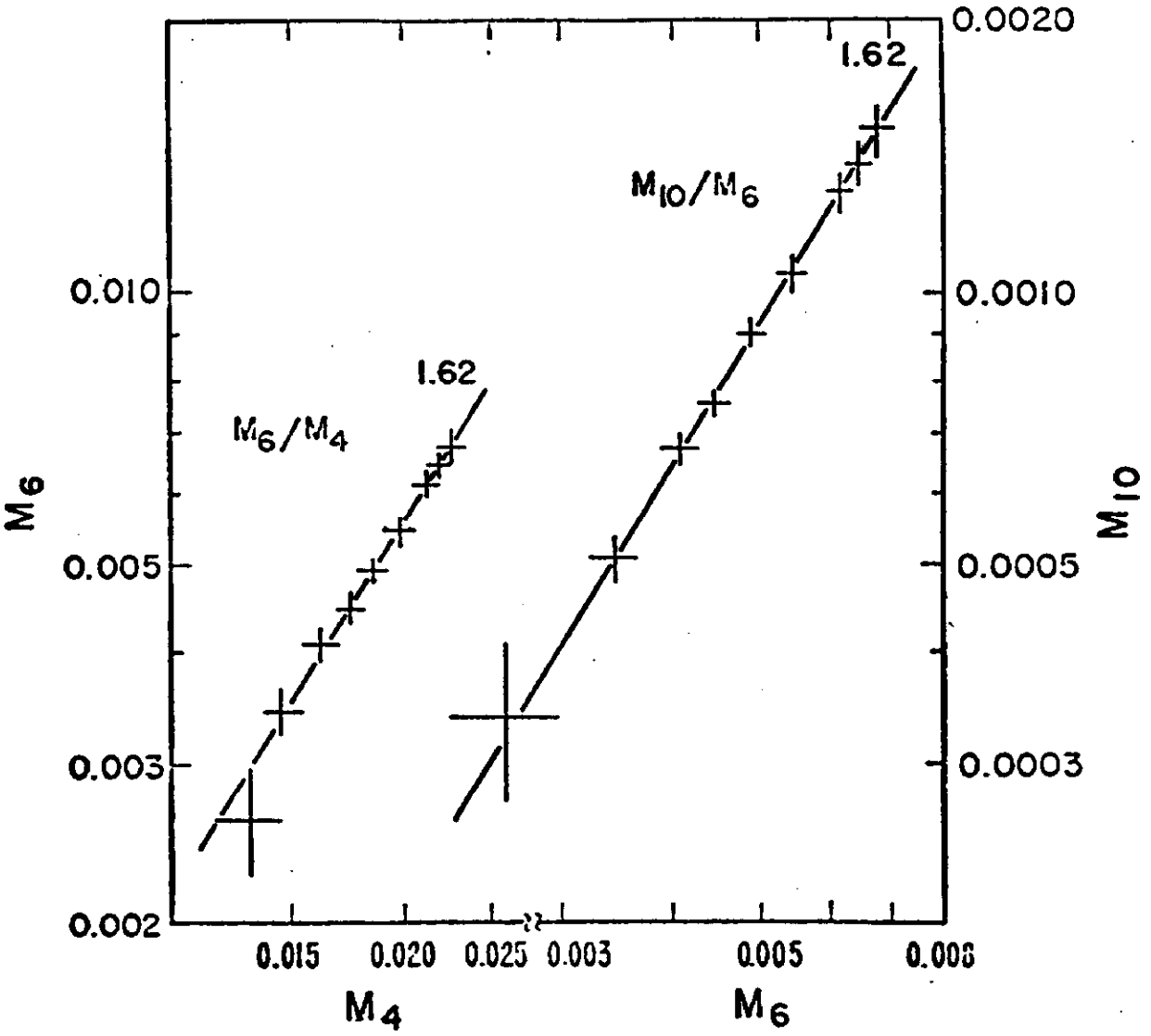

Fig. 30. Plot of log $M_6(Q^2)$ versus log $M_4(Q^2)$ and log $M_{10}(Q^2)$ versus log $M_6(Q^2)$.

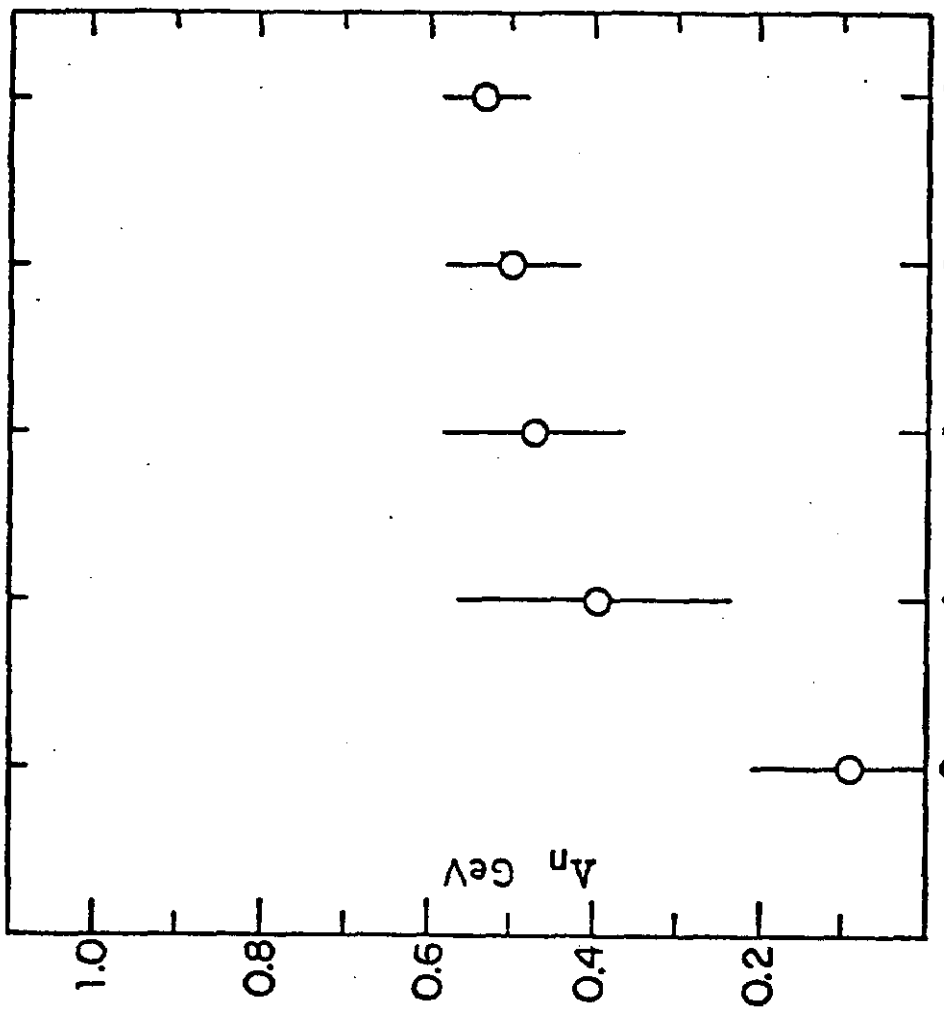

Fig. 31. Variation of Λ_n with n in 2nd order QCD analysis after correction for the Fermi motion in deuterium.

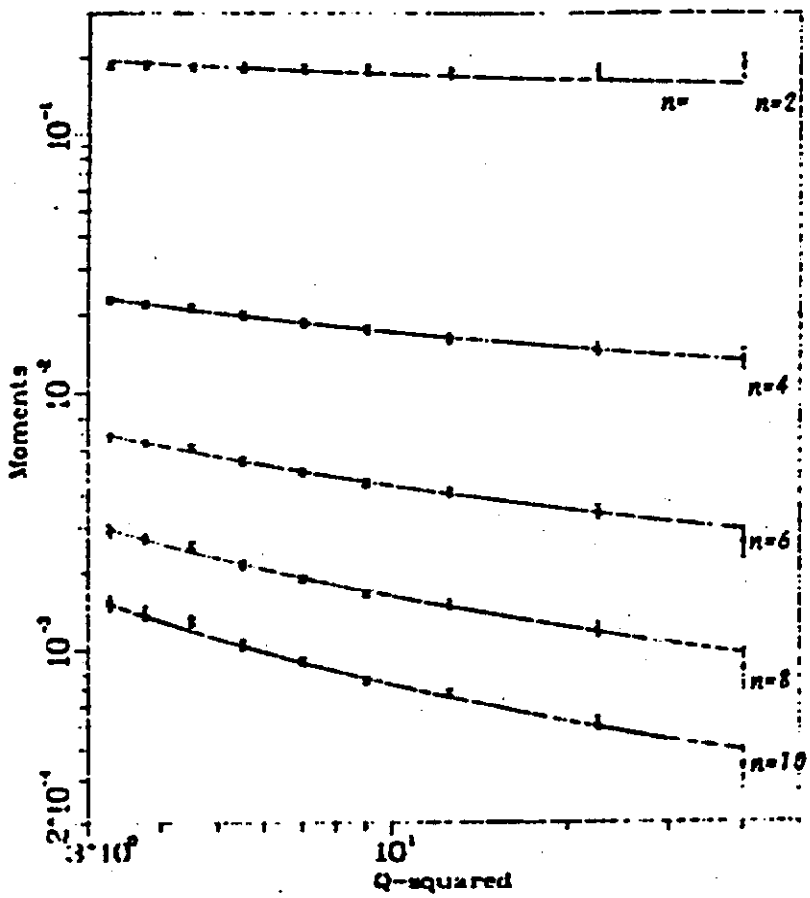

Fig. 32a. Global fit to the experimental Nachtmann moments in 2nd order QCD using $\Lambda = 469$ MeV. The deuterium moments have been corrected for Fermi motion.
a) Hydrogen

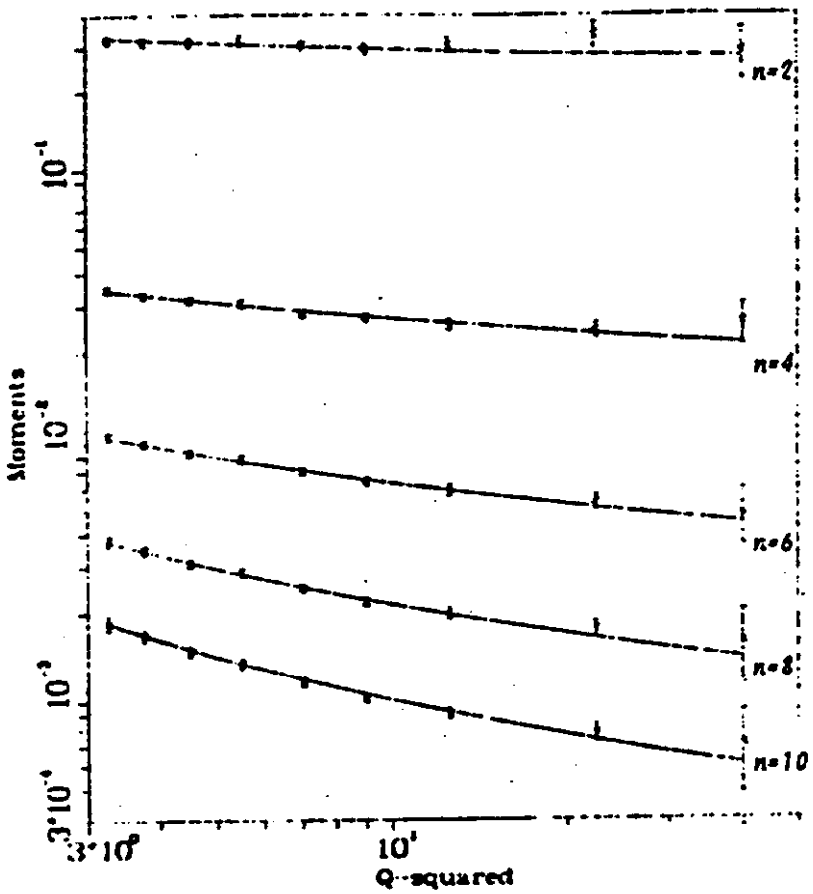

Fig. 32b. Global fit to the experimental Nachtmann moments in 2nd order QCD using $\Lambda = 469$ MeV. The deuterium moments have been corrected for Fermi motion.

b) Deuterium